

Multiscale computational modeling of size effects in carbon nanotube-polymer composites

Malagu, Marcello

DOI

[10.4233/uuid:22fbab3c-5da6-4a15-9275-ae01cd22f54f](https://doi.org/10.4233/uuid:22fbab3c-5da6-4a15-9275-ae01cd22f54f)

Publication date

2017

Document Version

Final published version

Citation (APA)

Malagu, M. (2017). *Multiscale computational modeling of size effects in carbon nanotube-polymer composites*. [Dissertation (TU Delft), Delft University of Technology]. <https://doi.org/10.4233/uuid:22fbab3c-5da6-4a15-9275-ae01cd22f54f>

Important note

To cite this publication, please use the final published version (if applicable). Please check the document version above.

Copyright

Other than for strictly personal use, it is not permitted to download, forward or distribute the text or part of it, without the consent of the author(s) and/or copyright holder(s), unless the work is under an open content license such as Creative Commons.

Takedown policy

Please contact us and provide details if you believe this document breaches copyrights. We will remove access to the work immediately and investigate your claim.

**MULTISCALE COMPUTATIONAL MODELING OF
SIZE EFFECTS IN
CARBON NANOTUBE-POLYMER COMPOSITES**

Marcello Malagù

MULTISCALE COMPUTATIONAL MODELING OF SIZE EFFECTS IN CARBON NANOTUBE-POLYMER COMPOSITES

Proefschrift

ter verkrijging van de graad van doctor
aan de Technische Universiteit Delft,
op gezag van de Rector Magnificus prof. ir. K.C.A.M. Luyben,
voorzitter van het College voor Promoties,
in het openbaar te verdedigen op dag 23 januari 2017 om 12:30 uur

door

Marcello MALAGÙ

ingegnere civile laureato all'Università degli Studi di Ferrara, Ferrara, Italië,
geboren te Ferrara, Italië.

This dissertation has been approved by

promoters: Prof. A.M. Tralli and Prof. dr. ir. L. J. Sluys

copromoters: Dr. E. Benvenuti and Dr. A. Simone

Composition of the doctoral committee:

Rector Magnificus,	chairman
Prof. A.M. Tralli,	Università degli Studi di Ferrara, promotor
Prof. dr. ir. L.J. Sluys,	Technische Universiteit Delft, promotor
Dr. E. Benvenuti,	Università degli Studi di Ferrara, copromotor
Dr. ir. A. Simone,	Technische Universiteit Delft, copromotor

Independent members:

Prof. ing. dr. hab. N. Challamel,	Université de Bretagne Sud
Prof. dr. ir. E. Schlangen,	Technische Universiteit Delft
Dr. K. Tserpes,	University of Patras
Dr. H. J. Böhm,	Technische Universität Wien
Prof. dr. ir. L. Nicola,	Technische Universiteit Delft, reserve member

The doctoral research has been carried out in the context of an agreement on joint doctoral supervision between Università degli Studi di Ferrara, Italy, and Delft University of Technology, the Netherlands. The work has been jointly supervised by Dr. Elena Benvenuti from University of Ferrara and Dr. Angelo Simone from Delft University of Technology.



This research has been supported by the Italian Ministry of Education, Universities and Research (Fondo Giovani 2011) and the European Research Council under the European Union's Seventh Framework Programme (FP7/2007-2013)/ERC Grant agreement n° 617972.

Keywords: carbon nanotubes, carbon nanotube-polymer composites, size effects, finite element method, atomistic simulations

Copyright © 2017 by M. Malagù

ISBN 9789402804928

Printed by Ipskamp Printing, Enschede, the Netherlands

An electronic version of this thesis is available at <http://repository.tudelft.nl/>.

*To my parents,
Mauro and Donatella*

Contents

Summary	ix
Sommario	xi
Samenvatting	xiii
1 Introduction	1
1.1 Aims of the thesis	1
1.2 Background	1
1.2.1 Carbon nanotubes	1
1.2.2 Carbon nanotube-polymer composites	3
1.3 Objectives and outline of the thesis	4
Bibliography	5
2 One-dimensional nonlocal and gradient elasticity: Assessment of high order approximation schemes	9
2.1 Introduction	9
2.2 Approximation schemes	11
2.2.1 B-spline basis functions	11
2.2.2 C^∞ generalized finite elements	13
2.3 Integro-differential elasticity	14
2.3.1 Homogeneous tensile rod under constant axial stress	16
2.3.2 Homogeneous tensile rod under body force with high gradient	18
2.4 Strain gradient formulation	28
2.4.1 Homogeneous tensile rod under constant axial stress	30
2.4.2 Inhomogeneous tensile rod under constant axial stress	30
2.5 Discussion	33
2.6 Conclusions	36
Bibliography	38
3 One-dimensional nonlocal elasticity for tensile single-walled CNTs: A molecular structural mechanics characterization	41
3.1 Introduction	41
3.2 MSM simulations of single-walled CNTs	43
3.2.1 Atomic model of single-walled carbon nanotubes	43
3.2.2 Model geometry	44
3.2.3 Young's modulus	46
3.2.4 Strain field in single-walled CNTs under tensile load	47
3.3 Nonlocal integro-differential elastic model for 1D problems	49
3.3.1 Numerical solution	53
3.4 Estimation of the nonlocal parameters	54

3.5	Conclusions	57
	Bibliography	60
4	A molecular-dynamics study of size and chirality effects on glass-transition temperature and ordering in carbon nanotube-polymer composites	65
4.1	Introduction	65
4.2	Model and simulation details	67
4.3	Results and discussion	69
4.3.1	Glass-transition temperature	69
4.3.2	Density profiles	71
4.3.3	Ordering of monomers	73
4.4	Conclusions	79
	Bibliography	81
5	Diameter dependent elastic properties of carbon nanotube-polymer composites: Emergence of size effects from atomistic to continuum scale	87
5.1	Introduction	87
5.2	Atomistic modeling of CNT-polymer composites	90
5.2.1	Method	90
5.2.2	Single-walled CNT and interphase volume fractions	92
5.2.3	Uniaxial tensile test simulations	95
5.2.4	Interface versus interphase	97
5.2.5	Size effect	99
5.3	Interphase as an equivalent continuum 3-D fiber	99
5.3.1	Numerical solution	100
5.3.2	Size effects	103
5.4	Micromechanical models for CNT-polymer composites	103
5.4.1	The embedded reinforcement method	104
5.5	Elastic properties of the nanocomposite	111
5.5.1	Analytical micromechanical models	113
5.5.2	Unidirectional reinforcement	115
5.5.3	Random reinforcement	115
5.5.4	Size effects	117
5.6	Summary and concluding remarks	117
5.A	Periodic boundary conditions for three-dimensional RVE	119
5.B	Control data for the NURBS continuum equivalent model	122
	Bibliography	122
6	Conclusions and future perspective	131
	Acknowledgements	135
	Curriculum Vitæ	137
	List of Publications	139

Summary

The development of carbon nanotube(CNT)-polymer composites advocates for a better understanding of their physical and mechanical properties that depend on the diameter of the embedded CNTs. Given that the experimental assessment of size effects is extremely difficult, the use of numerical models can be enormously helpful. However, since size effects might be observed both at the nano- and the macroscale, an adequate multiscale procedure is required.

In this thesis, numerical techniques are explored to develop a multiscale approach for the analysis of size effects in the elastic response of CNT-polymer composites. Atomistic simulations, such a molecular mechanics and molecular dynamics, are used for the characterization of the composites and their components at the nanoscale. The obtained results are then used to investigate size effects in the macroscopic properties of CNT-polymer composites using continuum models and efficient finite element techniques.

Molecular mechanics simulations on tensile carbon nanotubes show that their axial stiffness and axial strain field depend on the CNT diameter. Moreover, it is found that the axial strain field can be accurately reproduced using nonlocal continuum models if optimal nonlocal parameters, that vary with the nanotube diameter, and a suitable nonlocal kernel are used. Although the numerical solution of nonlocal problems is typically challenging, higher order B-spline finite elements overcome the issues encountered when standard approximation techniques are employed. Further, molecular dynamics simulations on CNT-polymer composites show that the CNT diameter alters the atomic structure and the mechanical properties of the ordered layer of polymer chains forming around the nanotube —the interphase. Such a layer has a significant impact on the mechanical properties of the composite. Although the role of the nanotubes during elastic deformation of the composite is negligible due to the weak non-bonded interface interactions, the interphase—thanks to its highly ordered atomic structure—is shown to enhance its mechanical properties. Here, molecular mechanics simulations at the nanoscale and the numerical solution of an equivalent continuum model at the macroscale indicate that the composite stiffness increases when the diameter of the carbon nanotubes is decreased.

When possible, the reliability of the results in this thesis has been assessed by means of analytical models and experimental or numerical results in the literature. Therefore, this study proposes a computational framework to improve our understanding of the mechanical response of CNT-polymer composites and the size effects on their elastic properties.

Sommario

Lo sviluppo di compositi polimerici rinforzati con nanotubi di carbonio (NTC) richiede una maggiore comprensione degli effetti delle dimensioni degli NTC sulle proprietà fisiche e meccaniche del composito. In questo contesto, l'impiego di modelli numerici è di fondamentale importanza a causa dei limiti che si incontrano nella caratterizzazione di questi materiali con prove sperimentali. Tuttavia, è necessario servirsi di un approccio multiscala in quanto gli effetti delle dimensioni degli NTC sono osservabili sia alla nano- che alla macroscale.

In questa tesi, diverse tecniche numeriche sono utilizzate per l'analisi multiscala degli effetti delle dimensioni degli NTC sulla risposta elastica dei compositi polimerici. Simulazioni atomistiche, come meccanica molecolare (MM) e dinamica molecolare (DM), sono impiegate per la caratterizzazione alla nanoscala dei compositi e dei loro singoli componenti. Con i risultati ottenuti ed avvalendosi di modelli continui ed efficienti tecniche agli elementi finiti, si sono analizzate le proprietà macroscopiche dei compositi.

Le simulazioni di MM su nanotubi in tensione mostrano che la rigidità assiale ed il campo di deformazione sono dipendenti dal diametro dell'NTC. Allo stesso tempo, si evidenzia che modelli continui nonlocali possono riprodurre in maniera accurata il campo di deformazione assiale nei nanotubi, se sono associati a idonei parametri nonlocali e un adeguato kernel nonlocale. Sebbene la soluzione numerica di problemi nonlocali è solitamente onerosa, elementi finiti B-spline di ordine elevato permettono di superare i problemi riscontrabili con tecniche di approssimazione classiche. Successivamente, le simulazioni di DM su matrici polimeriche rinforzate con NTC mostrano che il diametro dei nanotubi altera la struttura e le proprietà meccaniche dello strato di catene polimeriche circostanti (nota come interfase) con effetto rilevante sulle proprietà del composito. Nonostante il ruolo del nanotubo sulla deformazione elastica del composito sia irrilevante a causa delle deboli interazioni all'interfaccia, è provato che l'interfase (grazie alla sua ordinata struttura atomica) porta ad un miglioramento delle proprietà meccaniche del composito. In quest'ambito, simulazioni di MM alla nanoscala e l'analisi numerica di un modello equivalente per il composito alla macroscale indicano che la rigidità del composito aumenta al diminuire del diametro degli NTC.

Quando possibile, l'attendibilità dei risultati riportati in questa tesi è stata valutata con l'ausilio di modelli analitici e risultati sperimentali e numerici presenti in letteratura. Pertanto, la metodologia computazionale adottata in questo studio accresce la conoscenza della risposta meccanica dei compositi polimerici rinforzati con nanotubi in carbonio e dell'effetto delle dimensioni degli NTC sulle loro proprietà elastiche.

Samenvatting

De ontwikkeling van koolstof nanobuizen (KNB)-polymeren composieten pleit voor een beter begrip van de fysische en mechanische eigenschappen van de composieten die afhankelijk zijn van de diameter van de KNB. Gegeven dat de proefondervindelijke analyse van afmetingseffecten extreem moeilijk is, kan het gebruik van numerieke rekenmodellen zeer behulpzaam zijn. Afmetingseffecten zijn echter waarneembaar op zowel nano- als macroschaal, waardoor een geschikt multischaal algoritme noodzakelijk is.

In dit proefschrift worden numerieke technieken onderzocht voor het ontwikkelen van een multischale aanpak voor de analyse van afmetingseffecten in het elastisch gedrag van KNB-polymeren composieten. Atomistische simulaties, zoals moleculaire mechanica en moleculaire dynamica, worden gebruikt voor het karakteriseren van de composieten en hun onderdelen op nanoschaal. De verkregen resultaten worden gebruikt om de afmetingseffecten van de macroscopische eigenschappen van KNB-polymeren composieten te onderzoeken met behulp van continuümmodellen en efficiënte eindige-elemententechnieken. Moleculaire mechanica simulaties op rekbare koolstof nanobuizen tonen dat hun axiale stijfheid en axiale spanningsveld afhankelijk zijn van de diameter van de KNB. Ook is er getoond dat het axiale spanningsveld nauwkeurig reproduceerbaar is met behulp van niet-lokale continuümmodellen als de optimale diameter-afhankelijke niet-lokale parameters en een geschikte niet-lokale kern worden gebruikt.

Hoewel de numerieke oplossing van niet-lokale vraagstukken een uitdaging is, lossen hogere-orde B-spline eindige elementen de problemen op die normaliter optreden bij het gebruik van standaard benaderingsmethodes. Daarnaast tonen moleculaire dynamica simulaties van KNB-polymeren composieten dat de invloed van de diameter van de KNB op de atomaire structuur en op de mechanische eigenschappen van de geordende polymerenkettingenlaag om de nanotube —de interfase. Een dergelijke laag heeft een significante invloed op de mechanische eigenschappen van het composiet. Hoewel de rol van KNB tijdens de elastische deformatie van het composiet verwaarloosbaar is door de slappe ongebonden interface interacties, verbetert de interfase de mechanische eigenschappen door een zeer geordende atomaire structuur. Moleculaire mechanische simulaties op nanoschaal en de numerieke oplossing van een equivalent continuümmodel op macroschaal tonen aan dat de stijfheid van het composiet toeneemt wanneer de diameter van de KNB wordt verkleind.

Waar mogelijk is de betrouwbaarheid van de resultaten in dit proefschrift geëvalueerd door middel van analytische modellen en proefondervindelijke of numerieke resultaten uit de literatuur. Daarom stelt deze studie een rekenkundig raamwerk voor om het verband tussen de mechanische response en de afmetingseffecten op de elastische eigenschappen van KNB-polymeren composieten beter te begrijpen.

Chapter 1

Introduction

1.1 Aims of the thesis

The exceptional mechanical and physical properties of carbon nanotubes (CNTs) make them the ideal candidates for the design of high-performance polymer-based composite materials. However, due to their small dimensions, the analysis of CNT-polymer composites is difficult and, despite several works have been published during the last two decades, some fundamental issues need more investigation.

For instance, the effects of the nanotube diameter and chirality on the mechanical response of CNT-polymer composites, crucial for their design, are still unclear. Since the dimension of the CNTs circular cross section is comparable to the characteristic size of the polymer chains, a variation of the nanotube diameter can lead to different CNT-polymer interactions and alter the matrix atomic structure. Indeed, experimental observations indicated the presence of nanotube-induced size effects in the mechanical properties of CNT-polymer composites. However, the small size of the carbon nanotubes make the experimental characterization of size effects extremely challenging. Nevertheless, this problem can be addressed by means of computer simulations.

The main goal of this thesis is to develop an efficient computational procedure for modeling size effects in CNTs and CNT-polymer composites. Atomistic simulations have been used to provide fundamental insights about the nanoscale features of CNTs and CNT-polymer composites and continuum models have been employed to efficiently assess size effects at the macroscale.

In this first chapter, a brief presentation of the problems discussed in this work is given. An overview of the main features and issues regarding the mechanical characterization of CNTs and CNT-polymer composites is provided in Sections 1.2.1 and 1.2.2, respectively. Finally, the outline of the thesis is presented in Section 1.3.

1.2 Background

1.2.1 Carbon nanotubes

Carbon nanotubes are hollow cylindrical structures formed by hexagonal rings of carbon atoms (see Figure 1.1(a) and (b)) with a diameter of a few nanometers and length in the micrometers range. When a CNT consists of a single tube the term single-walled carbon

nanotube is used, while a CNT formed by multiple concentric nanotubes is called multi-walled carbon nanotube. Then, CNTs are also identified according to their chirality, the orientation of the hexagonal carbon rings with respect to the nanotube axis.

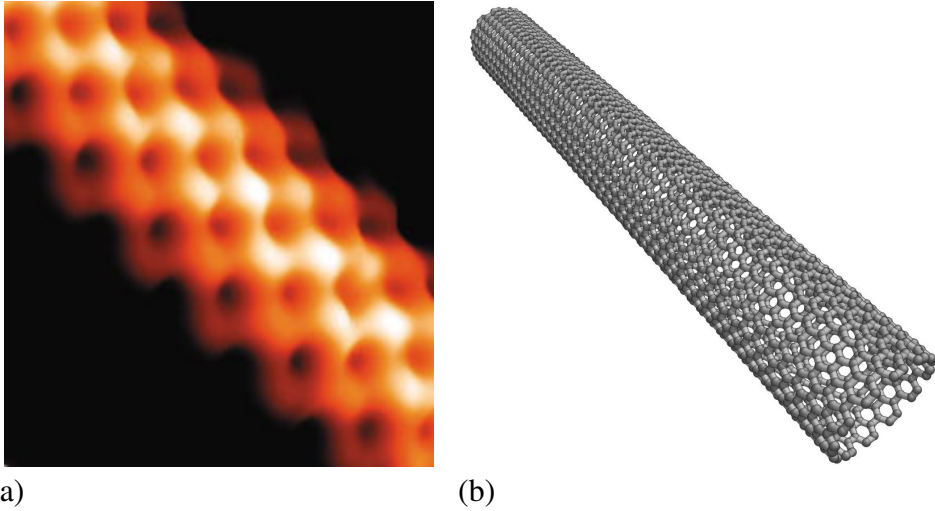


Figure 1.1: (a) Scanning tunneling microscopy image [20], and (b) schematic representation of single-walled carbon nanotubes.

Due to the small dimension of the nanotubes in the radial direction, their mechanical properties can be dependent on diameter, length and chirality. However, experimental assessment of effects of structural changes on the mechanical response of CNTs is extremely difficult. Due to the errors and uncertainties introduced by the measurements at the nanoscale, experiments show large scatter in the results—typical experimental values for the Young’s modulus vary between 0.6 and 2.4 TPa [10, 14, 17, 19, 21]. On the contrary, atomistic simulations such as *ab initio* calculations, molecular dynamics, molecular mechanics and molecular structural mechanics, that can accurately model nanoscale systems, provided values of the Young’s modulus in a smaller range, spanning between 0.8 and 1.1 TPa [3, 9, 13, 18, 22]. Here, size effects have been observed, indicating that the Young’s modulus decreases when the nanotube diameter is smaller than $1.5 \div 2$ nm. Moreover, effects induced by the chirality of the nanotubes have also been noticed.

Due to their high computational cost, atomistic simulations are limited to systems of small dimensions. Therefore, the analysis of size effects in long CNTs, and consequently in CNT-polymer composites, by means of atomistic simulations is prohibitive and several attempts have been made to study CNTs with continuum models. In particular, nonlocal continuum models, that can account for the long range interactions at the nanoscale and reproduce size effects, are the natural choice for the modeling of carbon nanotubes. Two nonlocal models commonly used for CNTs are the models proposed by Eringen [7] and Aifantis [1]. Both approaches add a term to the classical constitutive equations such that the stress at a given point depends on the strain field at surrounding points. In the Eringen model

the additional term involves a weighted integral of the strain field while in the Aifantis model it is defined by the Laplacian of the strain tensor. Moreover, the additional term includes one or more so-called nonlocal parameters to account for the characteristic length of the material atomic structure.

The finite element method is typically employed when studying nonlocal problems since their analytical solution is usually difficult. However, the use of the finite elements for the analysis of nonlocal problems present some issues that need be addressed. When the Eringen model is used, efficient finite element approximations are required to overcome the computational burden as the stiffness matrix loses sparsity, while in the case of the Aifantis model highly continuous finite elements are needed to satisfy requirements on the discretization.

Another important issue regarding the use of nonlocal formulations for the modeling of CNTs focuses on the choice of the nonlocal parameters. Although several works on the use of nonlocal models for the analysis of carbon nanotubes have been proposed, only few papers tried to address this issue.

1.2.2 Carbon nanotube-polymer composites

Carbon nanotubes, besides their exceptional physical and mechanical properties, bring two significant advantages over traditional reinforcements: high interface area, size effects in the interfacial shear strength and enhancement of the mechanical properties of the polymer matrix.

CNTs have very high aspect ratio. In typical short-fiber composites, the fiber aspect ratio ranges between 100 and 500 [6] while that of carbon nanotubes is higher than 10^3 . This implies a higher interface area at small volume fraction of reinforcement (see Figure 1.2).

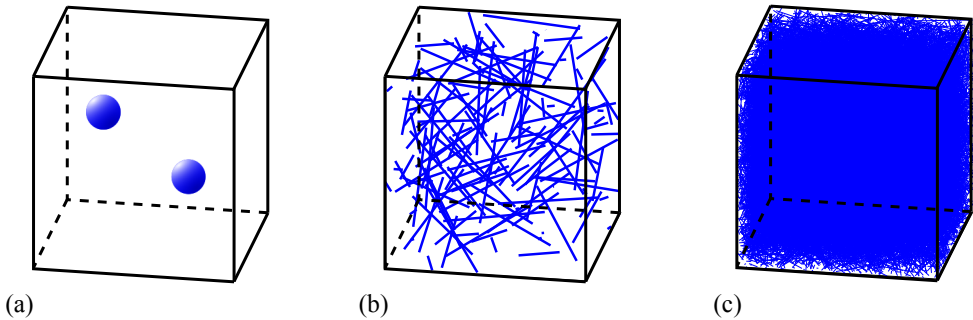


Figure 1.2: Schematic representation of the distribution of micro- and nanoparticles ((a) Al_2O_3 particles, (b) carbon fibers and (c) CNTs) in a homogeneous matrix having the same 0.1 % volume fraction of reinforcement. This figure has been adapted from [15].

Moreover, since the diameter of the nanotubes is comparable to the characteristic size of its atomic structure and that of the surrounding polymer chains, size effects might be observed also in CNT-polymer composites. Barber and coworkers [2] were the first to observe size effects in the interfacial shear strength of CNT-butane composites. Pull-out tests of individual carbon nanotubes from the polymer matrix showed that the interfacial shear strength

increases by decreasing the nanotube diameter (see Figure 1.3). Analogous results were later obtained with similar experiments [4] and molecular dynamics simulations [5, 12]. However, the effect of the diameter on the composite mechanical properties at the macroscale has not been investigated.

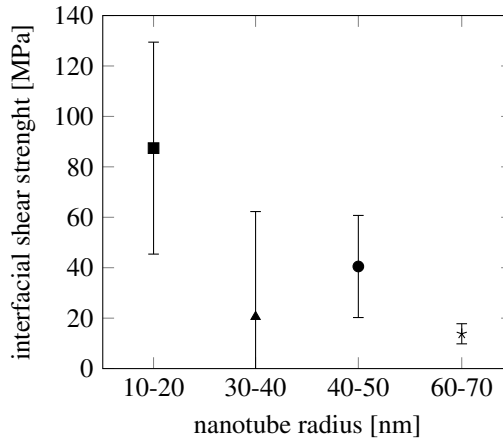


Figure 1.3: Diameter induced size effects on the interfacial shear strength from pull-out test in CNT-butane [2].

Furthermore, experimental observations on a wide class of polymers confirmed the formation of an ordered structure of polymer chains [11], surrounding the nanotubes as shown in Figure 1.4. Nucleation of such a layer, usually referred to as the interphase, is greatly beneficial as it offers additional reinforcement to composite. However, since the interphase thickness is comparable to the diameter of the nanotubes, its experimental characterization is difficult. Hence, atomistic simulations are typically employed since they allow for the detailed investigation of the structure of the polymer chains. However, only few studies investigated the size effects on the structure of the interphase [8] while size effects on its mechanical properties are still not clear.

1.3 Objectives and outline of the thesis

The basic idea behind this thesis is to develop a computational procedure for the analysis of size effects in CNT-polymer composites (only single-walled CNTs are considered in this work). Since different length scales are involved, from few nanometers to several micrometers, a multiscale approach performing atomistic and continuum simulations is employed.

The approach here adopted consists in the analysis of CNT-polymer composites through a detailed investigation of its single phases (i.e., carbon nanotubes, interface, interphase and polymer matrix). Atomistic simulations are used for the characterization of the material at the nanoscale and equivalent continuum models are further developed to examine size effects at the macroscale. Nonlocal models have been initially considered for the assessment of size

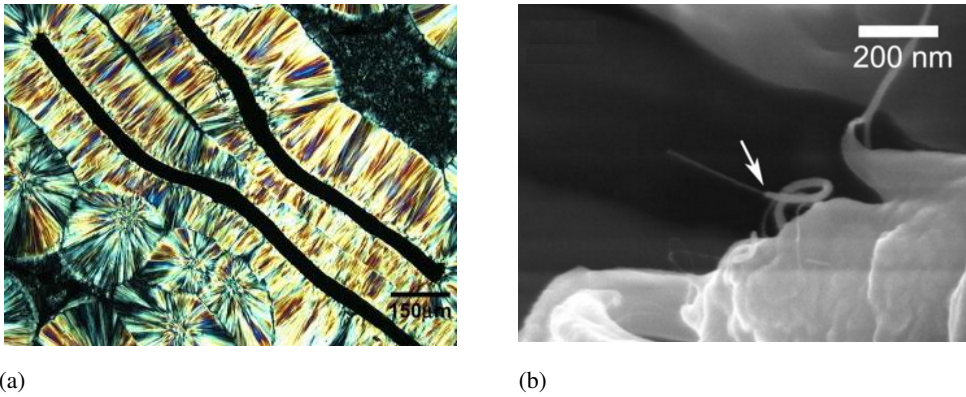


Figure 1.4: Optical micrographs of crystallized (a) polypropylene [23] and (b) poly(vinyl alcohol) [16] (the arrow indicates the crystallized coating around carbon nanotubes).

effects in the elastic response of carbon nanotubes and, consequently, the modeling of CNTs as one-dimensional fibers when embedded in a polymer matrix.

Therefore, this thesis starts with the assessment of several finite element approximations on the numerical solution of one-dimensional nonlocal problems (Chapter 2). The estimation of the optimal nonlocal parameters required for modeling size effects in the elastic response of tensile CNTs is further presented in Chapter 3. The reference solution of the strain field in the carbon nanotubes is obtained by means of molecular structural mechanics atomistic simulations (throughout the thesis, the CNTs atomic structure is assumed defect-free). Then, a detailed analysis of size effects induced by the nanotube in the structural properties of the interphase in CNT-polymer composites is carried out in Chapter 4 by using molecular dynamics simulations. A coarse-grained amorphous monodisperse polyethylene-like model is employed for the polymer matrix to provide general insights into a wide range of polymer-based materials. Only non-bonded interactions between CNTs and polymer chains have been considered. Finally, size effects in the micromechanical response of the CNT-polymer composites are discussed in Chapter 5 where particular attention is devoted to the assessment of the role played by the CNT, the interface, the interphase and the polymer matrix. Due to weak interactions at the interface, the effect of the nanotubes in the mechanical response of the composite is negligible. Hence, only the interphase is considered as reinforcement phase when CNT-polymer composites are modeled at the microscale.

Bibliography

- [1] E. C. Aifantis. On the role of gradients in the localization of deformation and fracture. *International Journal of Engineering Science*, 30(10):1279–1299, 1992.
- [2] A. H. Barber, S. R. Cohen, S. Kenig, and H. D. Wagner. Interfacial fracture energy measurements for multi-walled carbon nanotubes pulled from a polymer matrix. *Composites Science and Technology*, 64(15):2283–2289, 2004.

- [3] T. Chang and H. Gao. Size-dependent elastic properties of a single-walled carbon nanotube via a molecular mechanics model. *Journal of the Mechanics and Physics of Solids*, 51(6):1059–1074, 2003.
- [4] X. Chen, L. Zhang, M. Zheng, C. Park, X. Wang, and C. Ke. Quantitative nanomechanical characterization of the van der Waals interfaces between carbon nanotubes and epoxy. *Carbon*, 82:214–228, 2015.
- [5] B. Coto, I. Antia, J. Barriga, M. Blanco, and J.-S. Sarasua. Influence of the geometrical properties of the carbon nanotubes on the interfacial behavior of epoxy/CNT composites: A molecular modelling approach. *Computational Materials Science*, 79:99–104, 2013.
- [6] S. K. De and J. R. White. *Short fibre-polymer composites*. Elsevier, 1996.
- [7] A. C. Eringen. On differential equations of nonlocal elasticity and solutions of screw dislocation and surface waves. *Journal of applied physics*, 54(9):4703–4710, 1983.
- [8] S. G. Falkovich, S. V. Larin, A. V. Lyulin, V. E. Yudin, J. M. Kenny, and S. V. Lyulin. Influence of the carbon nanofiller surface curvature on the initiation of crystallization in thermoplastic polymers. *RSC Advances*, 4(89):48606–48612, 2014.
- [9] C. Goze, L. Vaccarini, L. Henrard, P. Bernier, E. Hernandez, and A. Rubio. Elastic and mechanical properties of carbon nanotubes. *Synthetic Metals*, 103(1):2500–2501, 1999.
- [10] A. Krishnan, E. Dujardin, T. W. Ebbesen, P. N. Yianilos, and M. M. J. Treacy. Young’s modulus of single-walled nanotubes. *Physical Review B*, 58(20):14013, 1998.
- [11] E. C. Laird and C. Y. Li. Structure and morphology control in crystalline polymer-carbon nanotube nanocomposites. *Macromolecules*, 46(8):2877–2891, 2013.
- [12] Y. Li, Y. Liu, X. Peng, C. Yan, S. Liu, and N. Hu. Pull-out simulations on interfacial properties of carbon nanotube-reinforced polymer nanocomposites. *Computational Materials Science*, 50(6):1854–1860, 2011.
- [13] G. Van Lier, C. Van Alsenoy, V. Van Doren, and P. Geerlings. Ab initio study of the elastic properties of single-walled carbon nanotubes and graphene. *Chemical Physics Letters*, 326(1):181–185, 2000.
- [14] O. Lourie and H. D. Wagner. Evaluation of Young’s modulus of carbon nanotubes by micro-Raman spectroscopy. *Journal of Materials Research*, 13(09):2418–2422, 1998.
- [15] P.-C. Ma, N. A. Siddiqui, G. Marom, and J.-K. Kim. Dispersion and functionalization of carbon nanotubes for polymer-based nanocomposites: A review. *Composites Part A: Applied Science and Manufacturing*, 41(10):1345–1367, 2010.
- [16] J. Meng, Y. Zhang, K. Song, and M. L. Minus. Forming crystalline polymer-nano interphase structures for high-modulus and high-tensile/strength composite fibers. *Macromolecular Materials and Engineering*, 299(2):144–153, 2014.

- [17] J.-P. Salvetat, J.-M. Bonard, N. H. Thomson, A. J. Kulik, L. Forro, W. Benoit, and L. Zuppiroli. Mechanical properties of carbon nanotubes. *Applied Physics A*, 69(3): 255–260, 1999.
- [18] H. Tashakori, B. Khoshnevisan, and F. Kanjuri. Ab initio systematic study of chirality effects on phonon spectra, mechanical and thermal properties of narrow single walled carbon nanotubes. *Computational Materials Science*, 83:16–21, 2014.
- [19] M. M. J. Treacy, T. W. Ebbesen, and J. M. Gibson. Exceptionally high Young’s modulus observed for individual carbon nanotubes. *Nature*, 381:678–680, 1996.
- [20] J. W. G. Wilder, L. C. Venema, A. G. Rinzler, R.E. Smalley, and C. Dekker. Electronic structure of atomically resolved carbon nanotubes. *Nature*, 391(6662):59–62, 1998.
- [21] E. W. Wong, P. E. Sheehan, and C. M. Lieber. Nanobeam mechanics: Elasticity, strength, and toughness of nanorods and nanotubes. *Science*, 277(5334):1971–1975, 1997.
- [22] N. Yao and V. Lordi. Young’s modulus of single-walled carbon nanotubes. *Journal of Applied Physics*, 84(4):1939–1943, 1998.
- [23] S. Zhang, M. L. Minus, L. Zhu, C.-P. Wong, and S. Kumar. Polymer transcrystallinity induced by carbon nanotubes. *Polymer*, 49(5):1356–1364, 2008.

Chapter 2

One-dimensional nonlocal and gradient elasticity: Assessment of high order approximation schemes*

We investigate the application and performance of high-order approximation techniques to one-dimensional nonlocal elastic rods. Governing equations and corresponding discrete forms are derived for the integro-differential formulation proposed by Eringen and the laplacian-based strain gradient formulation developed by Aifantis and coworkers. Accuracy and convergence rate of the numerical solutions obtained with Lagrange, Hermite, B-spline finite elements and C^∞ generalized finite elements are assessed against the corresponding analytical solutions.

2.1 Introduction

Effective modeling of nonlocal problems is a challenging issue in computational mechanics. In this context, high order approximation schemes are often required. Here, we compare standard and high order approximation schemes with a high degree of continuity in the analysis of one-dimensional nonlocal elasticity boundary value problems. In particular, we consider problems whose solution fields present local area of high gradients at the boundary or within the domain.

It is well known that classical continuum mechanics fails to predict deformation phenomena at the nanoscale due to the absence of an internal material length scale in the constitutive law. Therefore, nonclassical formulations have been proposed to model size-dependent problems where the effect of material microstructure and long-range interatomic forces becomes predominant. In this context, one-dimensional nonlocal formulations have been used to describe the mechanical response of nanostructures such as nanotrusses and carbon nanotubes [5, 40].

The finite element method is the *de facto* choice for the analysis of systems which show a size-dependent mechanical response [7, 8, 24, 31], for the analytical solution of these problems is usually difficult even in the most simple cases. Nevertheless, several issues arise from the implementation of either computationally intensive algorithms or highly continuous approximation schemes when derivatives of the strain field are included in the constitutive

*Reproduced from: M. Malagù, E. Benvenuti, C.A. Duarte and A. Simone, One-dimensional nonlocal and gradient elasticity: Assessment of high order approximation schemes, *Computer Methods in Applied Mechanics and Engineering*, 275:138–158, 2014.

equations. In fact, the numerical solution of nonlocal elastic problems poses great challenges since most of the approaches in the literature show limitations. Equally important, the finite element analysis of size-dependent systems depends on the constitutive equations employed to represent the nonlocal medium. Among others, Eringen [22] suggested an integro-differential formulation where the stress at a given point is made a weighted function of the strain at surrounding points. The corresponding finite element formulation leads to significant computational effort since the stiffness matrix reflects the nonlocality of the material [32] and loses sparsity. Aifantis and coworkers extended the classical elastic constitutive equations with the Laplacian of the strain tensor [2], consequently increasing the continuity requirements for the approximation schemes [4] which need to be C^1 -continuous or higher.

In this work, non-conventional approximation techniques are tested on the aforementioned nonlocal elastic models and compared against traditional approaches. We consider B-spline finite elements and C^∞ generalized finite elements (C^∞ GFEM) along with classical Lagrange and Hermite discretization techniques. The first method is widely used to approximate smooth and free-form geometries [30] and employs high-order piecewise polynomial basis functions. This technique can achieve a high degree of continuity through the so-called k -refinement technique [27] as described in Section 2.2.1. Furthermore, B-spline finite elements have been the subject of several publications, especially because of the interest in the Isogeometric Analysis [11, 27, 28, 39]. The second approximation scheme uses a C^∞ partition of unity (PoU) and polynomial enrichments to build arbitrarily smooth basis functions [19] as detailed in Section 2.2.2.

The main objective of this work is to present benchmark studies aimed at shedding some light on the assessment of the accuracy of the aforementioned approximation schemes. Starting from the governing equilibrium equations of the tensile rod, their discrete form is derived for the integro-differential formulation and the strain gradient model described in Section 2.3 and 2.4, respectively. We discuss the main features which distinguish these approaches and characterize implementation and continuity requirements on the discretization. We then consider some practical applications. In particular, the case study of a tensile rod with constant stress is used to compare the numerical results obtained with the two constitutive models employing the approximation schemes previously described. The performance of the approximation schemes is further assessed by means of two other examples: a homogeneous tensile rod under the action of a body force with high gradient employing the integro-differential formulation, and a strain gradient bimaterial rod with constant stress. The MATLAB[®] scripts used in the benchmark studies are freely available for download at the corresponding author's web site.

To the best of our knowledge, the work in this chapter represents the first attempt to compare the accuracy of classical and novel approximation techniques in the solution of nonlocal problems. In particular, we discuss the numerical results obtained from the integro-differential and the strain-gradient approaches in great detail. Furthermore, for the first time within the framework of the finite element method, high order approximations are used in the discrete equations derived from the integro-differential approach. It is not possible to say a-priori which method would be the most suitable to solve these equations. Hence, this work may provide significant insight into the applicability of high order methods in size-dependent problems which are for instance very useful for developers of nonlocal FE

models for nanowires and nanotubes [1, 6, 9, 29, 35].

2.2 Approximation schemes

In the finite element method analysis of one-dimensional elasticity problems, the displacement field $u(x)$ and the corresponding strain field $\varepsilon(x)$ are approximated at the element level through

$$u^e(x) \simeq \mathbf{N}^e(x) \mathbf{u}^e \quad \text{and} \quad \varepsilon^e(x) \simeq \frac{d\mathbf{N}^e}{dx} \mathbf{u}^e = \mathbf{B}^e(x) \mathbf{u}^e, \quad (2.1)$$

where \mathbf{N}^e is a vector containing element basis functions and \mathbf{u}^e is the vector of the unknown displacement degrees of freedom (dofs).

The weak statement of the governing differential equation of a generic boundary value problem poses continuity requirements on the solution fields. These continuity requirements can be met by means of appropriate approximation schemes. The most popular approximation schemes in computational solid mechanics of one-dimensional objects are Lagrange and cubic Hermite basis functions. Lagrange basis functions are interpolating polynomials and are C^0 functions whereas cubic Hermite basis functions are cubic polynomials which are C^1 -continuous at interelement boundaries—in general, Hermite basis functions of order p are $C^{(p-1)/2}$ -continuous at interelement boundaries. Hermite basis functions belongs to the family of spline basis functions [26]. In the next sections, high-order B-spline basis functions and C^∞ GFEM are investigated and compared to traditional Lagrange and Hermite finite elements in nonlocal problems.

2.2.1 B-spline basis functions

B-splines are piecewise polynomial functions which can be used to construct high-order and highly continuous basis functions on compact supports. Each support is spanned by a sequence of coordinates, known as *knots*, which is related to the basis functions number n and order p . The knot set $\Xi = \{\xi_1, \xi_2, \dots, \xi_{n+p+1}\}$, termed *knot vector*, subdivides the domain into $n+p$ *knot spans* which are equivalent to the element domains of a standard finite element mesh. Once the basis functions of order p and the knot vector Ξ are known, B-spline basis functions $N_{i,p}$ are defined by means of the Cox-de Boor recursion formula [12, 15]. Starting from the constant basis function

$$N_{i,0}(\xi) = \begin{cases} 1 & \text{if } \xi_i \leq \xi \leq \xi_{i+1} \\ 0 & \text{otherwise,} \end{cases} \quad (2.2)$$

B-splines basis functions of any order p are computed through

$$N_{i,p}(\xi) = \frac{\xi - \xi_i}{\xi_{p+i} - \xi_i} N_{i,p-1}(\xi) + \frac{\xi_{i+p+1} - \xi}{\xi_{i+p+1} - \xi_{i+1}} N_{i+1,p-1}(\xi). \quad (2.3)$$

These basis functions form a partition of unity and they are non-negative over the whole domain.

Figure 2.1 compares Lagrange, Hermite and B-spline basis functions on a one-dimensional domain discretized into three equally-spaced subdomains (finite elements and knot spans).

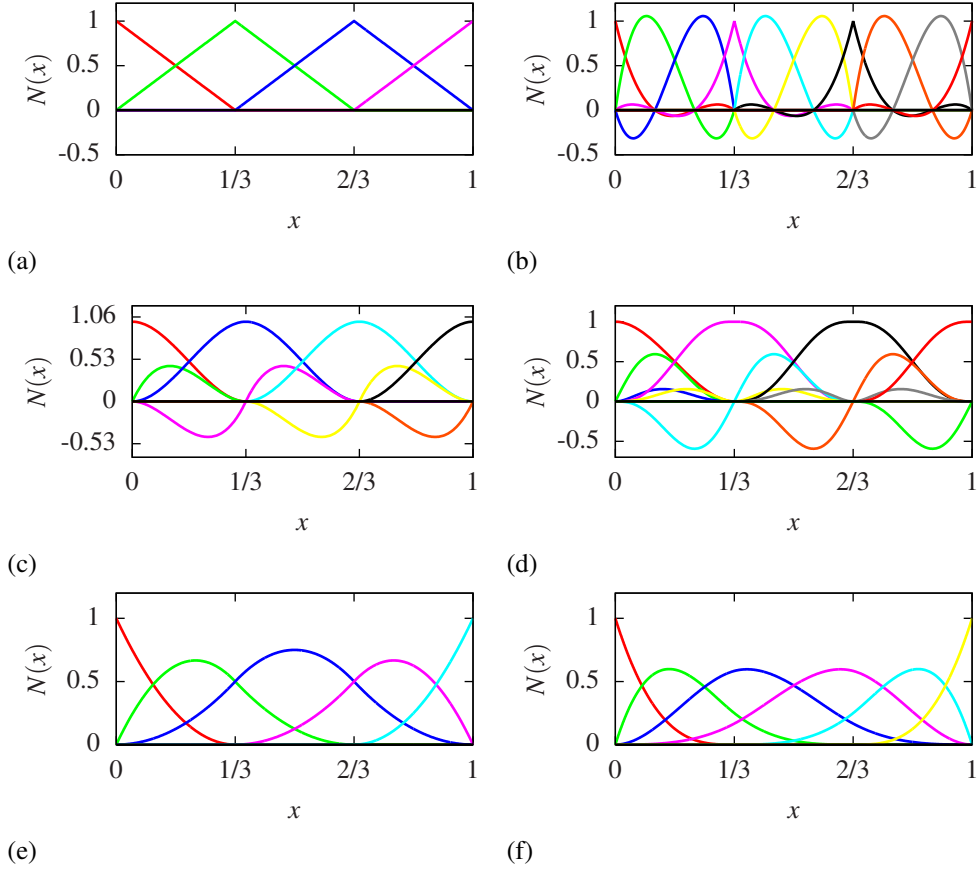


Figure 2.1: Approximation schemes: (a)-(b) linear and cubic Lagrange basis functions, (c)-(d) cubic and quintic Hermite basis functions, and (e)-(f) quadratic and cubic B-spline basis functions. The global domain is discretized into three equally-spaced subdomains.

Unlike Lagrange and Hermite basis functions, whose continuity decreases at the elements boundaries, B-spline basis functions are usually C^{p+1} -continuous over their support which is defined by $p + 1$ knot spans. However, if a knot has multiplicity m , the continuity of the basis functions will decrease to C^{p-m} at that knot. B-spline basis functions are interpolant at the boundaries and at those knots where the continuity is C^0 whereas they are approximant elsewhere.

The quality of the approximation can be improved by employing h -refinement and p -refinement which are similar to the corresponding techniques used in the traditional finite element method. A combination of these two techniques, the so-called k -refinement, is a distinguishing feature of B-spline basis functions. With this refinement scheme, the polynomial order is increased and new knots are inserted into the original knot vector. More details on theoretical and computational aspects of B-splines can be found in References [16, 26, 30].

2.2.2 C^∞ generalized finite elements

The C^∞ generalized finite element method (C^∞ GFEM) was proposed by Edwards [19, 20] in order to build finite elements with arbitrarily smooth basis functions. In the C^∞ GFEM, highly continuous basis functions, similar to those used in meshfree methods, have support on a standard finite element mesh. All finite elements sharing node x_α define a polygonal region called *cloud* which is indicated by ω_α . In a one-dimensional setting, cloud ω_α reduces to the domain between nodes $x_{\alpha-1}$ and $x_{\alpha+1}$. The construction of C^∞ basis functions requires several accessory functions and starts with the definition of the *cloud boundary functions*

$$\mathcal{E}_{\alpha,j}(x) = \begin{cases} e^{-\xi_j^{-\gamma}(x)} & \text{if } \xi_j(x) > 0 \\ 0 & \text{otherwise,} \end{cases} \quad (2.4)$$

which are defined on the support cloud ω_α as a function of the parametric coordinate

$$\xi_j(x) = \left(\frac{1-2^\gamma}{\log_e \beta} \right)^{\frac{1}{\gamma}} \frac{(x-x_j)}{h_{\alpha j}} \quad (2.5)$$

where j is equal to $\alpha \pm 1$ and $h_{\alpha j}$ is the distance between nodes x_α and x_j (here we assume $\gamma = 0.6$ and $\beta = 0.3$ as in [18]). These cloud boundary functions are used to define the *weighting functions*

$$\mathcal{W}_\alpha(x) = e^{c_\alpha} \prod_{j=1}^{M_\alpha} \mathcal{E}_{\alpha,j}(x) = \begin{cases} e^{\left(c_\alpha - \sum_{j=1}^{M_\alpha} \xi_j^{-\gamma} \right)} & \text{if } \xi_j > 0 \\ 0 & \text{otherwise,} \end{cases} \quad (2.6)$$

where the parameter M_α indicates the number of cloud boundary functions supported on cloud ω_α and the factor

$$c_\alpha = M_\alpha \left(\frac{1-2^\gamma}{\log_e \beta} \right)^{-1} \quad (2.7)$$

stems from the condition $\mathcal{W}_\alpha(x_\alpha) = 1$. C^∞ partition of unity functions $\varphi_\alpha(x)$ at node x_α are constructed through the Shepard's formula using the weighting functions $\mathcal{W}_\alpha(x)$ according to

$$\varphi_\alpha(x) = \frac{\mathcal{W}_\alpha(x)}{\sum_{\kappa(x)} \mathcal{W}_\kappa(x)} \quad \text{with } \kappa(x) \in \{\gamma \mid \mathcal{W}_\gamma(x) \neq 0\}. \quad (2.8)$$

As shown in [18], C^∞ basis functions satisfy the Kronecker delta property

$$\varphi_\alpha(x_\beta) = \delta_{\alpha\beta}. \quad (2.9)$$

Finally, C^∞ GFEM basis functions $\phi_{\alpha i}(x)$ of order i at node x_α are defined as the product of C^∞ partition of unity functions $\varphi_\alpha(x)$ and polynomial enrichments $L_{\alpha i}(x)$ as

$$\phi_{\alpha i}(x) = \varphi_\alpha(x) L_{\alpha i}(x) \quad (2.10)$$

with

$$L_{\alpha i}(x) = \frac{(x-x_\alpha)^i}{h_\alpha} \quad (2.11)$$

where h_α is the cloud radius [14]. For one-dimensional uniform meshes, like those used in this work, h_α is the finite elements size. The basis functions $\phi_{\alpha i}$, shown in Figure 2.2 together with the weighting functions $\mathcal{W}_\alpha(x)$ and the partition of unity functions $\varphi_\alpha(x)$, are employed to approximate the displacement field according to

$$u(x) \simeq \sum_{\alpha=1}^n \sum_{i=0}^{p_\alpha} u_{\alpha i} \phi_{\alpha i}(x) = \sum_{\alpha=1}^n \sum_{i=0}^{p_\alpha} u_{\alpha i} L_{\alpha i}(x) \varphi_\alpha(x) \quad (2.12)$$

in which p_α is the order of the polynomial enrichment function and, at the same time, indicates the number of degrees of freedom at node x_α . Imposition of Dirichlet boundary conditions is trivial as proved in [18]. Indeed, from (2.12),

$$u(\bar{x}_\alpha) = \sum_{\alpha=1}^n \sum_{i=0}^{p_\alpha} u_{\alpha i} L_{\alpha i}(\bar{x}_\alpha) \varphi_\alpha(\bar{x}_\alpha) \quad (2.13)$$

at a boundary node \bar{x}_α and, considering (2.9) and (2.11) and assuming a prescribed value \bar{u} at \bar{x}_α , it follows that

$$u(\bar{x}_\alpha) = \sum_{i=0}^{p_\alpha} u_{\alpha i} L_{\alpha i}(\bar{x}_\alpha) = u_{\alpha 0} \cdot 1 = \bar{u}. \quad (2.14)$$

The above relation implies that a Dirichlet boundary condition can be enforced as in traditional finite element methods on the degree of freedom corresponding to the polynomial enrichment of order zero.

2.3 Integro-differential elasticity

In an isotropic and homogeneous rod with constant Young's modulus E and cross sectional area A , integro-differential elasticity theory defines the stress σ at point x through a weighted integral of the strain ε [22]. In this study, we adopt the constitutive law

$$\sigma(x) = E \xi_1 \varepsilon(x) + E \xi_2 \int_{\Omega} \alpha(x, \bar{x}) \varepsilon(\bar{x}) d\bar{x} \quad (2.15)$$

proposed by Eringen [23]. The nonlocal kernel

$$\alpha(x, \bar{x}) = g_0 e^{-\frac{|x-\bar{x}|}{\ell}} \quad (2.16)$$

is a weighting function in which the normalization factor g_0 is equal to $1/(2\ell)$ and ℓ is the material characteristic length. Furthermore, constitutive parameters ξ_1 and ξ_2 obey the relations $\xi_1 \geq 1$ and $\xi_1 + \xi_2 = 1$ [10].

The governing equation is derived by setting the first variation of the total potential energy

$$\Pi(u) = W_i(u) - W_e(u) \quad (2.17)$$

equal to zero, where W_i and W_e express the virtual work of internal and external forces, respectively. According to [32], the total potential energy corresponding to the integro-differential constitutive equation (2.15) is expressed as

$$\Pi(u) = \frac{1}{2} \int_0^L \left[\xi_1 EA \varepsilon^2(x) + \frac{\xi_2}{2\ell} \int_0^L e^{-\frac{|x-\bar{x}|}{\ell}} EA \varepsilon(\bar{x}) d\bar{x} \varepsilon(x) \right] dx - \int_0^L q(x) u(x) dx, \quad (2.18)$$

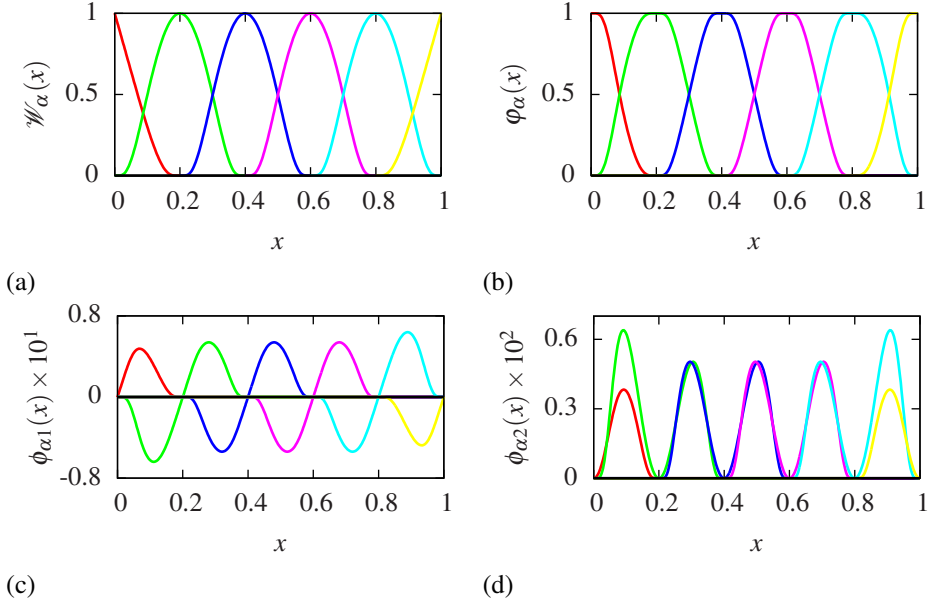


Figure 2.2: One-dimensional C^∞ GFEM: (a) weighting functions, (b) partition of unity shape functions, and shape functions enriched with (c) linear and (d) quadratic polynomials.

where $q(x)$ is the distributed axial load. Setting $\varepsilon(x) = u'(x)$, the first variation of the total potential energy

$$\begin{aligned} \delta\Pi(u) = & \int_0^L \left[\xi_1 EAu'(x)\delta u'(x) + \frac{\xi_2}{2\ell} \int_0^L e^{-\frac{|x-\tilde{x}|}{\ell}} EAu'(\tilde{x}) d\tilde{x} \delta u'(x) \right] dx \\ & - \int_0^L q(x)\delta u(x) dx = 0, \end{aligned} \quad (2.19)$$

which holds for any kinematically admissible $u(x) \in \mathcal{S}$ and $\delta u(x) \in \mathcal{V}$. The two functional spaces \mathcal{S} and \mathcal{V} are defined according to [37]

$$\mathcal{S} = \{u(x) \mid u(x) \in H^1, u = \bar{u} \text{ on } \Gamma_u\} \quad (2.20)$$

and

$$\mathcal{V} = \{\delta u(x) \mid \delta u(x) \in H^1, \delta u = 0 \text{ on } \Gamma_u\} \quad (2.21)$$

where the overbar refers to a prescribed value, and the boundary Γ is divided into a displacement (Γ_u) and a traction (Γ_t) part such that $\Gamma_t \cup \Gamma_u = \Gamma$ and $\Gamma_t \cap \Gamma_u = 0$. Application of the divergence theorem on (2.19) results into

$$\begin{aligned} \delta\Pi(u) = & - \int_0^L \left[EA \left(\xi_1 u''(x) + \frac{\xi_2}{2\ell} \int_0^L e^{-\frac{|x-\tilde{x}|}{\ell}} u''(\tilde{x}) d\tilde{x} \right) + q(x) \right] \delta u(x) dx \\ & + \left[EA \left(\xi_1 u'(x) + \frac{\xi_2}{2\ell} \int_0^L e^{-\frac{|x-\tilde{x}|}{\ell}} u'(\tilde{x}) d\tilde{x} \right) \delta u(x) \right] \Big|_{\Gamma} = 0 \end{aligned} \quad (2.22)$$

which, thanks to the fundamental lemma of the calculus of variations and the arbitrariness of δu , yields the Euler equation

$$EA \left(\xi_1 u''(x) + \frac{\xi_2}{2\ell} \int_0^L e^{-\frac{|x-\tilde{x}|}{\ell}} u''(\tilde{x}) d\tilde{x} \right) + q(x) = 0 \quad \forall x \in [0, L]. \quad (2.23)$$

Furthermore, since setting $\delta u = 0$ at the boundary is equivalent to specify u at the boundary itself, (2.22) results into the boundary conditions

$$EA \left(\xi_1 u'(x) + \frac{\xi_2}{2\ell} \int_0^L e^{-\frac{|x-\tilde{x}|}{\ell}} u'(\tilde{x}) d\tilde{x} \right) = \bar{N} \quad \text{on } \Gamma_t \quad \text{and} \quad (2.24a)$$

$$u(x) = \bar{u} \quad \text{on } \Gamma_u, \quad (2.24b)$$

where \bar{N} is a prescribed axial force. The discretized form of the governing equation, $\mathbf{K}\mathbf{u} = \mathbf{f}$, with the stiffness matrix

$$\mathbf{K} = \bigwedge_{e=1}^{n_{el}} \int_{x_1^e}^{x_2^e} \left(\xi_1 \mathbf{B}^{eT}(x) EA \mathbf{B}^e(x) + \frac{\xi_2}{2\ell} \int_0^L e^{-\frac{|x-\tilde{x}|}{\ell}} \mathbf{B}^{eT}(x) EA \mathbf{B}^e(\tilde{x}) d\tilde{x} \right) dx \quad (2.25)$$

and the external force vector

$$\mathbf{f} = \bigwedge_{e=1}^{n_{el}} \left[\mathbf{f}_\Omega^e + \mathbf{f}_\Gamma^e \right] = \bigwedge_{e=1}^{n_{el}} \left[\int_{x_1^e}^{x_2^e} \mathbf{N}^{eT}(x) q(x) dx + \left(\mathbf{N}^{eT}(x) N(x) \right) \Big|_\Gamma \right], \quad (2.26)$$

is derived following standard procedures. It bears emphasis that the computation of elemental stiffness matrices is more complex than in traditional finite elements methods as it requires the evaluation of contributions from the whole domain and the integration of products of high-order shape function derivatives with the exponential kernel—in the numerical studies performed in the following sections, particular care has been taken in performing an accurate integration of the stiffness matrix. The computational cost is also related to the number of degrees of freedom involved and the type of approximation as shown in Table 2.1.

	Lagrange finite elements	Hermite finite elements	B-splines finite elements	C^∞ GFEM
continuity	C^0	$C^{(p-1)/2}$	C^{p-1}	C^∞
dofs	$n_e p + 1$	$(n_e + 1)(p + 1)/2$	$n_e + p$	$(n_e + 1)(p_\alpha + 1)$

Table 2.1: Continuity and number of degrees of freedom in a one-dimensional analysis as a function of the number of elements n_e and the basis functions order p or enrichment order p_α (for C^∞ GFEM we assume that all nodes are evenly enriched).

2.3.1 Homogeneous tensile rod under constant axial stress

The accuracy of the approximation schemes summarized in Section 2.2 is assessed by means of the analysis of the elastic rod in Figure 2.3. With reference to (2.15), the equilibrium

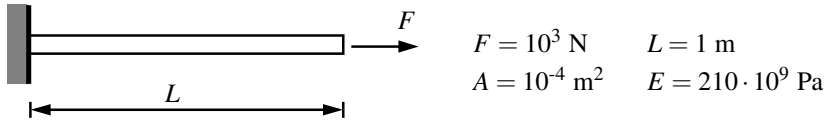


Figure 2.3: Homogeneous tensile rod under constant axial stress.

equation of the nonlocal rod is expressed as

$$\varepsilon(x) + \frac{\xi_2}{2\ell\xi_1} \int_0^L e^{-\frac{1}{\ell}|x-\bar{x}|} \varepsilon(\bar{x}) d\bar{x} = \frac{\bar{\varepsilon}}{\xi_1}, \quad (2.27)$$

where $\bar{\varepsilon} = F/AE = \bar{\sigma}/E$. Its analytical solution, derived in [10], is given by

$$\varepsilon(x) = C_1 \cosh(\kappa x) + C_2 \sinh(\kappa x) + \frac{\bar{\varepsilon}}{\xi_1} - \frac{\xi_2 \bar{\varepsilon}}{\xi_1} (1 - \cosh(\kappa x)) \quad (2.28)$$

with

$$k = \frac{1}{\ell\sqrt{\xi_1}}, \quad C_1 = C_2 k \ell \quad \text{and} \quad (2.29)$$

$$C_2 = \frac{\xi_2 \bar{\varepsilon}}{\xi_1^{3/2}} \frac{\frac{1}{k\ell} (1 - \cosh(kL)) - \sinh(kL)}{[k^2 \ell^2 \sinh(kL) + 2k\ell \cosh(kL) + \sinh(kL)]}.$$

The analytical solution is shown in Figure 2.4 for different values of ℓ and ξ_1 . Despite the constant axial stress $\bar{\sigma}$ which obeys equilibrium in the horizontal direction, the strain field exhibits boundary layers as a consequence of the assumed integro-differential model. In particular, the boundary layers grow with ξ_1 and become shaper as the material characteristic length ℓ decreases. Thus, we observe that the nonlocal parameters ξ_1 and ℓ affect the strain field and, consequently, the stiffness of the rod. On the other hand, the stress field is identical to that calculated with the local model because of equilibrium. Here and in the following, numerical results are computed for ξ_1 and ℓ/L equal to 2 and 0.01, respectively, unless mentioned otherwise.

The Lagrange approximations shown in Figure 2.5, being C^0 continuous in the displacement field, show discontinuities which disappear with mesh refinement and polynomial order increase. Moreover, cubic and quartic basis functions i) lead to spurious and periodic oscillations whose length corresponds to the finite element size, and ii) improve the accuracy of the strain field approximations at the elements boundaries. As indicated in Figure 2.6, Hermite finite elements yield oscillations similar to those just described for Lagrange finite elements. Nonetheless, their higher continuity enhances smoothness and accuracy of the numerical solution. On the other hand, high-order B-spline basis functions improve considerably the results illustrated in Figure 2.7 thanks to their smoothness and wide support. Indeed, it is noted that the oscillations are localized at the boundary area and vanish with mesh refinement. As shown in Figure 2.8, despite the basis functions having a high degree of continuity over the entire domain, periodic oscillations deeply affect the numerical solutions obtained with the C^∞ GFEM. Akin to Lagrange and Hermite finite elements, the

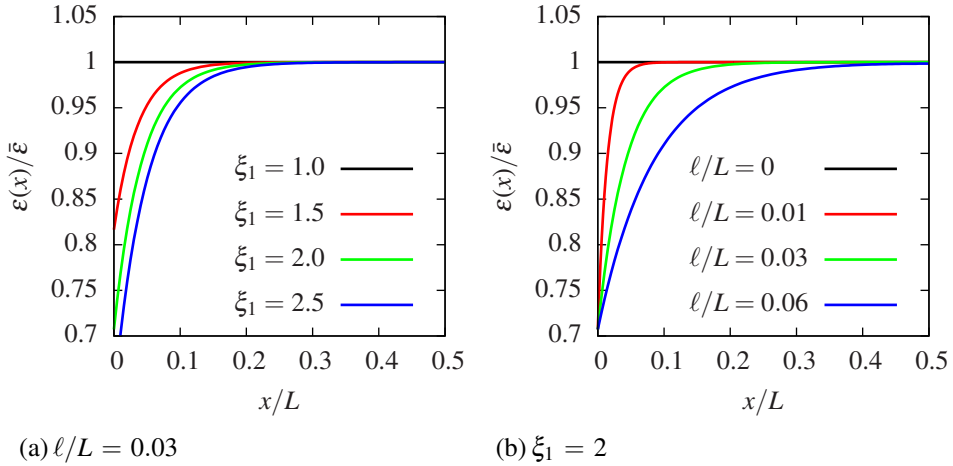


Figure 2.4: Homogeneous tensile rod under constant axial stress: exact solution for different values of constitutive parameter ξ_1 and material characteristic length ℓ (only half of the solution is plotted due to symmetry). The strain field $\varepsilon(x)$ is normalized by the maximum value $\bar{\varepsilon}$ of the local strain field.

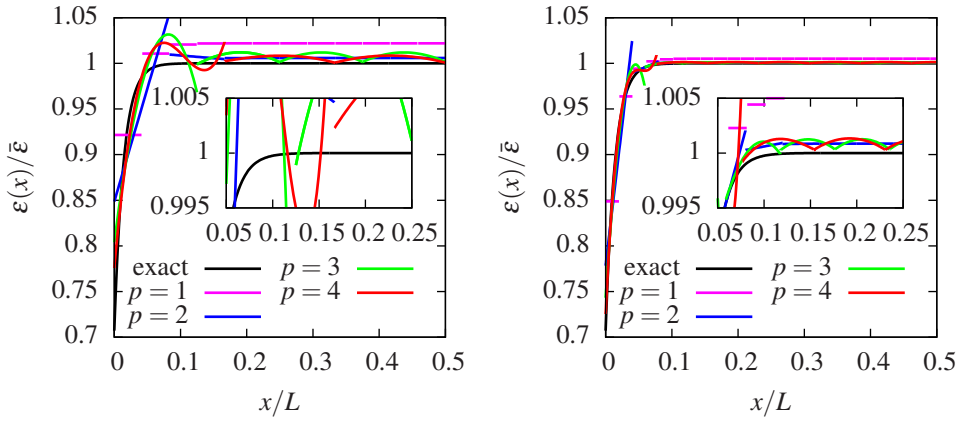
amplitude of the oscillations slightly decreases with the order of the basis functions and their period depends on the support of the basis functions as depicted in Figure 2.9. Finally, we observe that the accuracy of the numerical results rapidly improves at the elements nodes. The analysis of the source of the aforementioned oscillations is worth a deeper investigation and is out of the scope of this chapter. A detailed discussion of this problem can be found in References [13, 21, 25].

Figure 2.10 shows the relative error in energy norm. We observe that the error decreases with the order of the basis function (the polynomial enrichment in the case of the C^∞ GFEM). In particular, the relative error decreases with increasing the basis function order for Lagrange, Hermite and B-spline approximations. Furthermore, C^∞ GFEM curves are comparable with those obtained by means of Lagrange approximations: by assuming the same order of the polynomial enrichment and the Lagrange basis function, the relative error is similar. Moreover, it is worth noting that the rate of convergence is only slightly influenced by the polynomial order of the basis functions. This problem is studied in further detail in Section 2.4.1 with the strain gradient approach.

2.3.2 Homogeneous tensile rod under body force with high gradient

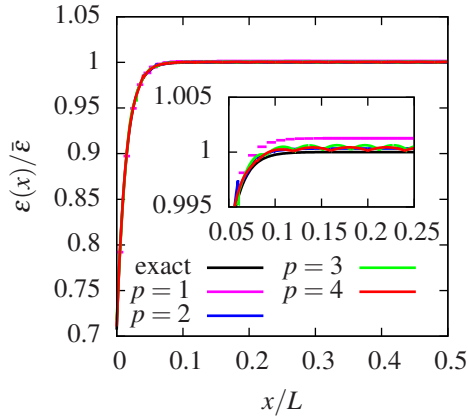
In this example, we consider the tensile rod problem shown in Figure 2.11 under the action of the body force

$$q(x) = \left[\frac{2}{\alpha^2} - \left(\frac{L-2x}{\alpha^2} \right)^2 \right] \exp \left[- \left(\frac{x-L/2}{\alpha} \right)^2 \right] \quad (2.30)$$



(a) Lagrange basis functions (25 dofs)

(b) Lagrange basis functions (50 dofs)



(c) Lagrange basis functions (100 dofs)

Figure 2.5: Integro-differential formulation: results from Lagrange approximations. The strain field $\varepsilon(x)$ is normalized by the maximum value $\bar{\varepsilon}$ of the local strain field.

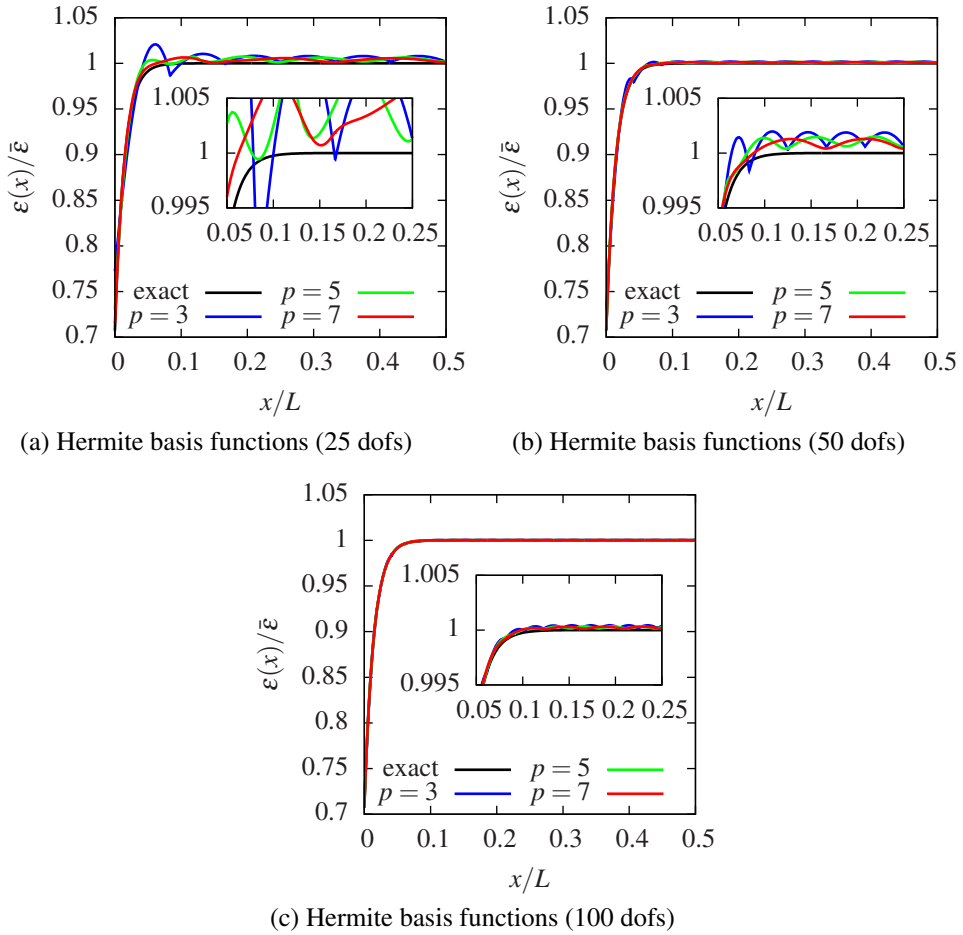
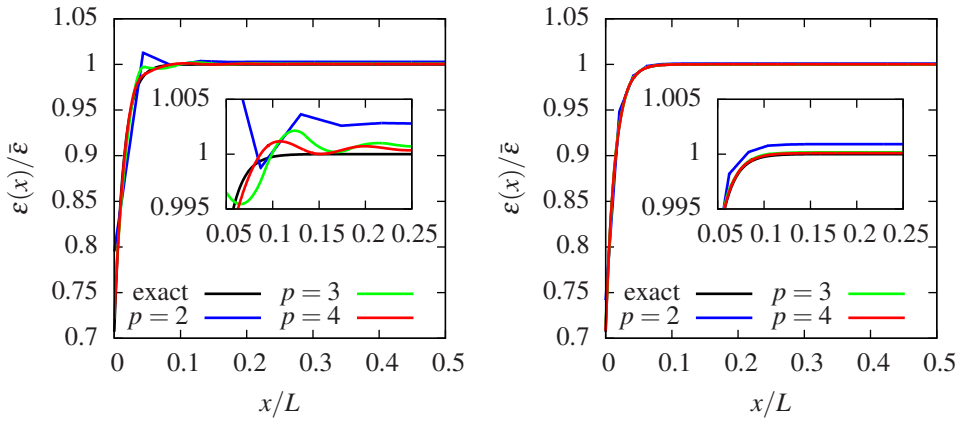
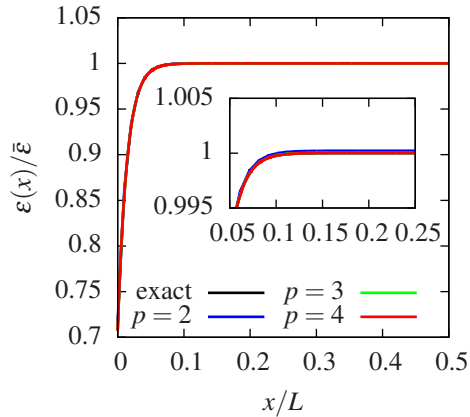


Figure 2.6: Integro-differential formulation: results from Hermite approximations. The strain field $\varepsilon(x)$ is normalized by the maximum value $\bar{\varepsilon}$ of the local strain field.



(a) B-spline basis functions (25 dofs)

(b) B-spline basis functions (50 dofs)



(c) B-spline basis functions (100 dofs)

Figure 2.7: Integro-differential formulation: results from B-spline approximations. The strain field $\varepsilon(x)$ is normalized by the maximum value $\bar{\varepsilon}$ of the local strain field.

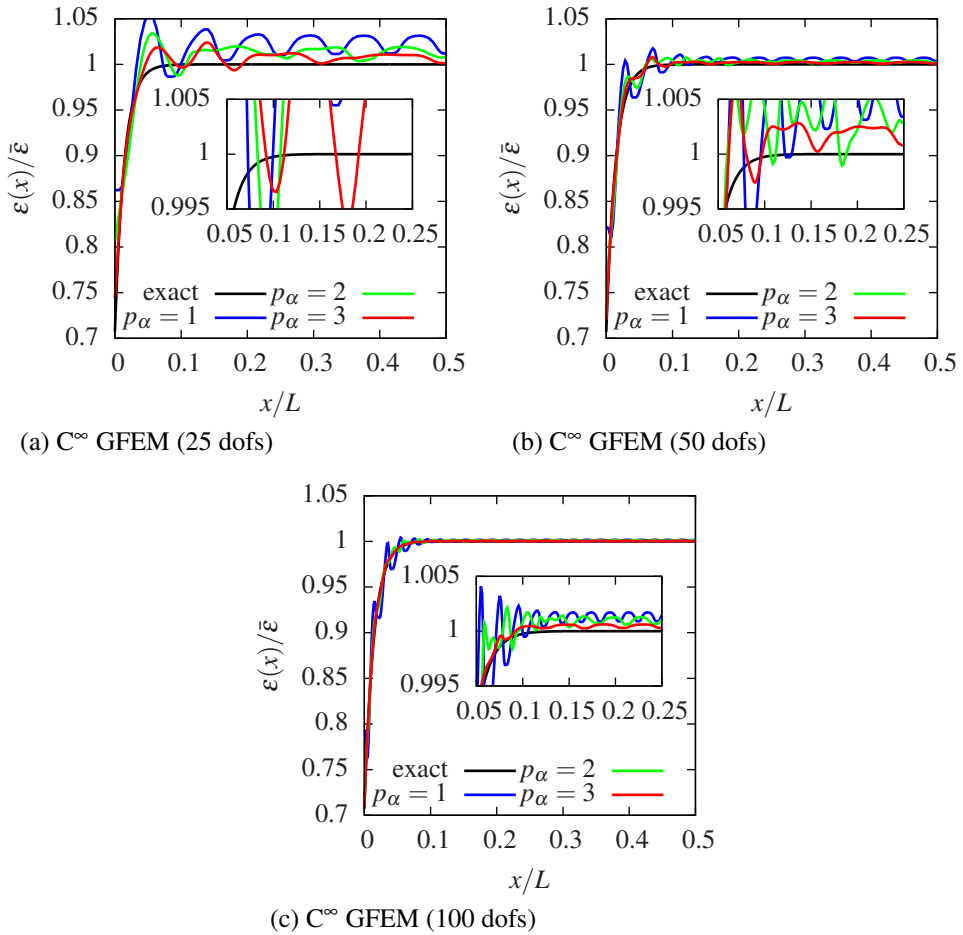
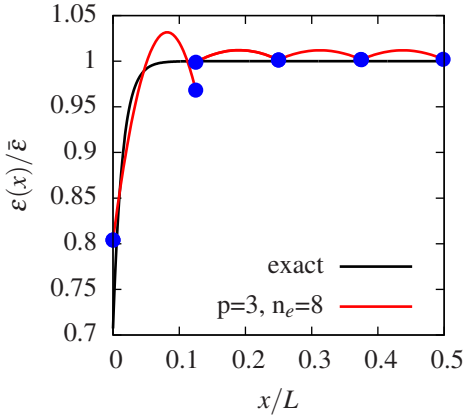
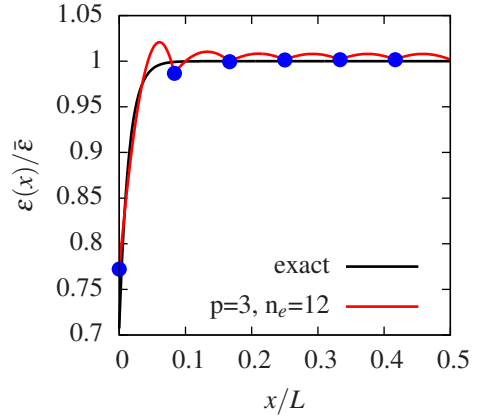


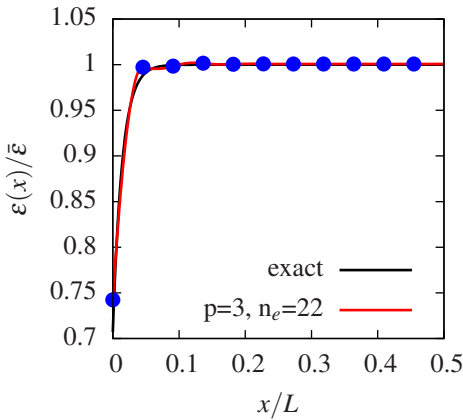
Figure 2.8: Integro-differential formulation: results from C^∞ GFEM approximations. The strain field $\varepsilon(x)$ is normalized by the maximum value $\bar{\varepsilon}$ of the local strain field.



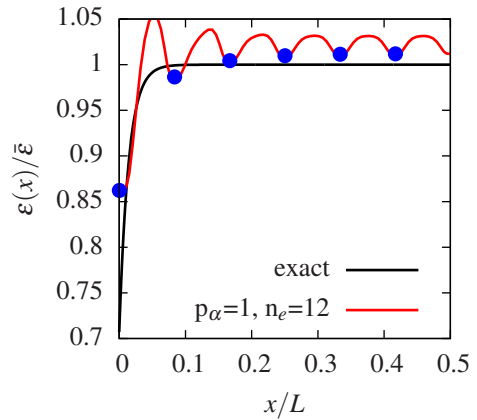
(a) Lagrange basis functions



(b) Hermite basis functions



(c) B-spline basis functions



(d) C^∞ basis functions

Figure 2.9: Integro-differential formulation: approximations computed with 25 dofs (markers denote the finite element boundaries). The strain field $\varepsilon(x)$ is normalized by the maximum value $\bar{\varepsilon}$ of the local strain field.

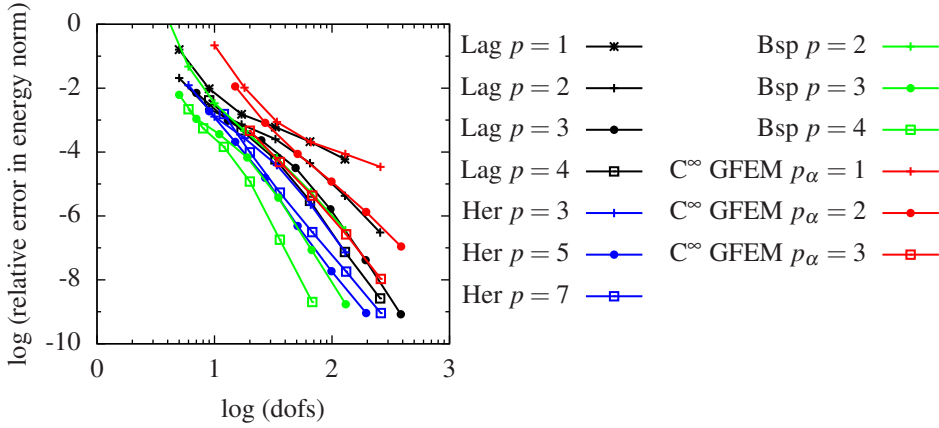


Figure 2.10: Integro-differential formulation: strain energy relative error.

which has a local area of high gradient [17]. The parameter α governs the strength of the gradient. The solution of this problem in terms of the strain field is expressed as

$$\varepsilon(x) = \frac{1}{E} \left[1 + 6 \frac{\ell^2}{\alpha^2} - \ell^2 \left(\frac{L-2x}{\alpha^2} \right)^2 \right] \frac{L-2x}{\alpha^2} \exp \left[- \left(\frac{x-L/2}{\alpha} \right)^2 \right] \quad (2.31)$$

and has been derived from (2.15) by making use of the boundary conditions [10, 34]

$$\varepsilon'(0) - \frac{\varepsilon(0)}{\ell} = \frac{q'(0)\ell - q(0)}{\xi_1 \ell EA} \quad \text{and} \quad \varepsilon'(L) + \frac{\varepsilon(L)}{\ell} = \frac{q'(L)\ell + q(L)}{\xi_1 \ell EA}. \quad (2.32)$$

As shown in Figure 2.12, low values of α (assumed equal to ℓ) yield sharper profiles of the strain field about the center of the domain. In the following analysis, we assume α/L and ℓ/L both equal to 0.01 to assess the properties of the approximation schemes described in Section 2.2 on a problem with a local area of high gradient.

As illustrated in Figures 2.13(a) and 2.13(b), Lagrange finite elements, being C^0 continuous, yield strong discontinuities and oscillations about the center of the domain. Despite the higher continuity, Hermite approximations computed with 100 dofs (Fig. 2.13(c)) present oscillations in a wide region. Nevertheless, Figure 2.13(d) shows a drastic improvement when finer discretizations are employed. The results obtained with B-spline, depicted in Figure 2.14(a) and 2.14(c), are similar to those related to Hermite approximations (a comparison is shown in Figure 2.15). Finally, Figures 2.14(b) and 2.14(d) show wide oscillations in C^∞ GFEM approximations irrespective of the element size.

As a general remark, this numerical study shows that basis functions with high continuity tend to generate spurious oscillations on a large portion of the problem domain when employed on a coarse discretization. Such observation is in agreement with the results reported by Dolbow et al. [17] who used meshless approximations for the corresponding local version of the same problem.

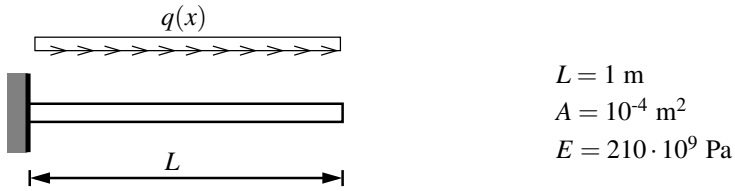


Figure 2.11: Homogeneous tensile rod under the action of a body force.

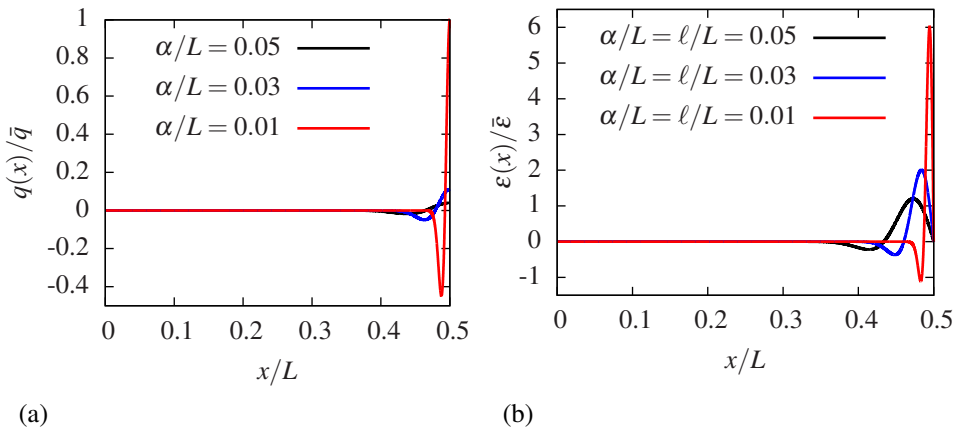


Figure 2.12: Homogeneous tensile rod under body force with high gradient: normalized (a) load distribution and (b) strain field solution (\bar{q} and $\bar{\epsilon}$ are the maximum value of $q(x)$ and $\epsilon(x)$ for $\alpha/L = 0.01$ and $\ell = 0$, respectively). Since the load distribution is symmetric and the strain field is antisymmetric, only half domain is shown.

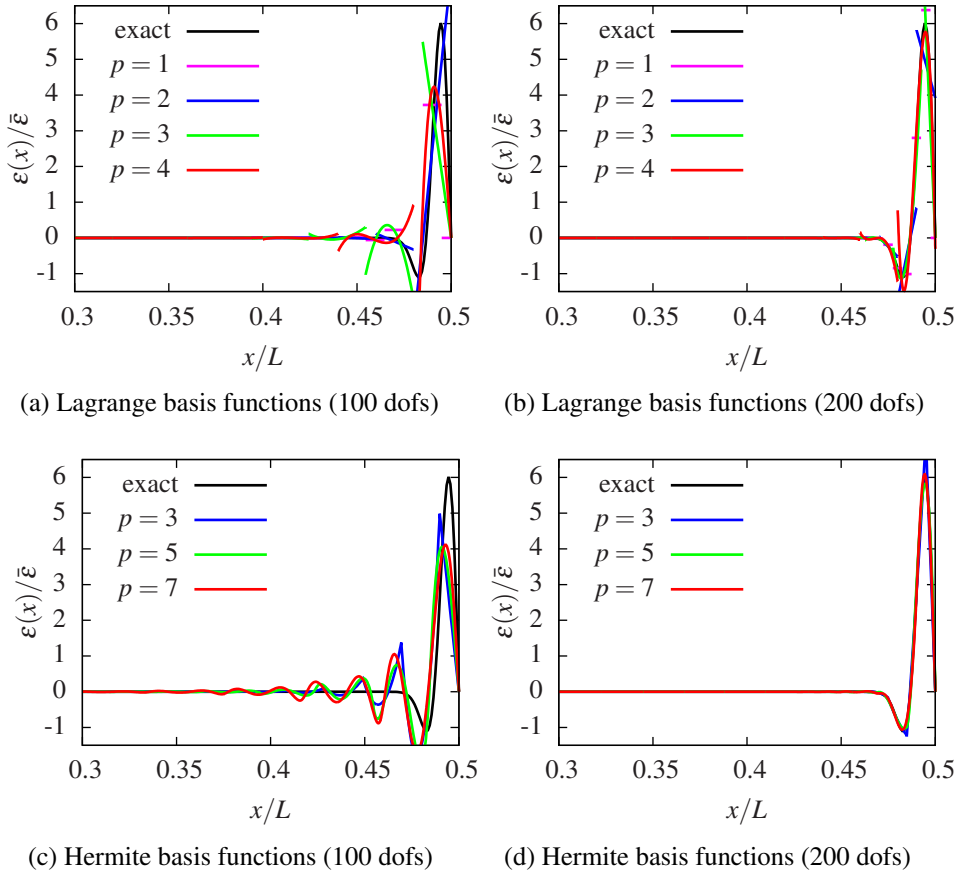
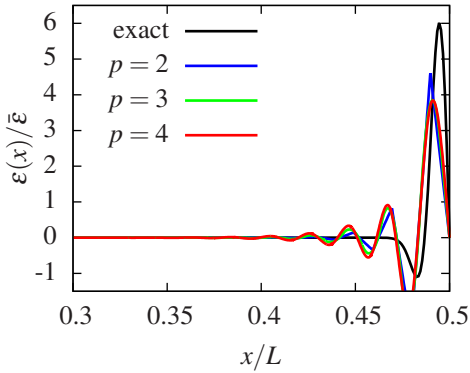
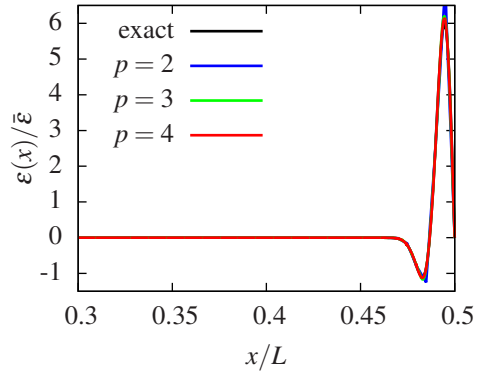


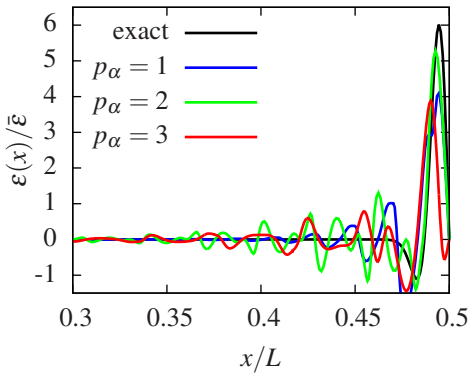
Figure 2.13: Elastic tensile rod under body force with high gradient: results with Lagrange and Hermite basis functions. The strain field $\varepsilon(x)$ is normalized by the maximum value $\bar{\varepsilon}$ of the local strain field.



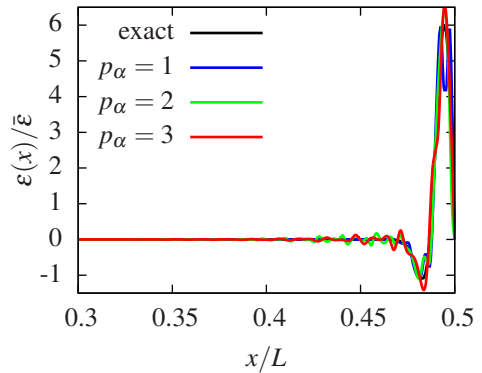
(a) B-spline basis functions (100 dofs)



(b) B-spline basis functions (200 dofs)



(c) C[∞] GFEM (100 dofs)



(d) C[∞] GFEM (200 dofs)

Figure 2.14: Elastic tensile rod under body force with high gradient: results with B-spline basis functions and C[∞] GFEM. The strain field $\varepsilon(x)$ is normalized by the maximum value $\bar{\varepsilon}$ of the local strain field.

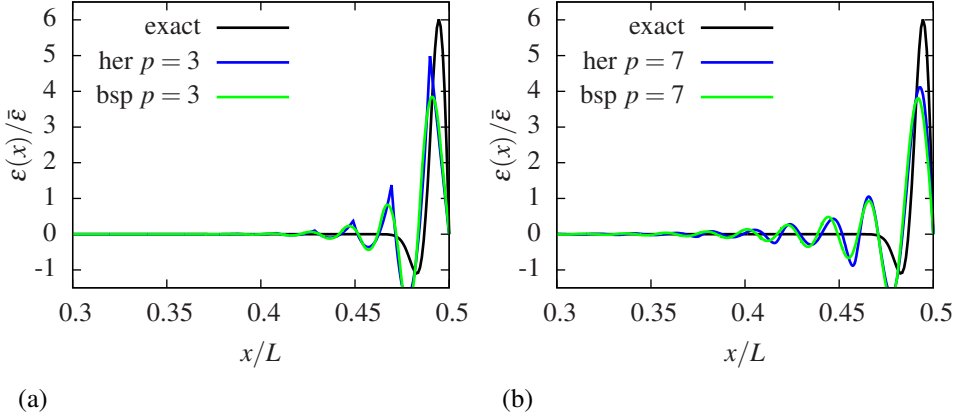


Figure 2.15: Elastic tensile rod under body force with high gradient: (a) cubic and (b) septic Hermite and B-spline approximation with 100 dofs. The strain field $\varepsilon(x)$ is normalized by the maximum value $\bar{\varepsilon}$ of the local strain field.

2.4 Strain gradient formulation

In this section, we consider the procedure outlined by Vardoulakis and Sulem [38] to derive the strain gradient governing equations of an elastic tensile rod. In a one-dimensional setting, the total potential energy

$$\Pi(u) = \frac{1}{2} \int_0^L \sigma(x) \varepsilon(x) \, dx + \left(\mu(x) \varepsilon(x) \right) \Big|_{\Gamma} - \int_0^L q(x) u(x) \, dx, \quad (2.33)$$

where the axial stress $\sigma(x)$ and the higher-order stress $\mu(x)$ are defined by the constitutive equations

$$\sigma(x) = E(\varepsilon(x) - g^2 \nabla^2 \varepsilon(x)) \quad \text{and} \quad \mu(x) = g^2 E \nabla \varepsilon(x), \quad (2.34)$$

with g the length scale parameter related to the volumetric elastic strain energy. The first variation of the total potential energy is then expressed as

$$\begin{aligned} \delta \Pi(u) &= \int_0^L \left[EA(u'(x) - g^2 u'''(x)) \delta u'(x) \right] dx + \left(EA g^2 u''(x) \delta u'(x) \right) \Big|_{\Gamma} \\ &\quad - \int_0^L q(x) \delta u(x) \, dx \\ &= - \int_0^L \left[EA(u''(x) - g^2 u''''(x)) + q(x) \right] \delta u(x) \, dx \\ &\quad + \left[g^2 EA u''(x) \delta u'(x) - EA(u'(x) - g^2 u'''(x)) \delta u(x) \right] \Big|_{\Gamma} \end{aligned} \quad (2.35)$$

and holds for any δu and $\delta u'$. Consequently, by means of the fundamental lemma of variational calculus and assuming δu and $\delta u'$ arbitrary and vanishing at the boundaries, the

following governing equations are obtained:

$$EA(u''(x) - g^2 u''''(x)) + q(x) = 0 \quad \forall x \in [0, L], \quad (2.36a)$$

$$EA(u'(x) - g^2 u'''(x)) = \bar{N} \quad \text{on } \Gamma_t, \quad (2.36b)$$

$$u(x) = \bar{u} \quad \text{on } \Gamma_u, \quad (2.36c)$$

$$g^2 EAu''(x) = \bar{N}^* \quad \text{on } \Gamma_{r^*}, \text{ and} \quad (2.36d)$$

$$u'(x) = \bar{u}' \quad \text{on } \Gamma_{u'}, \quad (2.36e)$$

where $\Gamma_{u'}$ and Γ_{r^*} denote the boundary portions where axial strains and nonclassical (or double) tractions are prescribed. In particular, $\Gamma_u \cup \Gamma_t = \Gamma$, $\Gamma_u \cap \Gamma_t = \emptyset$, $\Gamma_{u'} \cup \Gamma_{r^*} = \Gamma$ and $\Gamma_{u'} \cap \Gamma_{r^*} = \emptyset$ must hold. From (2.36b)-(2.36e), it is worth noting that, beside the prescribed axial forces and displacements, either the nonclassical (or double) axial force N^* or the axial strain $u'(x)$ need to be specified at the boundary. It follows that the enforcement of boundary conditions in strain gradient model is complicated by the presence of higher-order stresses whose value is not known a priori [8, 10, 33].

The equilibrium configuration of the one-dimensional rod can be found starting from (2.35) and imposing $\delta\Pi(u) = 0$ which implies

$$\begin{aligned} \int_0^L EA \left[u'(x) \delta u'(x) + g^2 u''(x) \delta u''(x) \right] dx &= \int_0^L q(x) \delta u(x) dx \\ &+ \left[EA(u'(x) - g^2 u'''(x)) \delta u(x) - EA g^2 u''(x) \delta u'(x) \right] \Big|_{\Gamma}. \end{aligned} \quad (2.37)$$

Hence, with reference to (2.37), the axial displacement $u(x)$ and its first variation $\delta u(x)$ are kinematically admissible if [37]

$$u(x) \in \mathcal{S} \text{ with } \mathcal{S} = \{u(x) \mid u(x) \in H^2, u = \bar{u} \text{ on } \Gamma_u, u' = \bar{u}' \text{ on } \Gamma_{u'}\} \quad (2.38a)$$

and

$$\delta u(x) \in \mathcal{V} \text{ with } \mathcal{V} = \{\delta u(x) \mid \delta u(x) \in H^2, \delta u = 0 \text{ on } \Gamma_u, \delta u' = 0 \text{ on } \Gamma_{u'}\}. \quad (2.38b)$$

The discrete form of the governing equations can be easily obtained and yields the stiffness matrix

$$\mathbf{K} = \sum_{e=1}^{n_{el}} \int_{x_1^e}^{x_2^e} \left(\mathbf{B}^{eT}(x) EA \mathbf{B}^e(x) + g^2 \frac{d\mathbf{B}^{eT}}{dx}(x) EA \frac{d\mathbf{B}^e}{dx}(x) \right) dx \quad (2.39a)$$

and the force vector

$$\begin{aligned} \mathbf{f} &= \sum_{e=1}^{n_{el}} \left[\mathbf{f}_{\Omega}^e + \mathbf{f}_{\Gamma}^e \right] \\ &= \sum_{e=1}^{n_{el}} \left[\int_{x_1^e}^{x_2^e} \mathbf{N}^{eT}(x) q(x) dx + \left(\mathbf{N}^{eT}(x) N(x) - \mathbf{B}^{eT}(x) N^*(x) \right) \Big|_{\Gamma} \right]. \end{aligned} \quad (2.39b)$$

The numerical approximation of $u(x)$ should be C^1 -continuous within the domain in order to belong to the class of kinematically admissible displacements. Accordingly, standard C^0 basis functions such as Lagrangian basis functions, cannot be employed. Cubic Hermite basis

functions, quadratic B-spline basis functions and C^∞ GFEM with quadratic enrichments are the first approximations to satisfy such continuity requirement. Alternatively, mixed finite element formulations, which require only C^0 -continuity, could be employed [3, 36]. However, these methods introduce the issue of the Ladyzenskaja-Babuška-Brezzi stability condition which is not present in the formulation adopted here.

2.4.1 Homogeneous tensile rod under constant axial stress

In this example we reconsider the problem examined in Section 2.3.1. Seeking for the same analytical solution, we set

$$g = \ell \sqrt{\bar{\xi}_1} \quad (2.40)$$

and use the following set of classical and nonclassical boundary conditions [10]:

$$u(0) = 0, \quad (2.41a)$$

$$N(L) = EA(u'(L) - g^2 u'''(L)) = F, \quad (2.41b)$$

$$u''(0) - \frac{1}{\ell} u'(0) = -\frac{1}{\ell} \frac{\bar{\xi}_1}{\xi_1}, \quad \text{and} \quad (2.41c)$$

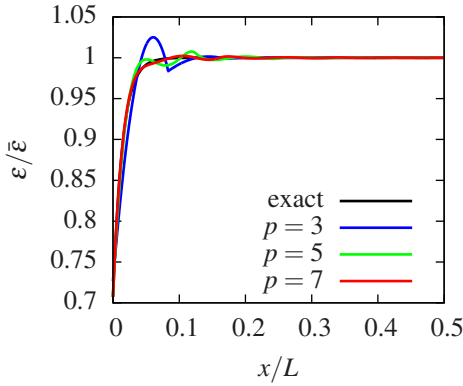
$$u''(L) + \frac{1}{\ell} u'(L) = \frac{1}{\ell} \frac{\bar{\xi}_1}{\xi_1}. \quad (2.41d)$$

The problem is studied by means of Hermite and B-spline finite elements and C^∞ GFEM. As reported in Figure 2.16, oscillations appear close to the boundary and disappear with h - and p -refinement of Hermite and B-spline approximations or with high-order enrichments in the case of C^∞ GFEM. In addition, as observed in Section 2.3.1, we notice that B-spline basis functions yield oscillations with the lowest amplitude whereas C^∞ GFEM lead to the highest.

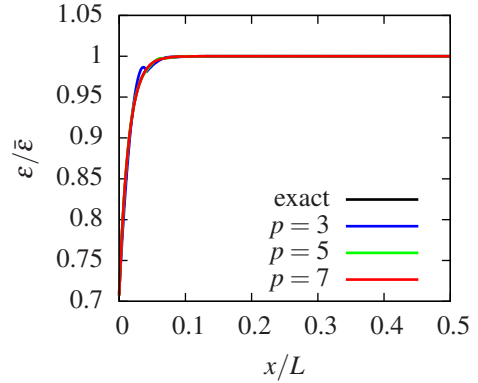
Figure 2.17 shows the relative error in energy norm with respect to the total number of degrees of freedom. It is evident how high-order Hermite and B-spline approximations considerably improve the accuracy of the numerical solution as compared to C^∞ GFEM. Furthermore, from the results obtained from Hermite and B-spline basis functions of the same order, we observe that continuity has a positive influence on the absolute error as discussed in Section 2.3.1.

2.4.2 Inhomogeneous tensile rod under constant axial stress

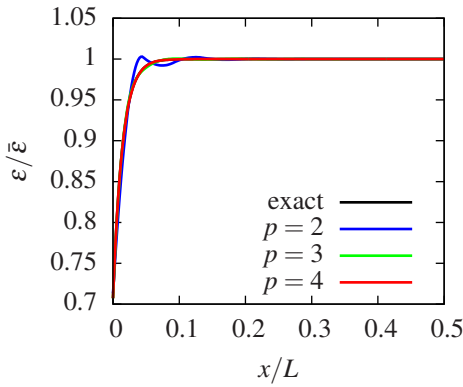
The strain gradient formulation has been widely used to model discontinuities such as those related to material heterogeneity [7, 8, 33]. In this last example, we consider the bimaterial rod depicted in Figure 2.18. We assume constant cross section A and length scale g along the rod, whereas the Young's modulus is chosen equal to E_1 for $x < L/2$ and E_2 for $x \geq L/2$. The analytical solution of the problem [8] is obtained with reference to the following boundary



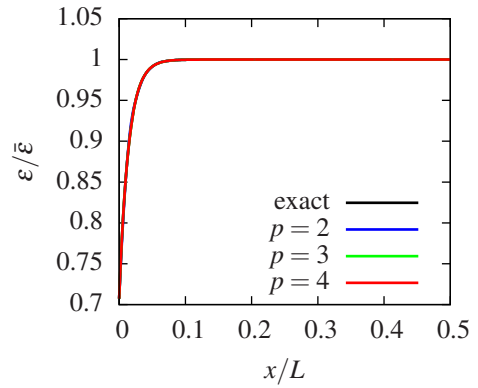
(a) Hermite basis functions (25 dofs)



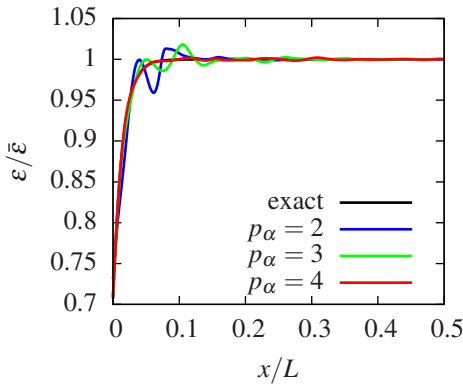
(b) Hermite basis functions (50 dofs)



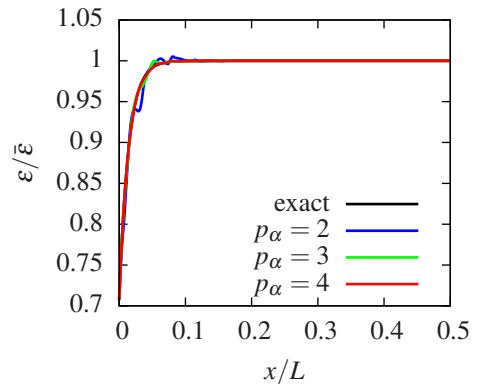
(c) B-spline basis functions (25 dofs)



(d) B-spline basis functions (50 dofs)



(e) C^∞ GFEM (25 dofs)



(f) C^∞ GFEM (50 dofs)

Figure 2.16: Strain gradient formulation: results with Hermite basis functions, B-spline basis functions and C^∞ GFEM. The strain field $\varepsilon(x)$ is normalized by the maximum value $\bar{\varepsilon}$ of the local strain field.

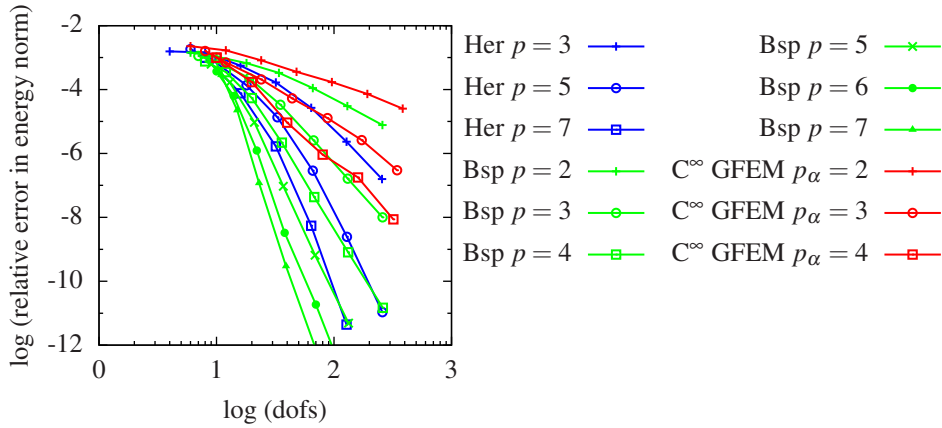


Figure 2.17: Strain gradient formulation: strain energy relative error.

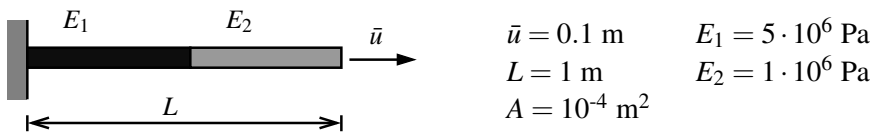


Figure 2.18: Strain gradient inhomogeneous tensile rod.

conditions:

$$u(0) = 0, \quad (2.42a)$$

$$u''(0) = 0, \quad (2.42b)$$

$$\sigma(L/2)^- = \sigma(L/2)^+, \quad (2.42c)$$

$$E_1 u''(L/2)^- = E_2 u''(L/2)^+, \quad (2.42d)$$

$$u(L) = \bar{u} \quad \text{and} \quad (2.42e)$$

$$u''(L) = 0. \quad (2.42f)$$

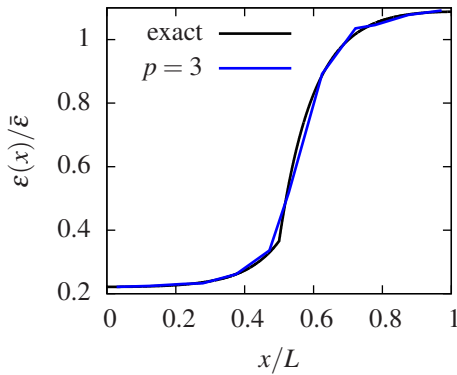
Due to (2.42c) and (2.42d), the displacement field is C^1 -continuous at the material interface. The numerical approximation of the solution should therefore satisfies such continuity requirement at $x = L/2$. Accordingly, we can use cubic Hermite basis functions since they are C^1 -continuous at the element boundaries. In addition, as discussed in Section 2.2.1, B-spline approximations can be C^1 -continuous at a given point by making use of $p - 1$ multiple knots at that position (p is the order of the basis functions). On the other hand, C^∞ GFEM cannot be used since they are C^∞ -continuous along the whole domain.

As depicted in Figures 2.19 and 2.20, the numerical approximations of $u'(x)$ and $u''(x)$ do not present oscillations even with coarse discretizations. However, high-order B-spline basis functions yield much better results as compared to those obtained from Hermite finite elements. Indeed, this is consistent with the results illustrated in Figure 2.21 where the numerical accuracy is assessed in terms the strain energy norm. Here, the basis function continuity significantly decreases the relative error and considerably increases the convergence rate of the numerical results.

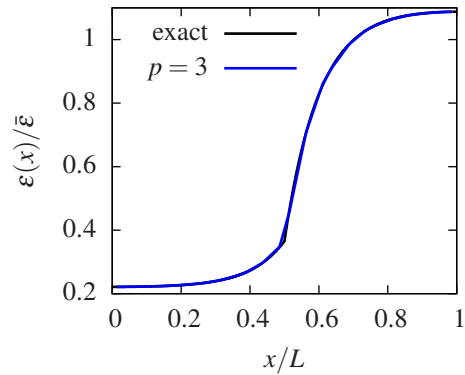
2.5 Discussion

The accuracy of high order approximation schemes in solving nonlocal elastic problems has been examined in Section 2.3 and 2.4. Beside classical Lagrange and Hermite finite elements, we have considered B-spline finite elements and C^∞ GFEM. As described in Section 2.2.1, B-spline basis functions are defined on a set of highly continuous polynomial basis functions on wide supports. On the other hand, C^∞ GFEM are built using C^∞ Shepard PoU functions with the same support as standard finite elements. However, the computational cost of these GFEM basis functions is higher due to the difficulty in numerically integrating functions based on Shepard PoU.

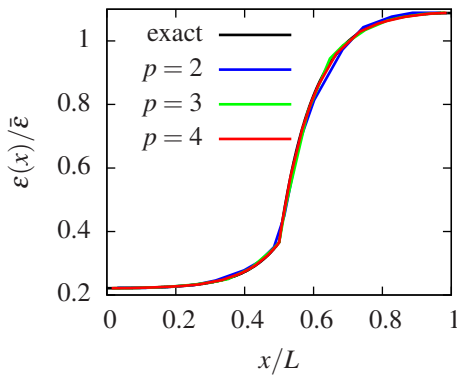
The numerical results obtained in this study show that the accuracy of the finite element solution does not only depend on the approximation scheme used and on its continuity. In fact, the constitutive assumptions play an important role. For the homogeneous tensile rod with constant stress, the integro-differential model and the strain gradient model yield the same analytical solution. However, both the algebraic structure of the constitutive models and the numerical issues associated with the corresponding approximation scheme are different. In particular, for the integro-differential formulation, oscillations in the solution obtained with Lagrange, Hermite and C^∞ GFEM approximations have been observed along the whole domain, whereas for the strain gradient case they were limited to the boundary area. Furthermore, as indicated in Table 2.2, the convergence rate of Hermite and B-spline



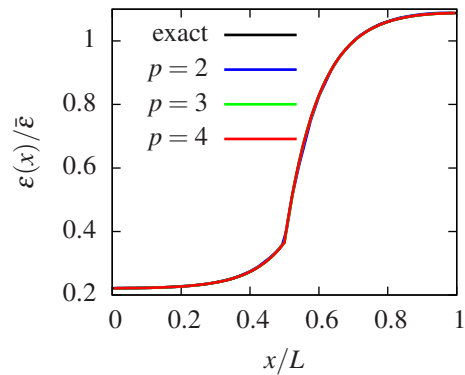
(a) Hermite basis functions (10 dofs)



(b) Hermite basis functions (20 dofs)

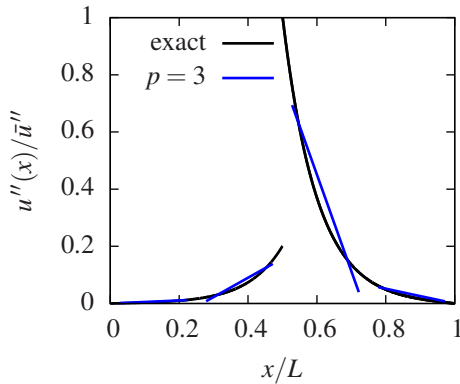


(c) B-spline basis functions (10 dofs)

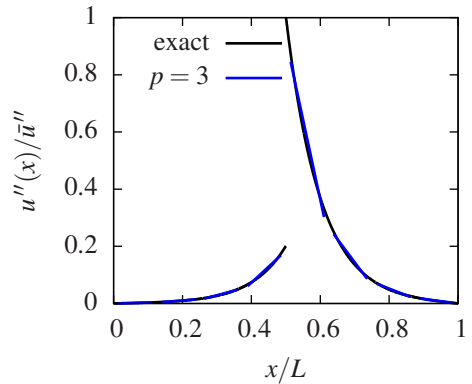


(d) B-spline basis functions (20 dofs)

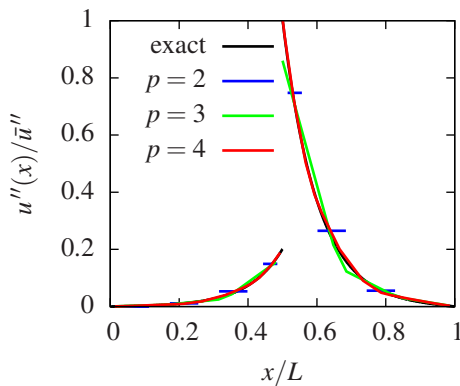
Figure 2.19: Strain gradient inhomogeneous tensile rod: strain field of the inhomogeneous tensile rod obtained with cubic Hermite and B-spline finite elements. The strain field $\varepsilon(x)$ is normalized by the maximum value $\bar{\varepsilon}$ of the local strain field.



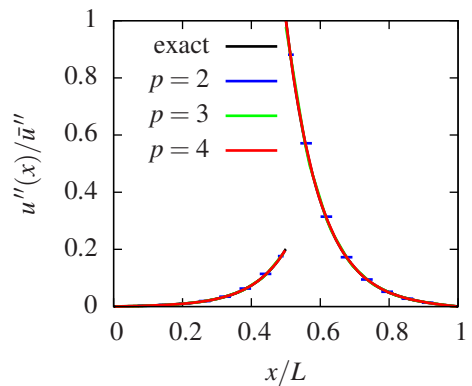
(a) Hermite basis functions (10 dofs)



(b) Hermite basis functions (20 dofs)



(c) B-spline basis functions (10 dofs)



(d) B-spline basis functions (20 dofs)

Figure 2.20: Strain gradient inhomogeneous tensile rod: second derivative of the displacement field of the inhomogeneous tensile rod obtained with cubic Hermite and B-spline finite elements. The solution field $u''(x)$ is normalized by its maximum value ($u''(x)$ is equal to zero throughout the domain in the local case).

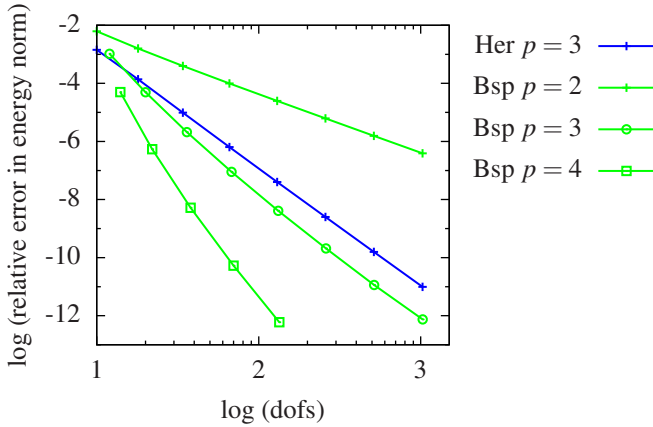


Figure 2.21: Strain gradient inhomogeneous tensile rod: strain energy relative error.

approximations computed with the integro-differential formulation barely increases with the order of the basis functions which is clearly in contrast with those obtained from the strain gradient model. Therefore, the knowledge of the analytical solution alone is not sufficient to decide a priori the best approximation scheme. Especially noteworthy is the similarity of the C^∞ GFEM convergence rates to those computed for the Lagrange finite elements —note however that beside the polynomial enrichments considered in this chapter, better GFEM convergence rates might be obtained from enrichments tailored to the problem being solved.

We have observed that the error in energy norm decreases with the continuity of the basis functions. However, highly continuous approximations suffer from some drawbacks. Firstly, as showed in Section 2.3.2, high order basis functions led to high oscillations when the exact solution of the problem presents non-monotonic sharp gradients far from the boundaries. For this class of problems, very fine discretizations are required in order to reduce these oscillations. Secondly, C^∞ GFEM and, in general, Hermite finite elements are not suitable when the continuity of the exact solution decreases at a prescribed point. On the other hand, arbitrarily continuous B-spline basis functions easily overcome this problem by means of multiple knots insertion. Furthermore, for the example examined in Section 2.4.2, B-spline convergence rates increase with the order of the basis functions as illustrated in Table 2.2.

2.6 Conclusions

A set of one-dimensional integro-differential and strain gradient boundary-value problems was studied by means of the finite element method equipped with classical and high-order basis functions. Accuracy and convergence properties of the approximation schemes were assessed against analytical solutions.

The main conclusions of this study can be summarized as follows:

- (i) in general, high-order basis functions lead to spurious oscillations in integro-differential formulations although the relative error in energy norm decreases; and

	order	cont.	IDH	SGH	SGN
Lagrange	1	C^0	1.85	-	-
	2	C^0	3.84	-	-
	3	C^0	5.66	-	-
	4	C^0	4.95	-	-
Hermite	3	C^1	4.06	3.88	3.62
	5	C^2	4.06	7.84	-
	7	C^3	4.07	11.14	-
B-spline	2	C^1	4.10	2.00	2.01
	3	C^2	4.14	4.08	3.96
	4	C^3	4.20	5.90	4.68
C^∞ GFEM	1	C^∞	1.32	-	-
	2	C^∞	3.62	1.54	-
	3	C^∞	4.20	3.16	-

Table 2.2: Convergence rates in energy norm for the integro-differential homogeneous rod (IDH), the strain gradient homogeneous rod (SGH) and the strain gradient nonhomogeneous rod (SGN) with constant stress studied in Sections 2.3.1, 2.4.1 and 2.4.2, respectively. The convergence rate is calculated as $-\Delta(\log \|e\|_E)/\Delta(\log N)$ using the last two data points of each curve and by taking $\|e\|_E$ as the relative error in energy norm and N as the total number of degrees of freedom.

- (ii) among the basis functions considered here, B-spline basis functions are the most efficient at modeling problems in the presence of nonlocal and gradient constitutive laws, provided that a) the knots multiplicity is increased at material interfaces, and b) the mesh is sufficiently refined in the case of sharp body forces.

Mesh refinement and enrichment functions based on *a-posteriori* error estimates could be used to guarantee convergence of the finite element solutions instead of uniform refinement which may not be practical to reach acceptable error levels.

Bibliography

- [1] S. Adhikari, T. Murmu, and M. A. McCarthy. Dynamic finite element analysis of axially vibrating nonlocal rods. *Finite Elements in Analysis and Design*, 63:42–50, 2013.
- [2] E. Aifantis. On the role of gradients in the localization of deformation and fracture. *International Journal of Engineering Science*, 30:1279–1299, 1992.
- [3] E. Amanatidou and N. Aravas. Mixed finite element formulations of strain-gradient elasticity problems. *Computer Methods in Applied Mechanics and Engineering*, 191:1723–1751, 2002.
- [4] H. Askes and E. C. Aifantis. Numerical modeling of size effects with gradient elasticity – Formulation, meshless discretization and examples. *International Journal of Fracture*, 117:347–358, 2002.
- [5] H. Askes and E. C. Aifantis. Gradient elasticity and flexural wave dispersion in carbon nanotubes. *Physical Review B*, 80:195412, 2009.
- [6] H. Askes and E. C. Aifantis. Gradient elasticity in statics and dynamics: An overview of formulations, length scale identification procedures, finite element implementations and new results. *International Journal of Solids and Structures*, 48:1962–1990, 2011.
- [7] H. Askes, A. S. J. Suiker, and L. J. Sluys. A classification of higher-order strain-gradient models – linear analysis. *Archive of Applied Mechanics*, 72:171–188, 2002.
- [8] H. Askes, I. Morata, and E. C. Aifantis. Finite element analysis with staggered gradient elasticity. *Computers and Structures*, 86:1266–1279, 2008.
- [9] M. Aydogdu and S. Filiz. Modeling carbon nanotube-based mass sensors using axial vibration and nonlocal elasticity. *Physica E: Low-dimensional Systems and Nanostructures*, 43:1229–1234, 2011.
- [10] E. Benvenuti and A. Simone. One-dimensional nonlocal and gradient elasticity: Closed-form solution and size effect. *Mechanics Research Communications*, 48:46–51, 2013.

- [11] M. J. Borden, M. A. Scott, J. A. Evans, and T. J. R. Hughes. Isogeometric finite element data structures based on Bézier extraction of NURBS. *International Journal of Fracture*, 87:15–47, 2011.
- [12] M. G. Cox. The numerical evaluation of B-splines. *Journal of the Institute of Mathematics and its Applications*, 10:134–149, 1972.
- [13] G. Dahlquist and Å. Björck. *Numerical Methods*. Prentice-Hall, 1974.
- [14] C. S. de Barcellos, P. T. R. Mendoça, and C. A. Duarte. A C^k continuous generalized finite element formulation applied to laminated Kirchhoff plate model. *Computational Mechanics*, 44:377–393, 2009.
- [15] C. de Boor. On calculating with B-splines. *Journal of Approximation Theory*, 6:50–62, 1972.
- [16] C. de Falco, A. Reali, and R. Vázquez. GeoPDEs: A research tool for Isogeometric Analysis of PDEs. *Advances in Engineering Software*, 42:1020–1034, 2011.
- [17] J. Dolbow and T. Belytschko. Numerical integration of the Galerkin weak form in meshfree methods. *Computational Mechanics*, 23:219–230, 1999.
- [18] C. A. Duarte, D.-J. Kim, and D. M. Quaresma. Arbitrarily smooth generalized finite element approximations. *Computer Methods in Applied Mechanics and Engineering*, 196:33–56, 2006.
- [19] H. C. Edwards. C^∞ finite element basis functions. Technical report, TICAM Report 96-45, The University of Texas at Austin, 1996.
- [20] H.C. Edwards. A parallel infrastructure for scalable adaptive finite element methods and its application to least squares c^∞ collocation. PhD dissertation, The University of Texas at Austin, May 1997. Austin, TX, USA.
- [21] E. Emmrich and O. Weckner. Analysis and numerical approximation of an integro-differential equation modeling non-local effects in linear elasticity. *Mathematics and Mechanics of Solids*, 12:363–384, 2007.
- [22] A. C. Eringen. On differential equations of nonlocal elasticity and solutions of screw dislocation and surface waves. *Journal of Applied Physics*, 54:4703–4710, 1983.
- [23] A. C. Eringen. *Nonlocal Continuum Field Theories*. Springer-Verlag, 2002.
- [24] P. Fischer, M. Klassen, J. Mergheim, P. Steinmann, and R. Müller. Isogeometric analysis of 2D gradient elasticity. *Computational Mechanics*, 47:325–334, 2011.
- [25] D. Gottlieb and C. W. Shu. On the Gibbs phenomenon and its resolution. *SIAM Review*, 39:644–668, 1997.
- [26] K. Hollig. *Finite Element Methods with B-splines*. SIAM, 2003.

- [27] T. J. R. Hughes, J. A. Cottrell, and Y. Bazilevs. Isogeometric analysis: CAD, finite elements, NURBS, exact geometry and mesh refinement. *Computer Methods in Applied Mechanics and Engineering*, 194:4135–4195, 2005.
- [28] J. Kiendl, K.-U. Bletzinger, J. Linhard, and R. Wüchner. Isogeometric shell analysis with Kirchhoff-Love elements. *Computer Methods in Applied Mechanics and Engineering*, 198:3902–3914, 2009.
- [29] J. K. Phadikar and S. C. Pradhan. Variational formulation and finite element analysis for nonlocal elastic nanobeams and nanoplates. *Computational Materials Science*, 49:492–499, 2010.
- [30] L. A. Piegl and W. Tiller. *The NURBS Book*. Springer, 1997.
- [31] A. A. Pisano, A. Sofi, and P. Fuschì. Nonlocal integral elasticity: 2D finite element based solutions. *International Journal of Solids and Structures*, 46:3836–3849, 2009.
- [32] C. Polizzotto. Nonlocal elasticity and related variational principles. *International Journal of Solids and Structures*, 38:7359–7380, 2001.
- [33] C. Polizzotto. Gradient elasticity and nonstandard boundary conditions. *International Journal of Solids and Structures*, 40:7399–7423, 2003.
- [34] A. D. Polyanin and A. V. Manzhirov. *Handbook of Integral Equations*. CRC Press, 1998.
- [35] C. M. C. Roque, A. J. M. Ferreira, and J. N. Reddy. Analysis of Timoshenko nanobeams with a nonlocal formulation and meshless method. *International Journal of Engineering Science*, 49:976–984, 2011.
- [36] J. Y. Shu, W. E. King, and N. A. Fleck. Finite elements for materials with strain gradient effect. *International Journal for Numerical Methods in Engineering*, 44:373–391, 1999.
- [37] B. Szabó and I. Babuška. *Finite element analysis*. John Wiley & Sons, Inc., 1991.
- [38] I. Vardoulakis and J. Sulem. *Bifurcation Analysis in Geomechanics*. Chapman and Hall, 1995.
- [39] C. V. Verhoosel, M. A. Scott, T. J. R. Hughes, and R. de Borst. An isogeometric analysis approach to gradient damage models. *International Journal for Numerical Methods in Engineering*, 86:115–134, 2011.
- [40] Y. Q. Zhang, G. R. Liu, and X. Y. Xie. Free transverse vibrations of double-walled carbon nanotubes using a theory of nonlocal elasticity. *Physical Review B*, 71:195404, 2005.

Chapter 3

One-dimensional nonlocal elasticity for tensile single-walled CNTs: A molecular structural mechanics characterization*

The parameters required for modeling tensile single-walled carbon nanotubes (CNTs) with a nonlocal rod model are estimated. Molecular structural mechanics (MSM) simulations are carried out for the mechanical analysis of single-walled CNTs with different diameter, length and chirality. Representative axial strain fields are then used in a parameter estimation procedure as reference solutions to tailor a nonlocal rod model. Obtained nonlocal parameters are further validated by comparing the total strain energy of MSM reference solutions and corresponding nonlocal rod solutions. The effect of size and chirality on the optimal value of the estimated parameters is discussed in details. Analytical relations between nonlocal parameters and geometry of the single-walled CNTs are obtained.

3.1 Introduction

Fundamental insight into the behavior of carbon nanotubes (CNTs) is customarily obtained with atomistic simulations [35]. Although accurate, these simulations are usually computationally intensive and not particularly suited for the analysis of long CNTs or more complex systems such as CNT networks or composites. Here, we propose a one-dimensional nonlocal rod model which is kinematically and energetically equivalent to a generic axially loaded single-walled carbon nanotube (CNT).

The most used atomistic approaches for the analysis of carbon nanotubes (CNTs) include *ab initio* calculations [41], molecular dynamics [24], and molecular mechanics [3]. Although accurate, the application of these procedures is limited to small-scale atomistic systems. In an effort to decrease the computational effort of atomistic simulations, Li and Chou [22] proposed a simple and efficient approach, referred to as molecular structural mechanics (MSM), which combines molecular mechanics and classical structural mechanics. In MSM, CNTs are modeled as space frame structures in which beam and spring elements replace covalent

* *Reproduced from:* M. Malagù, E. Benvenuti and A. Simone, One-dimensional nonlocal elasticity for tensile single-walled carbon nanotubes: A molecular structural mechanics characterization, *European Journal of Mechanics-A/Solids*, 54:160–170, 2015.

bonds between carbon atoms. Based on this concept, Tserpes and Papanikos [46] developed a three-dimensional finite element model to investigate the mechanical properties of armchair, zigzag and chiral single-walled CNTs. The results obtained by these authors are in good agreement with those provided by theoretical and experimental studies [25, 52, 53]. The computational effort of MSM is, however, still considerable for long nanotubes.

An alternative approach to atomistic simulations of CNTs relies on equivalent continuum formulations which are relatively simpler and result in a reduced computational effort. In modeling single-walled CNTs with a continuum mechanics model, the discrete atomic lattice of the nanotube is replaced by a continuous and homogeneous solid. In general, either isotropic and anisotropic shells [6, 53] or one-dimensional theories such as Euler-Bernoulli and Timoshenko beam models [34, 55] as well as rod models [54] are employed.

The use of classical continuum formulations at the nanoscale, however, might be questionable [8]. Classical theories do not account for small length scale effects induced by the discrete structure of single-walled CNTs. Promising approaches are those based on nonlocal continuum mechanics which allows the consideration of size effects by introducing small-scale parameters in the constitutive relation. The main advantage of a nonlocal formulation lies on the possibility of accounting for interatomic long range interactions (in Eringen's nonlocal theory [11], the strain at a given point is a weighted average of the strain at surrounding points). Applications of nonlocal continuum mechanics to the study of CNTs are reported in several papers [1, 44, 56].

Although several studies on the modeling of single-walled CNTs with nonlocal formulations have been carried out, only few attempts have been made to determine the value of the nonlocal parameters. Duan et al. [10] and Hu et al. [14] calibrated the small-scale parameters for the free vibration problem in single-walled CNTs by using molecular dynamics simulations. They found that the estimated nonlocal parameters vary with the aspect ratio, mode shapes and boundary conditions of the single-walled CNTs. A similar approach was used in [19] to capture size effects in the dynamic torsional response of (6,6) and (10,10) armchair single-walled CNTs with a nonlocal shell model. Naredar et al. [28], by using MSM, derived an expression of the small scale parameters to study the ultrasonic wave propagations in single-walled CNTs.

In this contribution, we estimate the nonlocal parameters for tensile armchair, zigzag and chiral single-walled CNTs by comparing the axial strain field calculated with MSM and a nonlocal elastic rod model. First, MSM is used to investigate size and chirality effects on single-walled CNTs Young's modulus and on the strain field in tensile simulations as discussed in Section 3.2.3 and 3.2.4, respectively. Then, a two-component local/nonlocal model [4, 12], a variant of the classical integro-differential Eringen's formulation, is considered for the modeling of single-walled CNTs as continuum rods. The corresponding one-dimensional constitutive equation is summarized in Section 3.3. Instead of the classical Gaussian kernel, the atomistically-based kernel developed by Picu [32] is adopted. As in atomic pair potentials [36], this kernel has a positive value at the origin and becomes negative at some distance. Finally, the identification of the nonlocal parameters is performed by means of an optimization procedure by minimizing the discrepancy between MSM and nonlocal axial strain fields as described in Section 3.4. To improve the agreement between atomistic and nonlocal results, the quadratic penalty method [29] is used. The effect of diameter and chirality on the value of the calculated parameters is further discussed. Hence, an

analytical relation between the nonlocal parameters and the nanotubes diameter and chirality is derived.

To our knowledge, the work in this chapter represents a first attempt to estimate nonlocal parameters for the modeling of single-walled CNTs subjected to static axial load by using an atomistic (MSM) model. The results presented herein ensure the reliability of nonlocal formulations to model tensile carbon nanotubes and, in particular, to predict their axial strain field and strain energy.

3.2 Molecular structural mechanic simulations of single-walled carbon nanotubes

3.2.1 Atomic model of single-walled carbon nanotubes

Molecular structural mechanics (MSM) is an atomistic modeling technique to study the mechanical properties of materials at the atomic scale. Similar to molecular mechanics (MM), molecules in MSM are modeled as discrete systems of balls (representing atoms) and springs (representing covalent and non-covalent bonds). Thus, knowing the position of the atoms and the stiffness of the chemical bonds that hold them together allows to predict the mechanical response of an atomic structure.

The constitutive equations for the structural elements depend on the mathematical relations describing the total potential energy Π of a molecule [21] which is expressed as:

$$\begin{aligned} \Pi = & \sum_{bonds} \Pi_{stretch}(\Delta r) + \sum_{angles} \Pi_{bend}(\Delta \omega) + \sum_{dihedrals} \Pi_{torsion}(\Delta \phi) \\ & + \sum_{pairs} \Pi_{nonbond}(\Delta r). \end{aligned} \quad (3.1)$$

Here, $\Pi_{stretch}$, Π_{bend} , $\Pi_{torsion}$ and $\Pi_{nonbond}$ are the energy contributions corresponding to bond stretching, angle bending, torsional motion around a single bond and stretching of non-covalent bonds (van der Waals forces), while Δr , $\Delta \omega$ and $\Delta \phi$ denote variations of covalent or non-covalent bonds length and angles between three atoms and dihedral angles (see Figure 3.1 for a representation of these quantities). As observed in Refs. [22, 38], the energy contribution from van der Waals interactions is negligible for covalent systems undergoing small deformations. Therefore, we neglect the contribution of $\Pi_{nonbond}$ in (3.1) since the small deformation hypothesis is adopted in this work.

Assuming the bond stretching and angle bending terms defined by the modified Morse potential [3] and the torsional contribution described by a parabolic function [18], the energy contributions in (3.1) are defined as:

$$\Pi_{stretch}(\Delta r) = D_e \left[\left(1 - e^{-\beta \Delta r} \right)^2 - 1 \right], \quad (3.2)$$

$$\Pi_{bend}(\Delta \omega) = \frac{k_\omega}{2} \Delta \omega^2 \left[1 + k_{sextic} \Delta \omega^4 \right], \text{ and} \quad (3.3)$$

$$\Pi_{torsion}(\Delta \phi) = \frac{k_\phi}{2} \Delta \phi^2. \quad (3.4)$$

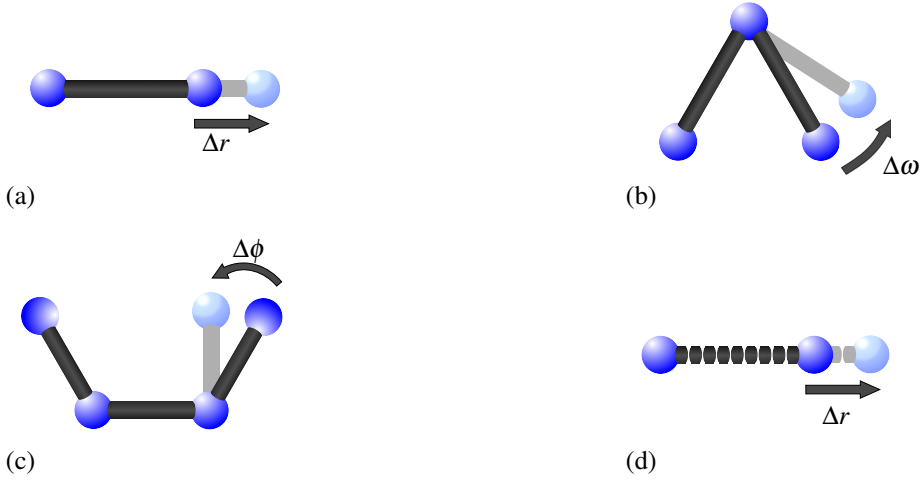


Figure 3.1: Interatomic interactions in molecular structural mechanics: (a) bonds stretching, (b) angle bending, (c) torsion and (d) stretching of non-covalent bonds.

According to Refs. [3, 18], the constant parameters D_e , β , k_ω , k_{sextic} and k_ϕ are equal to 0.603105 nN nm, 26.25 nm^{-1} , 0.9 nN nm/rad^2 , 0.754 rad^{-4} , and $0.278 \text{ nN nm/rad}^2$, respectively.

To study the mechanical properties of single-walled CNTs with MSM, we consider a frame finite element model geometry computed according to Ref. [20] with the constitutive equations of each structural element derived from (3.2)–(3.4). More specifically, the covalent bonds are defined as two-node space frame elements with the relation between axial force and axial stretch expressed as

$$F(\Delta r) = \frac{d\Pi_{stretch}(\Delta r)}{d\Delta r} = 2\beta D_e \left(1 - e^{-\beta\Delta r}\right) e^{-\beta\Delta r}. \quad (3.5)$$

Since the C–C bonds remain straight during deformation, we assume corresponding flexural and torsional stiffness values such that bending and torsional deformations are negligible when compared to the axial strains. Bending and torsional terms are modeled by means of torsional spring elements. Hence, according to (3.3) and (3.4), the constitutive equations between moments and angle variations are defined as

$$\begin{aligned} M_b(\Delta\omega) &= \frac{d\Pi_{angle}(\Delta\omega)}{d\Delta\omega} = k_\omega \Delta\omega \left(1 + 3k_{sextic} \Delta\omega^4\right) \quad \text{and} \\ M_t(\Delta\phi) &= \frac{d\Pi_{torsion}(\Delta\phi)}{d\Delta\phi} = k_\phi \Delta\phi. \end{aligned} \quad (3.6)$$

3.2.2 Model geometry

The geometry of the model in the MSM simulations is built with reference to the atomic structure of the nanotubes. Single-walled CNTs are periodic cylindrical cage-like structures

of carbon atoms with high aspect ratio and diameter in the nanoscale range. The cylindrical shape consists of a mono layer graphene sheet. Geometric and mechanical properties of single-walled CNTs depends on the rolling angle, that is the orientation of the carbon lattice with respect to the longitudinal axis of the nanotube.

The geometric properties of a single-walled carbon nanotube are usually expressed in terms of diameter d , chiral angle θ , and length L . With reference to Figure 3.2(a), and denoting the distance of the carbon-carbon bonds with a_{cc} (here assumed equal to 0.1421 nm), diameter and chirality are uniquely defined by the chiral vector

$$\mathbf{C}_h = n_1 \mathbf{a}_1 + n_2 \mathbf{a}_2 \quad (3.7)$$

in which n_1 and n_2 are a couple of integers, and \mathbf{a}_1 and \mathbf{a}_2 the basis vectors

$$\mathbf{a}_1 = \left(\frac{\sqrt{3}}{2}, \frac{1}{2} \right) \sqrt{3} a_{cc} \quad \text{and} \quad \mathbf{a}_2 = \left(\frac{\sqrt{3}}{2}, -\frac{1}{2} \right) \sqrt{3} a_{cc}. \quad (3.8)$$

The length of \mathbf{C}_h specifies the circumference C of the nanotube. Therefore, the diameter of a single-walled CNT can be calculated as

$$d = \frac{C}{\pi} = \frac{a_{cc} \sqrt{3(n_2^2 + n_1^2 + n_1 n_2)}}{\pi}. \quad (3.9)$$

The angle between \mathbf{C}_h and the basis vector \mathbf{a}_1 denotes the chiral angle

$$\theta = \arctan \left(\frac{\sqrt{3} n_2}{2n_1 + n_2} \right). \quad (3.10)$$

Carbon nanotubes are named after the value assumed by the chiral angle θ . If $\theta = 0$, $n_2 = 0$ in (n_1, n_2) and the single-walled CNT is called *zigzag*. On the other hand, the single-walled CNT is called *armchair* when $\theta = \pi/6$ and n_1 is equal to n_2 . For any other value in the range $(0; \pi/6]$, the nanotube is referred to as *chiral*.

Moreover, the chiral vector \mathbf{C}_h can be used to identify the periodic unit cells of the carbon nanotubes. Indeed, as indicated in Figure 3.2(b)–(c), a single-walled CNT is periodic along both the longitudinal and the circumferential directions. In particular, the width of the periodic unit cell along the nanotube axis is

$$T = |\mathbf{T}| = \frac{\sqrt{3} |\mathbf{C}_h|}{\text{gcd}(2n_1 + n_2, 2n_2 + n_1)}, \quad (3.11)$$

where $|\mathbf{T}|$ denotes the magnitude of the translational vector \mathbf{T} (see Figure 3.2(a)) and $\text{gcd}(a, b)$ the greatest common divisor (gcd) of two integers a and b . Similarly, the width of the periodic cell along the circumference is

$$S = \frac{|\mathbf{C}_h|}{\text{gcd}(n_1, n_2)}. \quad (3.12)$$

As shown in Figure 3.2, the widths T and S vary according to the chirality of the nanotube while they are not affected by its diameter and length.

For more details on the periodicity and symmetry of single-walled CNT structure we refer the reader to Ref. [37].

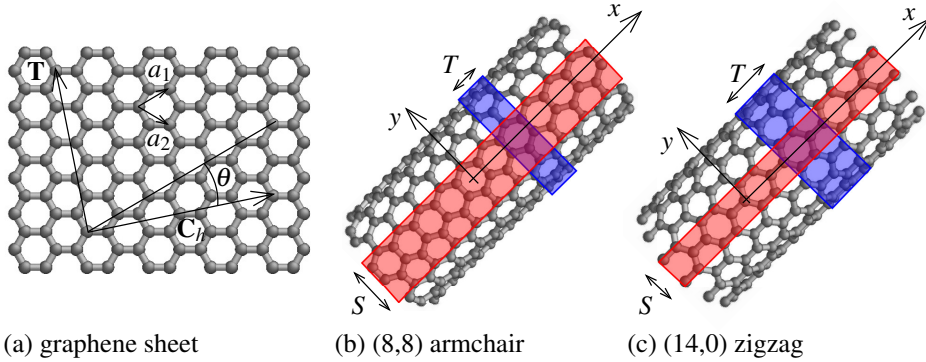


Figure 3.2: (a) Honeycomb structure of graphene and atomic configuration of (b) an (8,8) armchair and (c) a (14,0) zigzag single-walled CNT. Blue and red areas denote the portions of single-walled CNT which are repeated periodically along the longitudinal axis and the circumference, respectively.

3.2.3 Young's modulus

By assuming the carbon nanotubes as continuum hollow cylinders, a set of single-walled CNTs with different diameter and chirality has been employed to derive the Young's modulus E_{xx} for the one-dimensional formulation in Section 3.3. One end of the nanotube was fully constrained whereas an axial displacement \bar{u}_x was applied to the opposite side where radial displacements are also constrained. The value of \bar{u}_x was set equal to 10^{-5} nm in order to calculate the tangent elastic modulus of the nanotubes and to satisfy the small deformation hypothesis. We stress that the nonlinear constitutive laws of the structural elements in the MSM model, which are representative of the covalent bonds, do not account for plasticity and damage.

Figure 3.4 shows the deformed configurations of a tensile single-walled CNT. The value of the stiffness was determined through

$$E_{xx} = F_x L / A \bar{u}_x, \quad (3.13)$$

where F_x is the reaction force along the longitudinal direction at the fully constrained end, and A is the cross sectional area of the single-walled CNT. This quantity is defined as the area of an annulus with thickness $t = 0.34$ nm [16] and inner diameter $d - t/2$. The results, shown in Figure 3.3 and in Tables 3.1 and 3.2, reveal a dependence on diameter and chirality. Indeed, E_{xx} increases with the diameter and reaches an almost constant value for d larger than 2 nm. The two sets of chiral single-walled CNTs yield the highest values of E_{xx} , whereas zigzag nanotubes have the lowest axial stiffness.

These results are in good agreement with experimental and numerical tests in the literature. Demczyk et al. [9] estimated a Young's modulus equal to 900 GPa from pulling individual carbon nanotubes with diameter of about 10 nm away from one fixed end in a transition electron microscope. Values of E_{xx} ranging between 940 and 1118 GPa have been found with *ab initio* calculations in Ref. [23]. Based on molecular dynamics simulations,

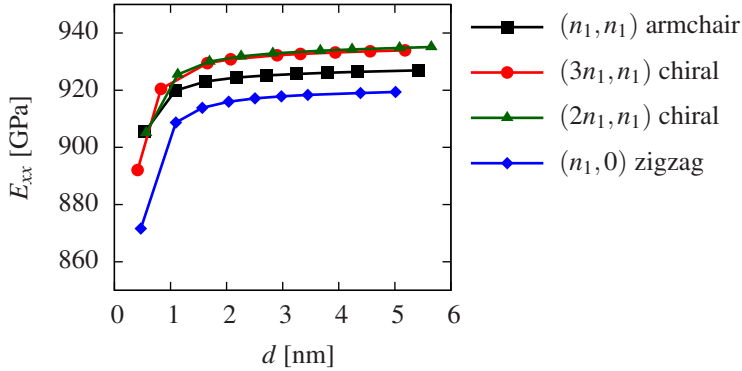


Figure 3.3: Young's modulus of single-walled CNTs as a function of diameter and chirality.

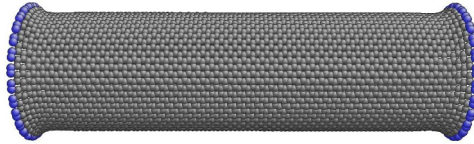


Figure 3.4: Deformed configuration of a (28, 28) armchair single-walled CNT with length 12.31 nm under tensile loading (blue atoms have constrained radial displacements).

WenXing et al. [49] showed that the Young's modulus ranges between 918 and 941 GPa for single-walled CNTs with different chirality and diameters ranging between 1.6 and 2.8 nm. Belytschko et al. [3] calculated a value of E_{xx} equal to 940 GPa for a (20, 0) nanotube with the modified Morse potential in molecular mechanics calculations. Meo and Rossi [27], by employing an MSM approach similar to that presented in this chapter to single-walled CNTs with diameter ranging between 0.4 and 2 nm, showed that the Young's modulus varies from 910 to 923 GPa for the armchair configuration and from 899 and 920 GPa for the zigzag configuration. Furthermore, similar effects of chirality on the elastic modulus have been observed in Refs. [7, 45, 46, 51].

3.2.4 Strain field in single-walled CNTs under tensile load

To investigate the axial strain in tensile single-walled CNTs, we adopt the technique developed by Shimizu et al. [43] who calculate the strain field from atomistic simulations. The idea behind this method is that strains are calculated through a least-squares fit of the deformation gradient \mathbf{J}_i for each atom i . Accordingly, \mathbf{J}_i is computed as the tensor which best maps \mathbf{d}_{ij} to \mathbf{d}_{ij}^0 , where \mathbf{d}_{ij} and \mathbf{d}_{ij}^0 are the distances between atom i and its neighbor j in the current and reference configuration, respectively. Therefore, minimization of

$$\sum_{i \in N_i} |\mathbf{J}_i \mathbf{d}_{ij}^0 - \mathbf{d}_{ij}|^2,$$

(n_1, n_1)	d [nm]	E_{xx} [GPa]	$(n_1, 0)$	d [nm]	E_{xx} [GPa]
(4, 4)	0.54	905.4	(6, 0)	0.47	871.6
(8, 8)	1.09	919.9	(14, 0)	1.10	908.7
(12, 12)	1.63	923.1	(20, 0)	1.57	913.8
(16, 16)	2.17	924.4	(26, 0)	2.04	915.1
(20, 20)	2.71	925.2	(32, 0)	2.51	917.1
(24, 24)	3.26	925.7	(38, 0)	2.98	917.9
(28, 28)	3.80	926.1	(44, 0)	3.45	918.4
(32, 32)	4.34	926.4	(56, 0)	4.39	919.0
(40, 40)	5.43	926.9	(64, 0)	5.01	919.4

(a) (n_1, n_1) armchair (b) $(n_1, 0)$ zigzag

Table 3.1: Young's modulus of (a) armchair and (b) zigzag single-walled CNTs with a length of 12.31 and 12.36 nm, respectively.

$(2n_1, n_1)$	d [nm]	E_{xx} [GPa]	$(3n_1, n_1)$	d [nm]	E_{xx} [GPa]
(4, 2)	0.41	892.1	(6, 2)	0.56	905.1
(8, 4)	0.83	920.5	(12, 4)	1.13	925.5
(16, 8)	1.66	929.5	(18, 6)	1.69	930.0
(20, 10)	2.07	930.8	(24, 8)	2.26	931.9
(28, 14)	2.90	932.2	(30, 10)	2.82	932.9
(32, 16)	3.32	932.7	(39, 13)	3.67	933.8
(38, 19)	3.94	933.2	(45, 15)	4.24	934.3
(44, 22)	4.56	933.6	(54, 18)	5.08	934.8
(50, 25)	5.18	933.7	(60, 20)	5.65	935.1

(a) $(2n_1, n_1)$ chiral (b) $(3n_1, n_1)$ chiral

Table 3.2: Young's modulus for (a) $(2n_1, n_1)$ and (b) $(3n_1, n_1)$ chiral single-walled CNTs with a length of 12.41 and 12.30 nm, respectively.

yields the deformation gradient

$$\mathbf{J}_i = \left(\sum_{i \in N_i} \mathbf{d}_{ij}^{0T} \mathbf{d}_{ij}^0 \right)^{-1} \left(\sum_{i \in N_i} \mathbf{d}_{ij}^{0T} \mathbf{d}_{ij} \right), \quad (3.14)$$

in which N_i denotes the number of neighbors of atom i . The value of N_i depends on the cutoff radius r_{co} since it specifies the region of the nanotube to be considered in the calculation. Here, we assume r_{co} equal to the magnitude of the Burgers vector in carbon nanotubes [15], namely $\sqrt{3}a_{cc}$. Therefore, with \mathbf{I} denoting the identity tensor, the Lagrangian strain tensor at atom i is defined as [43]

$$\mathbf{E}_i = \frac{1}{2} (\mathbf{J}_i \mathbf{J}_i^T - \mathbf{I}). \quad (3.15)$$

Next, we will examine the influence of chirality on the axial component ε_{xx} of the strain field derived from (3.15) and the circumferential strain field ε_r calculated as the ratio between the

radial displacement u_r and the nanotube radius. Here and throughout the chapter, ε_{xx} and ε_r are normalized with respect to the local axial strain $\bar{\varepsilon}_{xx} = \bar{u}_x/L$ and the circumferential strain at the middle section $\varepsilon_{r,x/L=0.5}$, respectively.

To investigate the effect of the chirality, the strain field is represented on the unrolled nanotube. The normalized strain field values at atoms aligned along the longitudinal direction are interpolated by piecewise curves as depicted in Figure 3.5 where ε_{xx} and ε_r are shown for three tensile nanotubes with different chirality but similar diameter and length. Furthermore, all nanotubes show a boundary layer. In armchair and zigzag nanotubes, both axial and circumferential strain fields are represented by two different curves with similar trend which repeat periodically along the circumference. Chiral nanotubes, on the other hand, present a higher number of periodic curves and a more complex profile of the strain field due to the rotation of the symmetry axis. Chirality-induced anisotropy in chiral single-walled CNTs has been discussed in many works [5, 31, 50]. However, only few studies aimed at modeling chiral nanotubes as anisotropic shells [2, 6, 40] instead of using the more common isotropic models [13, 30, 39, 42, 47, 48, 53]. Unfortunately, none of these works has included a comparison of the strain field obtained with atomistic simulations and shell models. Moreover, it is likely that continuum models cannot reproduce the complex profile of the strain field reported in Figures 3.5(e) and 3.5(f) which is a consequence of the discrete structure of the nanotube.

With regard to the diameter, we compare the strain field in nanotubes with equal chirality and length but different diameter. Figure 3.6(a)-(b) shows that height and width of the boundary layer increase with the diameter d in both armchair and zigzag single-walled CNTs. A similar dependence of ε_{xx} on the diameter, as shown in Figure 3.6(c)-(d), is observed in chiral nanotubes. With regard to the radial strain, Figure 3.7 shows that the width of the boundary layer increases with the nanotube diameter, whereas its height barely changes.

Finally, the dependence of the strain profile on the nanotube length has been examined. We observed that the effect of L on both ε_{xx} and ε_r is negligible (refer to the discussion in Section 3.4).

The MSM results presented in this section have been verified with those obtained from MM simulations performed with the LAMMPS software [33] (input files and supplemental material are freely available for download at the authors' web page).

3.3 Nonlocal integro-differential elastic model for one-dimensional problems

According to the nonlocal theory of elasticity developed by Eringen [11], the strain at a point is calculated as a weighted integral of the strain field at surrounding points. By accounting for small-scale effects, nonlocal theories have been used to model nanostructures such as carbon nanotubes [1, 56]. Hence, with the aim of modeling tensile single-walled CNTs as one-dimensional rods with mechanical properties that can be related to those of single-walled CNTs, the local/nonlocal constitutive law

$$\sigma_{xx}(x) = E_{xx} \left(\xi_1 \varepsilon_{xx}(x) + \xi_2 \int_0^L g(x, \bar{x}, \ell) \varepsilon_{xx}(\bar{x}) d\bar{x} \right) \quad (3.16)$$

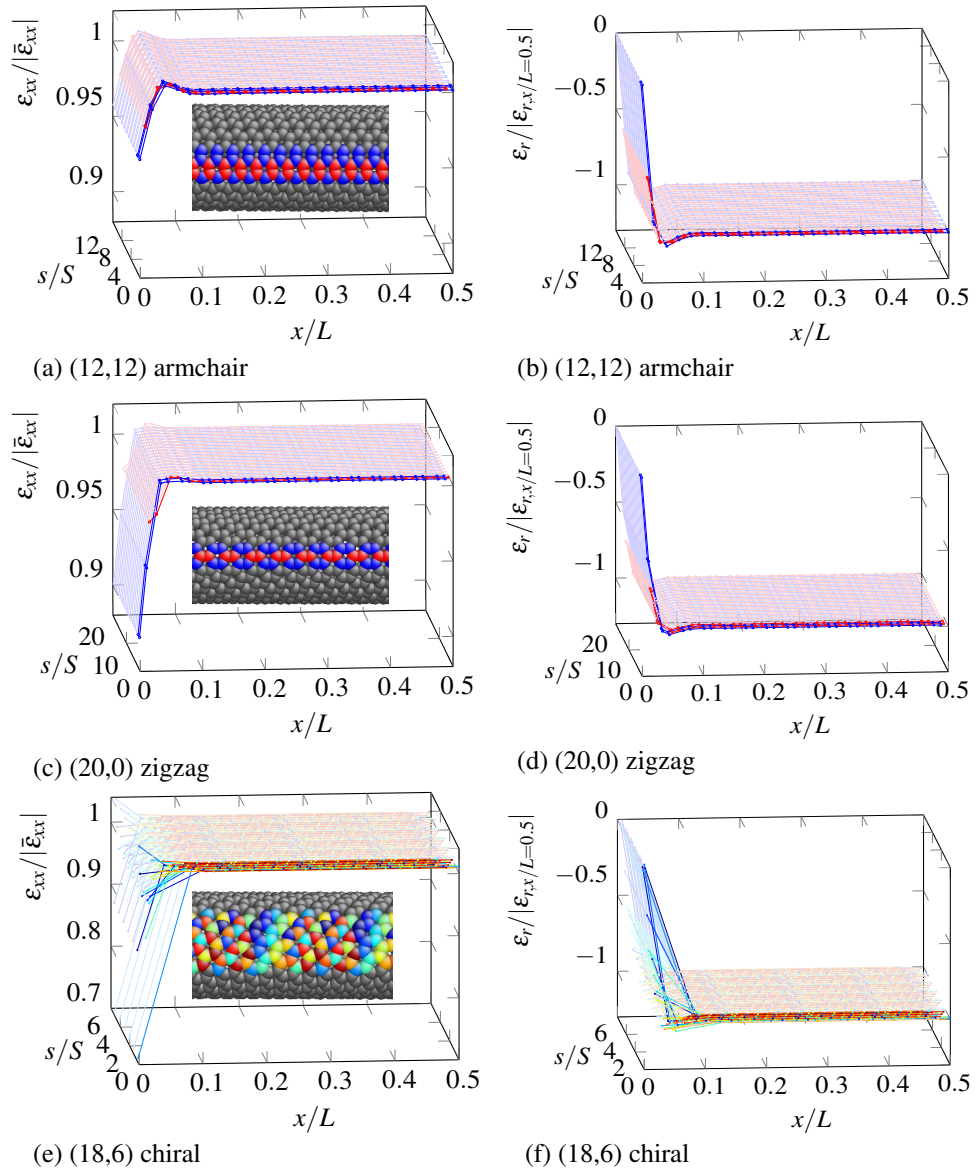


Figure 3.5: Normalized axial and hoop strain fields in (a)-(b) (12,12) armchair, (c)-(d) (20,0) zigzag and (e)-(f) (18,6) chiral single-walled CNTs. The strain field is represented over the unrolled single-walled CNTs surface. Only half of the axial domain is shown due to symmetry, whereas the entire curvilinear abscissa s , related to the circumference of the nanotubes, is considered. The atoms aligned along the x direction are connected with a piecewise linear interpolation. Lines whose atoms are aligned along the s direction have the same color. For illustration purposes, only the lines in the first periodic longitudinal strip of width S have been highlighted (make reference to Figure 3.2 for the definition of S). The insets provide a visual representation of the SWNTCs atomic structure and of the highlighted lines of atoms: five in the armchair configuration, three in the zigzag configuration and 26 in the chiral configuration.

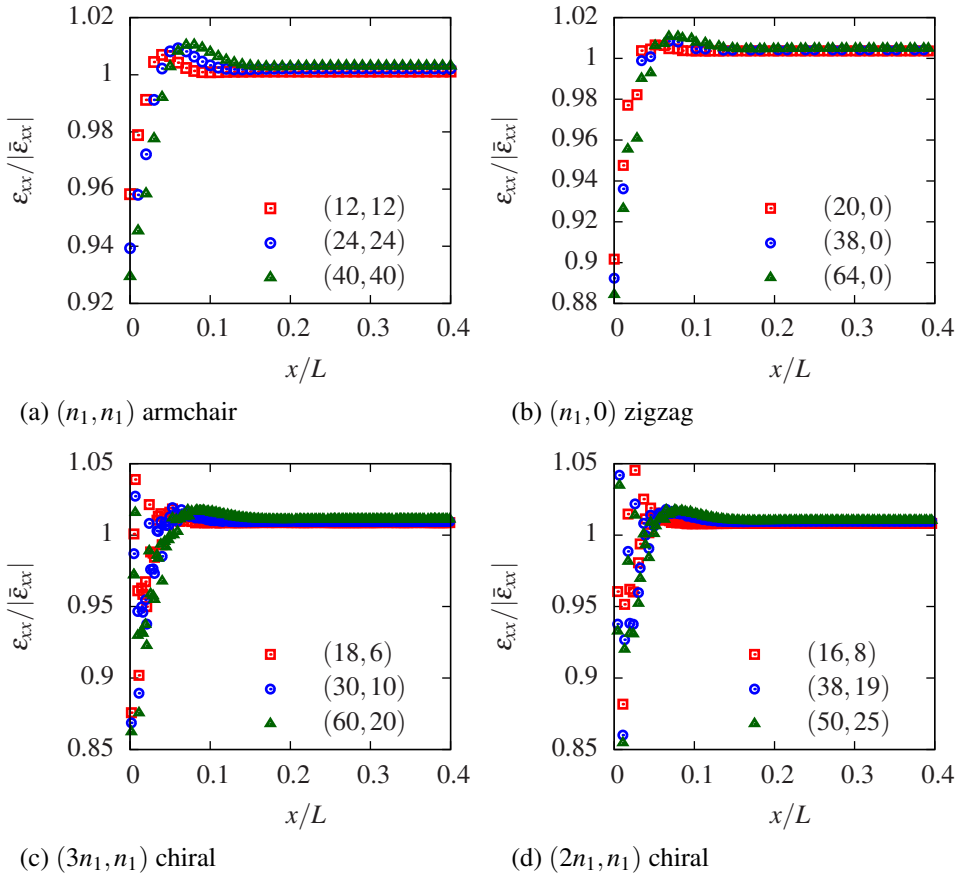


Figure 3.6: Normalized axial strain field for (a) armchair, (b) zigzag, (c) $(3n_1, n_1)$ chiral and (d) $(2n_1, n_1)$ chiral single-walled CNTs.

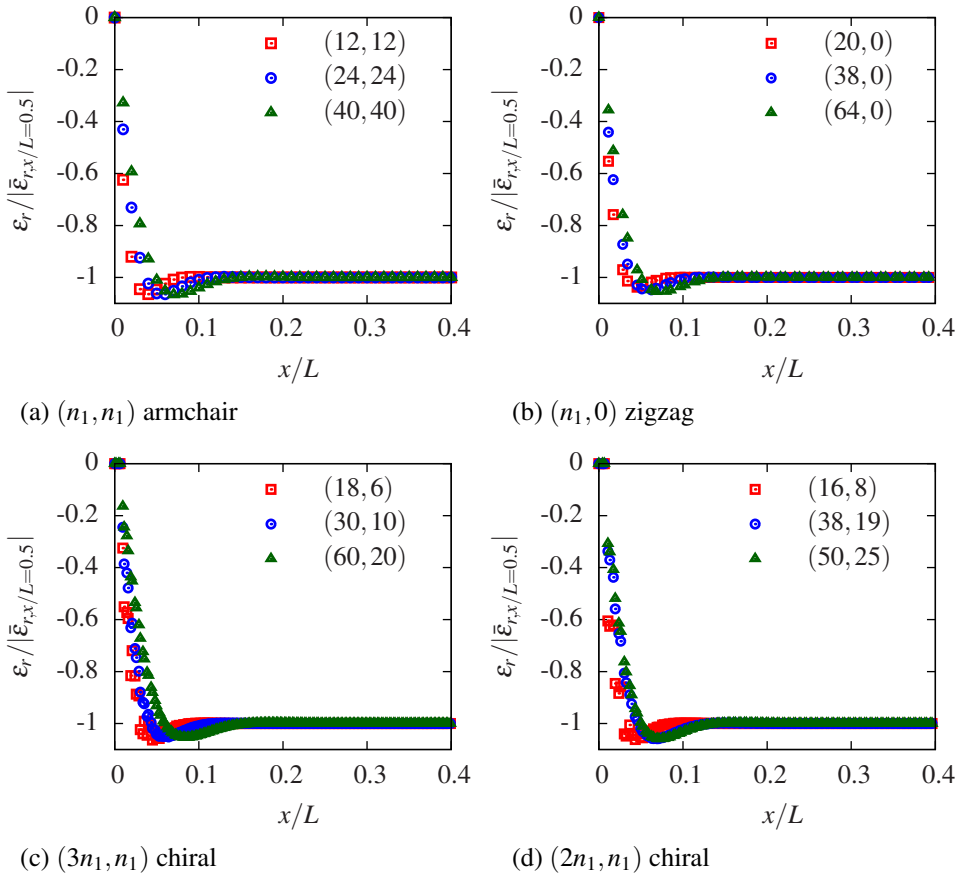


Figure 3.7: Normalized hoop strain field for (a) armchair, (b) zigzag, (c) $(3n_1, n_1)$ chiral and (d) $(2n_1, n_1)$ chiral single-walled CNTs.

proposed in Ref. [12] is adopted in this work. Parameters ξ_1 and ξ_2 are such that $\xi_1 + \xi_2 = 1$ (see [4]), and the nonlocal kernel $g(x, \bar{x}, \ell)$ is a weighting function which depends on the distance $|x - \bar{x}|$ and the intrinsic length scale ℓ of the nanotubes (which is related to its geometry).

The choice of a nonlocal kernel capable of representing long-range atomic interactions is crucial for the accurate prediction of deformation phenomena at the nanoscale. In the literature, Gaussian and exponential weight functions have been widely used [12]. With these kernels, however, the nonlocal model used in this study was not able to accurately reproduce the axial strain field obtained with MSM. Fortunately, this was possible with the atomistically-based nonlocal kernel

$$g(x, \bar{x}, mb) = \alpha_0 \left(1 - n(|x - \bar{x}|/b)^2\right) \exp\left[-(|x - \bar{x}|/mb)^2\right] \quad (3.17)$$

proposed by Picu [32], where the intrinsic length scale ℓ is defined as the product of the nonlocal parameter m and the magnitude b of the Burgers vector \mathbf{b} . A second dimensionless nonlocal parameter, n , and the normalization factor α_0 complete the set of parameters. In the one-dimensional case, the condition

$$\int_{-\infty}^{\infty} g(x, \bar{x}, \ell) d\bar{x} = 1 \quad (3.18)$$

yields

$$\alpha_0 = [\sqrt{\pi}mb(1 - 0.5nm^2)]^{-1}. \quad (3.19)$$

3.3.1 Numerical solution

To understand the physical implications of the nonlocal parameters in (3.17), we make use of a representative one-dimensional problem. We consider an elastic rod with length L , cross sectional area A and Young's modulus E_{xx} equal to 20 nm, 1 nm² and 900 GPa, respectively. An axial displacement $\bar{u} = 1$ nm is applied at $x = L$ while the opposite end at $x = 0$ mm is fixed. This boundary value problem has been solved numerically since the analytical solution is not available. As shown in Ref. [26], higher order B-spline basis functions are superior to classical Lagrange and Hermite basis functions and C^∞ generalized finite element approximations in modeling nonlocal integro-differential problems. In general, B-spline basis functions avoid the presence of periodic oscillations which, on the contrary, characterize the strain field approximated with the other techniques. Therefore, in this work, quintic B-spline basis functions have been employed for the computation of ϵ_{xx} . The one-dimensional model has been discretized using 107 equally-spaced elements (usually referred to as uniform knot spans in the isogeometric analysis context [17]) which correspond to 100 degrees of freedom. The MATLAB[®] scripts are freely available for download at the authors' web page as supplementary material.

As indicated in Figure 3.8(a), the discrepancy between nonlocal and local solution (which corresponds to $\xi_1 = 1$) increases with $|1 - \xi_1|$. For $\xi_1 > 1$ the value of ϵ_{xx} at the boundaries is smaller than the local strain $\bar{\epsilon}_{xx}$, whereas $\xi_1 < 1$ produces the opposite behavior. Figure 3.8(b) shows that the boundary layer becomes sharper by decreasing m as a consequence of the smaller intrinsic length scale ℓ . These results are similar to those derived by Benvenuti

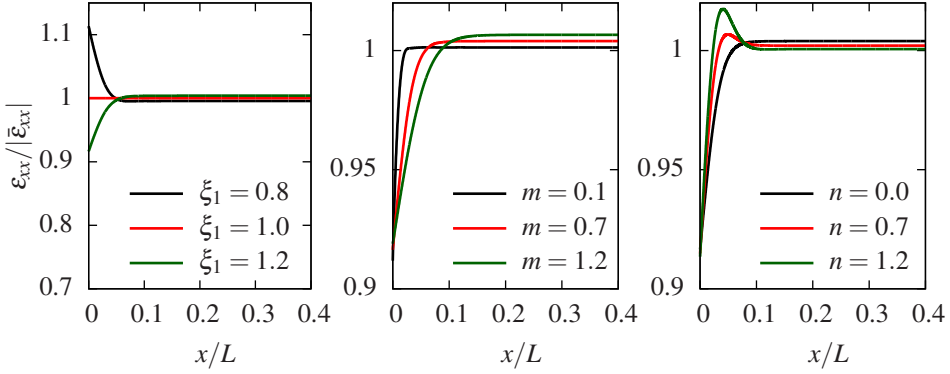


Figure 3.8: Normalized strain field for a one-dimensional nonlocal tensile rod by fixing (a) $m = 0.7$ and $n = 0$, (b) $\xi_1 = 1.2$ and $n = 0$, (c) $\xi_1 = 1.2$ and $m = 0.7$, and by varying ξ_1 , m and n , respectively.

and Simone [4] with of an exponential kernel. Nonetheless, the presence of the second nonlocal parameter n leads to an interesting consequence. Indeed, as illustrated in Figure 3.8(c), n increases the maximum value of the strain toward the boundary layers. Consequently, the profile of ε_{xx} obtained from the one-dimensional nonlocal model recalls the results calculated with molecular structural mechanics.

Hence, it might be interesting to provide a reliable estimate of the nonlocal parameters ξ_1 , m and n in order to approximate the axial strain field of tensile single-walled CNTs with the nonlocal model (3.16) equipped with the atomistically-based kernel (3.17). To achieve this goal, we will make use of a parameter estimation procedure. This procedure is feasible for the axial strain field in armchair and zigzag nanotubes due to the similarity of the strain profiles in the periodic strip. As shown in Figure 3.6(c)-(d), a similar argument does not hold for the response of chiral single-walled CNTs. Therefore, in the parameter estimation procedure described in the next section we will derive ξ_1 , m and n only for armchair and zigzag nanotubes.

3.4 Estimation of the nonlocal parameters

Based on the collection of results provided by the atomistic simulations described in Section 3.2, we wish to determine the value of the parameters m , n and ξ_1 for each single-walled CNT such that the nonlocal model can accurately represents the axial strain field calculated with MSM. This operation is performed by means of a parameter estimation procedure. Given the parameter vector $p = [\xi_1, m, n]$, we aim to solve the least-square problem

$$\min_p f(p), \quad (3.20)$$

where the objective function

$$f(p) = \frac{1}{2} \sum_{i=1}^N \left(\frac{\varepsilon_{xx_i}^{NL}(p) - \varepsilon_{xx_i}^{MSM}}{\bar{\varepsilon}} \right)^2 \quad (3.21)$$

measures the discrepancy between nonlocal and MSM results at the N points corresponding to the atoms of the single-walled CNT. To improve the quality of the fit for the boundary layers in ε_{xx} , we consider problem (5.16) subject to the inequality constraints

$$\begin{aligned} c(p) &= \frac{|\varepsilon^{NL}(x_m, p) - \varepsilon^{MSM}(x_m)|}{\varepsilon^{MSM}(x_m)} \leq \tau \quad \text{and} \\ C(p) &= \frac{|\varepsilon^{NL}(x_M, p) - \varepsilon^{MSM}(x_M)|}{\varepsilon^{MSM}(x_M)} \leq \tau \end{aligned} \quad (3.22)$$

where x_m and x_M denote the minimum and maximum values of the atomic strain field, and the tolerance τ is assumed equal to 10^{-6} .

Constrained parameter estimation problems can be solved with different numerical techniques [29]. For our purposes, we used the quadratic penalty method. This simple technique combines objective function (3.21) and constraints (3.22) into the unconstrained optimization problem

$$\min_p \left\{ Q(p, \mu) = f(p) + \frac{\mu}{2} \sum (c^2(p) + C^2(p)) \right\}, \quad (3.23)$$

in which the penalty parameter μ penalizes constraint violations—that is, the higher the value of μ the closer to zero the constraints in (3.22). The quadratic penalty method may lead to ill conditioning and unfeasible solutions. Nonetheless, as suggested in Ref. [29], it is possible to avoid these issues by choosing a suitable sequence of positive values $\{\mu_k\}$ with $\mu_k \rightarrow \infty$ as $k \rightarrow \infty$ and to calculate the approximate minimizer p_k of $Q(p, \mu_k)$ for each k .

Hence, for each nanotube a reasonable starting point p_0 of the identification process was carried out with a preliminary visual examination and the initial penalty parameter μ_0 was assumed equal to 1. The set of parameters $\{\mu_k\}$ has been chosen such that $\mu_k = 10\mu_{k-1}$. At each k -th step an approximate minimizer p_k of $Q(p, \mu_k)$ was derived by starting from $p = p_{k-1}$ and terminating either when the objective function $Q(p, \mu_k)$ was less than 10^{-4} or the infinity norm of the gradient $\nabla_p Q(p, \mu_k)$ was less than 10^{-6} . By satisfying these requirements, the minimizer of $Q(p, \mu_k)$ was reached. In particular, the Gauss-Newton method was used to minimize the objective function in (3.23) avoiding the trouble of computing the Hessian of $Q(p, \mu_k)$ [29]. In general, it was observed that a small number of iterations was needed to attain the converged solution as reported in Figure 3.9. This iterative procedure was repeated until the feasibility conditions (3.22) were satisfied.

To investigate the influence of the nanotube length on the nonlocal parameters, we have considered several values of L . First, ξ_1 , m and n have been estimated for armchair and zigzag nanotubes with a length of 12.31 and 12.36 nm, respectively. Quintic B-spline basis functions, 400 degrees of freedom and uniform knot spans have been used while computing ε_{xx}^{NL} . Then, we have considered SWNCTs whose length was two, four and eight times longer than the previous ones. Accordingly, the nonlocal strain field has been calculated by increasing the number of degrees of freedom involved in the analysis two, four and eight times (i.e. by keeping the size of the knots spans constant).

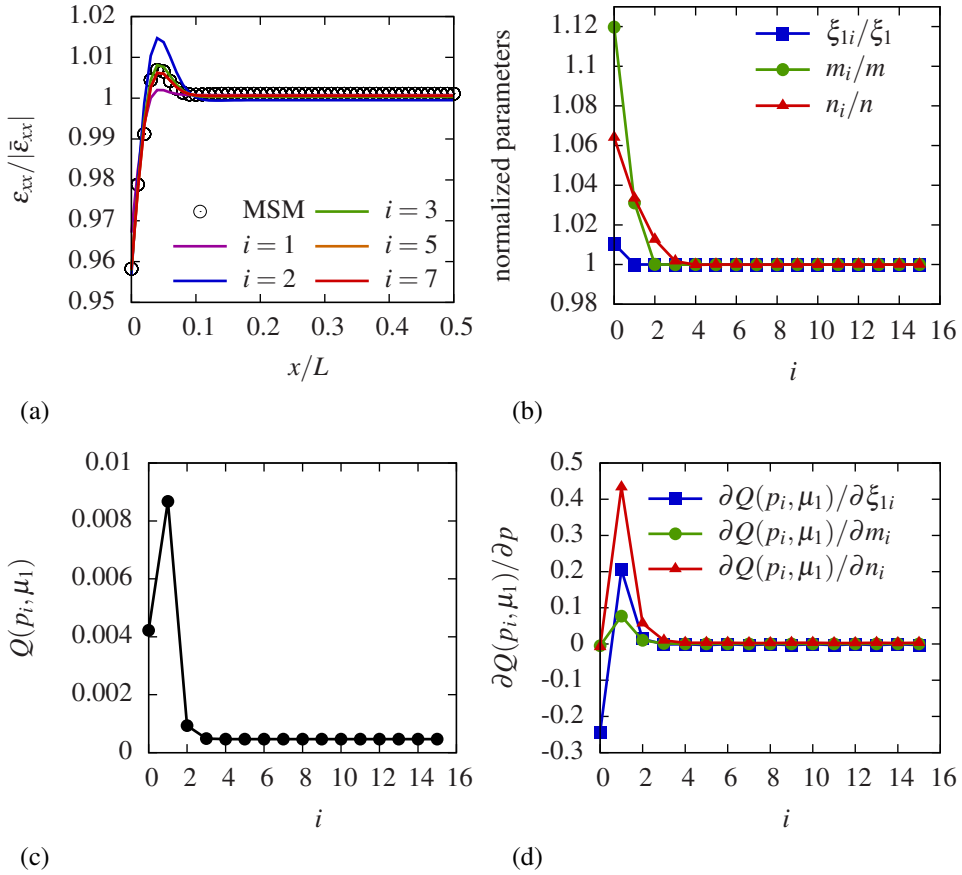


Figure 3.9: Convergence pattern of the initial k -th step (i.e. $\mu_k = \mu_1$) for the (12, 12) armchair single-walled CNT: (a) normalized nonlocal axial strain field approximating the MSM results (only few iteration steps are displayed), (b) normalized values of the nonlocal parameters ξ_1 , m and n , (c) the cost function and (d) its derivatives with respect to p (i refers to the iteration number).

Figure 3.10 illustrates the calculated nonlocal parameters corresponding to armchair and zigzag nanotubes with different diameters and lengths. As mentioned in Section 3.2.4, the diameter has a marked effect in the characterization of the strain field of single-walled CNTs whereas length effects are negligible. Furthermore, we can easily notice a clear trend in the value of ξ_1 , m and n . Therefore, seeking for an analytical relation between the nonlocal parameters and the nanotubes geometric characteristics we have considered the function

$$q(d, \theta) = c_1(\theta) + c_2(\theta) d^{c_3(\theta)} \quad (3.24)$$

where q is a generic nonlocal parameter, equal to m , n or ξ_1 . The dimensionless parameters c_1 , c_2 and c_3 have been determined for both armchair and zigzag nanotubes with the *fit* function from the MATLAB[®] Optimization Toolbox. In particular, the Trust-Region algorithm with randomly generated starting points has been chosen. The estimated set of parameters is listed in Table 3.3 and the corresponding functions are depicted in Figure 3.10.

	ξ_1	m	n		ξ_1	m	n
c_1	1.48	-2.96	0.05	c_1	1.12	0.26	0.70
c_2	-0.16	4.43	0.43	c_2	0.11	1.17	-0.49
c_3	-0.22	0.22	-1.83	c_3	0.31	0.42	0.14
RMSE	4.0e-7	5.1e-6	8.8e-5	RMSE	3.4e-6	1.4e-4	4.7e-5
R^2	0.9995	0.9989	0.9980	R^2	0.9864	0.9490	0.9922

(a) (n_1, n_1) armchair

(b) $(n_1, 0)$ zigzag

Table 3.3: Parameter c_1 , c_2 and c_3 for (a) armchair and (b) zigzag nanotubes with diameter ranging between 1 and 5.5 nm. The goodness of fit has been assessed by calculating the root mean square error (RMSE) and the coefficient of determination (R^2).

To conclude, we have assessed the effectiveness of the proposed model. As illustrated in Figure 3.11, the one-dimensional nonlocal model (3.16), with ξ_1 , m and n derived from (3.24), yields a good approximation of the axial strain field in tensile single-walled CNTs. However, despite an accurate approximation of the boundary layers, a small discrepancy between discrete and continuum profiles occurs in the central part of the domain as shown in the insets in Figure 3.11. Nonetheless, it was observed that such discrepancy decreases by increasing the length of the nanotubes. Furthermore, we have compared the total strain energy computed with MSM (Π^{MSM}) and the nonlocal theory (Π^{NL}). As reported in Figure 3.12, the relative error is small. This discrepancy does not lie only in the approximation provided by the nonlocal formulation. Indeed, it can also be attributed to the deformation components involved in the calculation of the strain energy. For the nonlocal one-dimensional model, Π^{NL} is determined solely by the axial deformations. In contrast, for the atomistic simulation, Π^{MSM} is expressed as a summation of different terms (see eq. (3.1)) from which it is not possible to derive the components specifically related to axial deformations.

3.5 Conclusions

We have estimated the parameters required to model tensile single-walled CNTs as nonlocal rods. With these parameters it was possible to correctly capture size and chirality effects

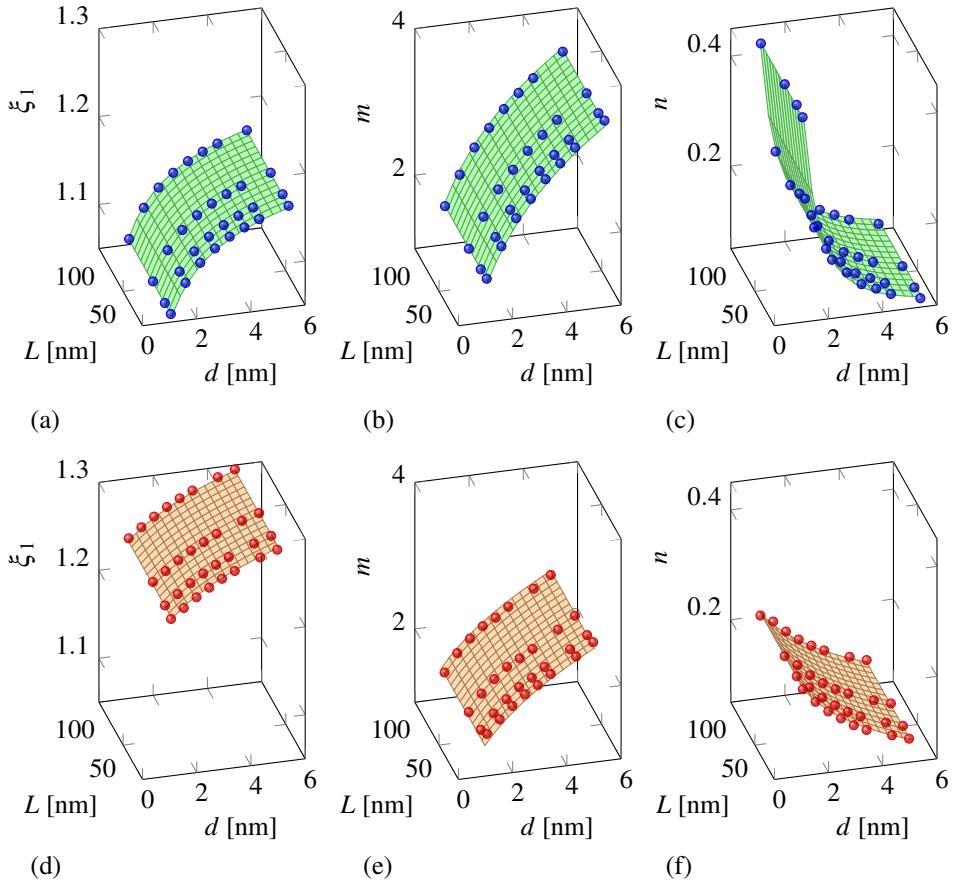


Figure 3.10: Nonlocal parameters ξ_1 , m and n for (a)-(c) (n_1, n_1) armchair and (d)-(f) zigzag single-walled CNTs calculated with the parameter estimation procedure (filled markers) and corresponding approximating surface.

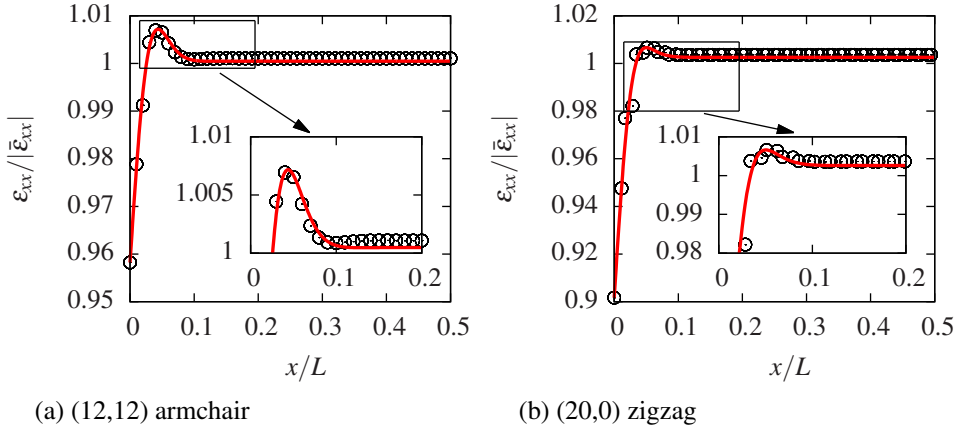


Figure 3.11: Normalized axial strain field ϵ_{xx} calculated with MSM simulations (circles) and the one-dimensional nonlocal model (solid red line) for (a) a (12,12) armchair and (b) a (20,0) zigzag single-walled CNTs with length L equal to 12.31 and 12.05 nm, respectively.

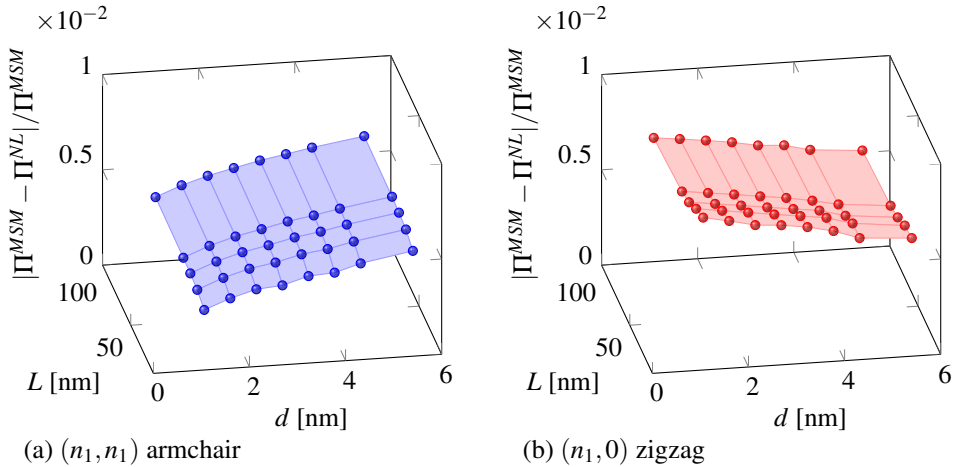


Figure 3.12: Relative error between the total strain energies computed with MSM (Π^{MSM}) and the one-dimensional nonlocal model (Π^{NL}) for (a) armchair and (b) zigzag single-walled CNTs.

observed in the axial strain profile computed with molecular structural mechanics. In particular, the optimal nonlocal parameters resulted to vary with the diameter and the chirality of the nanotubes while the influence of the length was negligible. Nonlocal parameters have been estimated for armchair and zigzag single-walled CNTs only. As the orthotropy axes in chiral single-walled CNTs are not aligned with the chiral and roll-up axes, one-dimensional theories are not suitable.

The choice of the nonlocal kernel was the key to the characterization of the equivalent nonlocal rod model. By adopting an atomistically-based nonlocal kernel, the axial strain profiles obtained with the integro-differential formulation were remarkably consistent with those predicted with molecular structural mechanics. Classical Gaussian and exponential kernels did not produce similar results.

The successful use of nonlocal models as a replacement for more sophisticated atomistic models hinges on the reliable determination of the nonlocal parameters and the choice of the constitutive relation. To our knowledge, this is the first time nonlocal parameters have been derived from the axial strain field obtained from atomistic simulations of single-walled CNTs. The adopted approach, although partially successful because applicable to “smooth” axial strain profiles only, paves the way for the use of nonlocal formulations in studies of CNTs and CNTs-based composites and all those applications in which axial deformation is the predominant CNT deformation mode.

Bibliography

- [1] B. Arash and Q. Wang. A review on the application of nonlocal elastic models in modeling of carbon nanotubes and graphenes. *Computational Materials Science*, 65: 303–313, 2012.
- [2] C. Bajaj, A. Favata, and P. Podio-Guidugli. On a nanoscopically-informed shell theory of single-wall carbon nanotubes. *European Journal of Mechanics A/Solids*, 42:137–157, 2013.
- [3] T. Belytschko, S. P. Xiao, G. C. Schatz, and R. S. Ruoff. Atomistic simulations of nanotube fracture. *Physical Review B*, 65:235430, 2002.
- [4] E. Benvenuti and A. Simone. One-dimensional nonlocal and gradient elasticity: Closed-form solution and size effect. *Mechanics Research Communications*, 48:46–51, 2013.
- [5] K. Chandraseker and S. Mukherjee. Coupling of extension and twist in single-walled carbon nanotubes. *Journal of Applied Mechanics*, 73:315–326, 2006.
- [6] T. Chang. A molecular based anisotropic shell model for single-walled carbon nanotubes. *Journal of the Mechanics and Physics of Solids*, 58:1422–1433, 2010.
- [7] T. Chang and H. Gao. Size-dependent elastic properties of a single-walled carbon nanotube via a molecular mechanics model. *Journal of the Mechanics and Physics of Solids*, 51:1059–1074, 2003.

- [8] T. Chang, J. Geng, and X. Guo. Prediction of chirality- and size-dependent elastic properties of single-walled carbon nanotubes via a molecular mechanics model. *Proceedings of the Royal Society A: Mathematical, Physical and Engineering Science*, 462:2523–2540, 2006.
- [9] B. G. Demczyk, Y. M. Wang, J. Cumings, M. Hetman, W. Han, A. Zettl, and R. O. Ritchie. Direct mechanical measurement of the tensile strength and elastic modulus of multiwalled carbon nanotubes. *Materials Science and Engineering A*, 334:173–178, 2002.
- [10] W. H. Duan, C. M. Wang, and Y. Y. Zhang. Calibration of nonlocal scaling effect parameter for free vibration of carbon nanotubes by molecular dynamics. *Journal of Applied Physics*, 101:024305–024305, 2007.
- [11] A. C. Eringen. On differential equations of nonlocal elasticity and solutions of screw dislocation and surface waves. *Journal of Applied Physics*, 54:4703–4710, 1983.
- [12] A. C. Eringen. *Nonlocal Continuum Field Theories*. Springer-Verlag, 2002.
- [13] J. Geng and T. Chang. Non linear stick-spiral model for predicting mechanical behavior of single-walled carbon nanotubes. *Physical Review B*, 74:245428, 2006.
- [14] Y. G. Hu, K. M. Liew, and Q. Wang. Nonlocal continuum model and molecular dynamics for free vibration of single-walled carbon nanotubes. *Journal of nanoscience and nanotechnology*, 11:10401–10407, 2011.
- [15] J. Y. Huang, S. Chen, Z. F. Ren, Z. Q. Wang, D.Z. Wang, M. Vaziri, Z. Suo, G. Chen, and M. S. Dresselhaus. Kink formation and motion in carbon nanotubes at high temperatures. *Physical Review Letters*, 97:075501, 2006.
- [16] Y. Huang, J. Wu, and K. C. Hwang. Thickness of graphene and single-wall carbon nanotubes. *Physical Review B*, 74:245413, 2006.
- [17] T. J. R. Hughes, J. A. Cottrell, and Y. Bazilevs. Isogeometric analysis: CAD, finite elements, NURBS, exact geometry and mesh refinement. *Computer Methods in Applied Mechanics and Engineering*, 194(39):4135–4195, 2005.
- [18] A. L. Kalamkarov, A. V. Georgiades, S. K. Rokkam, V. P. Veedu, and M. N. Ghasemi-Nejhad. Analytical and numerical techniques to predict carbon nanotubes properties. *International Journal of Solids and Structures*, 43:6832–6854, 2006.
- [19] F. Khademolhosseini, A. Srikantha Phani, A. Nojeh, and N. Rajapakse. Nonlocal continuum modeling and molecular dynamics simulation of torsional vibration of carbon nanotubes. *IEEE Transactions on Nanotechnology*, 11:34–43, 2012.
- [20] J. Kołoczek, Y.-K. Kwon, and A. Burian. Characterization of spatial correlations in carbon nanotubes-modelling studies. *Journal of Alloys and Compounds*, 328:222–225, 2001.

- [21] E. G. Lewars. *Computational chemistry: Introduction to the theory and applications of molecular and quantum mechanics*. Springer, 2010.
- [22] C. Li and T.-W. Chou. A structural mechanics approach for the analysis of carbon nanotubes. *International Journal of Solids and Structures*, 40:2487–2499, 2003.
- [23] G. Van Lier, C. Van Alsenoy, V. Van Doren, and P. Geerlings. Ab initio study of the elastic properties of single-walled carbon nanotubes and graphene. *Chemical Physics Letters*, 326:181–185, 2000.
- [24] K. M. Liew, X. Q. He, and C. H. Wong. On the study of elastic and plastic properties of multi-walled carbon nanotubes under axial tension using molecular dynamics simulation. *Acta Materialia*, 52:2521–2527, 2004.
- [25] J. P. Lu. Elastic properties of carbon nanotubes and nanoropes. *Physical Review Letters*, 79:1297, 1997.
- [26] M. Malagù, E. Benvenuti, C. A. Duarte, and A. Simone. One-dimensional nonlocal and gradient elasticity: Assessment of high order approximation schemes. *Computer Methods in Applied Mechanics and Engineering*, 275:138–158, 2014.
- [27] M. Meo and M. Rossi. Prediction of Young’s modulus of single wall carbon nanotubes by molecular-mechanics based finite element modelling. *Composites Science and Technology*, 66:1597–1605, 2006.
- [28] S. Narendar, D. Roy Mahapatra, and S. Gopalakrishnan. Prediction of nonlocal scaling parameter for armchair and zigzag single-walled carbon nanotubes based on molecular structural mechanics, nonlocal elasticity and wave propagation. *International Journal of Engineering Science*, 49:509–522, 2011.
- [29] J. Nocedal and S. J. Wright. *Numerical optimization*. Springer, 2006.
- [30] A. Pantano, D. M. Parks, and M. C. Boyce. Mechanics of deformation of single- and multi-wall carbon nanotubes. *Journal of the Mechanics and Physics of Solids*, 52: 789–821, 2004.
- [31] J. Peng, J. Wu, K. C. Hwang, J. Song, and Y. Huang. Can a single-wall carbon nanotube be modeled as a thin shell? *Journal of the Mechanics and Physics of Solids*, 56:2213–2224, 2008.
- [32] R. C. Picu. The Peierls stress in non-local elasticity. *Journal of the Mechanics and Physics of Solids*, 50:717–735, 2002.
- [33] S. Plimpton. Fast parallel algorithms for short-range molecular dynamics. *Journal of Computational Physics*, 117:1–19, 1995.
- [34] P. Poncharal, Z. L. Wang, D. Ugarte, and W. A. De Heer. Electrostatic deflections and electromechanical resonances of carbon nanotubes. *Science*, 283:1513–1516, 1999.
- [35] R. Rafiee and R. M. Moghadam. On the modeling of carbon nanotubes: A critical review. *Composites part B: Engineering*, 56:435–449, 2014.

- [36] D. C. Rapaport. *The art of molecular dynamics simulation*. Cambridge University Press, 2004.
- [37] S. Reich, C. Thomsen, and J. Maultzsch. *Carbon nanotubes: Basic concepts and physical properties*. John Wiley & Sons, 2008.
- [38] C. Q. Ru. Effect of van der Waals forces on axial buckling of a double-walled carbon nanotube. *Journal of Applied Physics*, 87:7227–7231, 2000.
- [39] C. Q. Ru. Effective bending stiffness of carbon nanotubes. *Physical Review B*, 62:9973, 2000.
- [40] C. Q. Ru. Chirality-dependent mechanical behavior of carbon nanotubes based on an anisotropic elastic shell model. *Mathematics and Mechanics of Solids*, 14:88–101, 2008.
- [41] D. Sánchez-Portal, E. Artacho, J. M. Soler, A. Rubio, and P. Ordejón. Ab initio structural, elastic, and vibrational properties of carbon nanotubes. *Physical Review B*, 59:12678, 1999.
- [42] L. Shen and J. Li. Transversely isotropic elastic properties of single-walled carbon nanotubes. *Physical Review B*, 69:045414, 2004.
- [43] F. Shimizu, S. Ogata, and J. Li. Theory of shear banding in metallic glasses and molecular dynamics calculations. *Materials Transactions*, 48:2923–2927, 2007.
- [44] L. J. Sudak. Column buckling of multiwalled carbon nanotubes using nonlocal continuum mechanics. *Journal of Applied Physics*, 94:7281–7287, 2003.
- [45] H. Tashakori, B. Khoshnevisan, and F. Kanjuri. Ab initio systematic study of chirality effects on phonon spectra, mechanical and thermal properties of narrow single walled carbon nanotubes. *Computational Materials Science*, 83:16–21, 2014.
- [46] K. I. Tserpes and P. Papanikos. Finite element modeling of single-walled carbon nanotubes. *Composites part B: Engineering*, 36:468–477, 2005.
- [47] C. Y. Wang, C.Q. Ru, and A. Mioduchowski. Axially compressed buckling of pressured multiwall carbon nanotubes. *International Journal of Solids and Structures*, 40:3893–3911, 2003.
- [48] L. Wang, Q. Zheng, J. Z. Liu, and Q. Jiang. Size dependence of the thin-shell model for carbon nanotubes. *Physical Review Letters*, 95:105501, 2005.
- [49] B. WenXing, Z. ChangChun, and C. WanZhao. Simulation of Young’s modulus of single-walled carbon nanotubes by molecular dynamics. *Physica B*, 352:156–153, 2004.
- [50] J. Wu, K. C. Hwang, and Y. Huang. An atomistic-based finite-deformation shell theory for single-wall carbon nanotubes. *Journal of the Mechanics and Physics of Solids*, 56:279–292, 2008.

- [51] J. R. Xiao, B. A. Gama, and J. W. Gillespie Jr. An analytical molecular structural mechanics model for the mechanical properties of carbon nanotubes. *International Journal of Solids and Structures*, 42:3075–3092, 2005.
- [52] Z. Xin, Z. Jianjun, and O.Y. Zhong-Can. Strain energy and young's modulus of single-wall carbon nanotubes calculated from electronic energy-band theory. *Physical Review B*, 62(20):13692, 2000.
- [53] B. I. Yakobson, C. J. Brabec, and J. Bernholc. Nanomechanics of carbon tubes: Instabilities beyond linear response. *Physical Review B*, 76:2511, 1996.
- [54] N. Yao and V. Lordi. Young's modulus of single-walled carbon nanotubes. *Journal of Applied Physics*, 84:1939–1943, 1998.
- [55] J. Yoon, C. Q. Ru, and A. Mioduchowski. Timoshenko-beam effects on transverse wave propagation in carbon nanotubes. *Composites Part B: Engineering*, 35:87–93, 2004.
- [56] Y. Q. Zhang, G. R. Liu, and X. Y. Xie. Free transverse vibrations of double-walled carbon nanotubes using a theory of nonlocal elasticity. *Physical Review B*, 71:195404, 2005.

Chapter 4

A molecular-dynamics study of size and chirality effects on glass-transition temperature and ordering in carbon nanotube-polymer composites*

We carry out molecular-dynamics simulations of single-walled carbon nanotubes (CNTs) embedded in a coarse-grained amorphous monodisperse polyethylene-like model system. The roles of nanotube diameter and chirality on the physical and structural properties of the composite are thoroughly discussed for several CNTs with different diameter and chirality. We show that the glass-transition temperature of the polymer matrix increases with the diameter of the CNT while chirality effects are negligible. A denser and ordered layered region of polymer matrix is found in the vicinity of the nanotube surface. The density and ordering of this layer increases with the CNT diameter. All simulations indicate that chirality does not affect the atomic structure of the highly ordered layer surrounding the CNTs. Despite the simplicity of the polymer model, our results are qualitatively comparable with those obtained from experiments and numerical simulations that consider a chemically-specific polymer matrix.

4.1 Introduction

When carbon nanotubes (CNTs) are used as inclusions in polymeric materials, important changes in the atomic structure of the hosting matrix can take place. Experimental evidence on a large class of CNT-polymer composites indicates that nanotubes can promote crystallization [1, 3, 8, 17, 19, 38, 39, 48, 59]. Despite the growing interest in carbon nanotube-polymer composites, CNT-induced effects on the polymer structure are still not well characterized due to the complexity of the interactions at the nanoscale [4, 28, 36, 52]. Several factors can influence the nucleating effect of CNTs [35]: nanotube diameter and chirality, presence of surface functional groups, use of surfactants, CNT volume fraction, and type of polymer (it is worth mentioning that, besides CNT-induced crystallization, negligible [25] and anti-nucleation [16, 23] effects have been observed in a small number of

*Reproduced from: M. Malagù, A. Lyulin, E. Benvenuti and A. Simone, A molecular-dynamics study of size and chirality effects on glass-transition temperature and ordering in carbon nanotube-polymer composites, *Macromolecular Theory and Simulations*, 25:571–581, 2016.

polymer types). Here, by using molecular-dynamics (MD) simulations, we present a preliminary study of CNT-induced ordering with a focus on the roles of CNT diameter and chirality.

The nucleation of a crystallized polymer layer around a nanotube is highly beneficial to the enhancement of the composite thermal and mechanical properties [14, 18, 30]. Although changes in the structure of the polymer matrix are limited to the nanoscale, their influence at the macroscopic level is significant [15, 24, 30, 42]. A detailed characterization of the atomic structure of the crystallized polymer layer, however, is not trivial. Being the nanotube size comparable to the characteristic length scale of the matrix atomic structure, the size of the CNT diameter might influence the ordering of the polymer chains. As observed experimentally from the analysis of crystallized polyethylene on different nanofillers [40] (single- and multi-walled CNTs, carbon nanofibers and graphene), small-diameter fibers cause the polymer chains to align along their axis. In addition, molecular crystallization might also be influenced by the CNT chirality [35].

The experimental quantification of structurally-induced effects of the CNT on the polymer matrix is very difficult to accomplish due to the small size of the crystallized layer [55]. Moreover, it would be extremely challenging to isolate effects from other sources (e.g. preparation procedure and experimental technique). For these reasons, molecular-dynamics, which is here used to study structure and mobility of the polymer chains surrounding the nanotubes, has been typically employed. Minoia et al. [47] reported diameter effects on the structure and adhesion of single polyethylene chains on single-walled CNTs and negligible chirality effects. In contrast, Wei [56] observed chirality effects from MD simulations on single-walled CNTs surrounded by one layer of polyethylene chains. To investigate the more complex structure of a composite having a large number of polymer chains, Falkovich et al. [21] compared the ordering of an R-BAPB polyimide matrix in the vicinity of a flat graphene layer and a small diameter single-walled CNT. Their results show higher ordering in the case of the graphene sheet. However, their study does not provide a comprehensive description of diameter-induced modifications (only one nanotube was considered) and does not explore chirality effects. Furthermore, all the above results might be limited to the specific polymer considered in the simulations. Hence, a detailed and more fundamental understanding of CNT-induced effects and the interaction between polymer chains and filler is still lacking.

The purpose of this study is therefore twofold: to assess nanotube-induced effects on the atomic structure of the surrounding polymer matrix, and to provide a description of size and chirality effects that can be observed in a wide range of single-walled CNT-polymer composites. In the MD simulations we employ a simple model of a CNT-polymer composite consisting of a single single-walled CNT embedded in a polymer matrix. We also avoid polymer chemistry-specific effects by using a simplified polyethylene-like coarse-grained (CG) model that has the added advantage of reducing the computational effort for the long relaxation time of the system –this simplified CG model is intended for the investigation of CNT-induced effects on an amorphous monodisperse polymer polyethylene-like matrix rather than on a specific polymer matrix. Diameter and chirality effects are here explored by means of a detailed fully-atomistic single-walled CNT model. Non-bonded interactions are defined between nanotube and polymer chains and within the polymer chains.

To assess the influence of the nanotube-polymer interaction, the variation of the composite glass-transition temperature is discussed. Next, a comprehensive and detailed analysis of

the structural properties of single-walled CNT-polymer composites is carried out by investigating density profile and ordering of the polymer chains around the nanotube. Throughout the chapter, we qualitatively compare our results with experimental and modeling literature findings to validate the reliability of the atomistic model.

All the simulations and the corresponding results will help to elucidate nanotube-induced diameter and chirality effects at the level of the structure of the interface of the hosting polymer matrix. To the best of our knowledge, none of the previous studies in the literature provides such an extensive investigation and a basic understanding of single-walled carbon nanotube-effects in polymer-based composites.

4.2 Model and simulation details

Since we are interested in exploring features of an archetype single-walled CNT-polymer composite, a CG model is adopted for the polymer chains. Effects induced by the specific chemistry of the polymer matrix are therefore not considered. In view of the investigation of size and chirality effects, a fully-atomistic representation of different single-walled CNTs is employed. Despite its simplicity, this atomistic model yields results in agreement with those from experiments and atomistic simulations with real polymers as discussed in the next section.

In the simulations, each polymer chain consists of 300 identical monomeric units, here referred to as beads. Assuming r as the distance between two beads, covalently bonded interactions are described by the interatomic potential

$$U(r) = -0.5KR_0^2 \ln \left[1 - \left(\frac{r}{R_0} \right)^2 \right] + 4\varepsilon_p \left[\left(\frac{\sigma_p}{r} \right)^{12} - \left(\frac{\sigma_p}{r} \right)^6 + \frac{1}{4} \right]. \quad (4.1)$$

The first term, which is attractive and defined according to the Finitely Extensible Nonlinear Elastic (FENE) potential [34], depends on the stiffness K and the maximum elongation R_0 of the polymer bonds. The second term, which, conversely, is repulsive, is a truncated Lennard-Jones (LJ) potential defined in terms of beads characteristic length-scale σ_p and energy ε_p parameters. Although common practice suggests the use of dimensionless LJ units for the quantities in (4.1), Kremer and Grest [34] suggested some values by comparing the dynamics of entangled FENE chains melts and real polymers. Accordingly, we take parameters σ_p , ε_p , K and R_0 equal to 5.1 Å, 0.8903 kcal/mol, $30\varepsilon_p/\sigma_p^2$ and $1.5\sigma_p$, respectively. These values were suggested for amorphous monodisperse polyethylene-like systems. The interatomic potential (4.1) does not include bending and torsional contributions. Hence, the effect of the polymer chains flexibility on the physical properties of the composite is not examined in this work. The modified Morse potential [7] is employed to model the CNTs adopting the same parameters defined in our previous work [44]. Further, the 12-6 Lennard-Jones potential has been considered for polymer-polymer and polymer-CNT non bonded interactions. In particular, the parameters σ_{pc} and ε_{pc} for the LJ interactions between polymer beads and CNT carbon atoms are calculated with the Lorentz-Berthelot rules

$$\sigma_{pc} = \frac{1}{2} (\sigma_p + \sigma_c) \quad \text{and} \quad \varepsilon_{pc} = \sqrt{\varepsilon_p \varepsilon_c}, \quad (4.2)$$

where σ_c and ϵ_c are the LJ parameters for CNT carbon atoms [11].

The starting configuration of a CNT-polymer composite was generated by randomly packing stretched polymer chains in a large simulation box with one single-walled CNT at the center aligned in the z -axis—the Packmol package [46] was used for this task. The number of polymer chains, which depends on the nanotube diameter, corresponds to a nanotube volume ratio v^{CNT} approximately equal to 0.6% [26, 30] at 100 K and to a weight fraction w^{CNT} of approximately 2% (see Tables 4.1 and 4.2). The initial configurations were relaxed at the rather high initial temperature of 800 K in an NVT ensemble for 0.5 ns. Since the volume of the CNT and the density of polymer at 800 K are known, the approximated volume of the composite at that temperature can be estimated. This information was used in the next step where the size of the simulation box was reduced until the desired volume was reached. Each system was further relaxed at 800 K in an NPT ensemble at 0 atm—indistinguishable from 1 atm since pressure fluctuations are in the range of about ± 50 atm—for 10 ns, a period that was long enough to reach equilibration (checked by measuring the variation of the energy). This initialization phase, used to reach the equilibrium volume of the composite, was preferred over a single NPT ensemble since it leads to a shorter computational time and equivalent equilibrated configurations. Finally, all systems were further cooled down in an NPT ensemble at a cooling rate of 0.1 K/ps (see Figure 4.1 for a typical snapshot of an (8,8)-polymer composite at 100 K).

	(6,6)-polymer	(8,8)-polymer	(10,10)-polymer	(12,12)-polymer
d [Å]	8.14	10.86	13.57	16.28
v^{CNT} [%]	0.64	0.62	0.62	0.62
w^{CNT} [%]	2.09	2.00	1.98	1.95

Table 4.1: Diameter d of the embedded armchair single-walled CNTs and nanotube volume fraction v^{CNT} and weight fraction w^{CNT} in the (n,n) -polymer composites.

	(10,0)-polymer	(14,0)-polymer	(17,0)-polymer	(21,0)-polymer
d [Å]	7.83	10.97	13.32	16.45
v^{CNT} [%]	0.63	0.62	0.62	0.62
w^{CNT} [%]	2.08	2.00	1.98	1.95

Table 4.2: Diameter d of the embedded zigzag single-walled CNTs and nanotube volume fraction v^{CNT} and weight fraction w^{CNT} in the $(n,0)$ -polymer composites.

All simulations have been performed using the Large-scale Atomic/Molecular Massively Parallel Simulator (LAMMPS) software package [50]. We choose periodic boundary conditions in all three directions. The Newton’s equations of motion were integrated with the velocity Verlet algorithm using a time step of 1 fs. The Nosé-Hoover thermostat and barostat were used. For each system, three different initial configurations were generated and the corresponding results were averaged. The LAMMPS input scripts can be downloaded from the authors’ website.

Next, four armchair ((6,6), (8,8), (10,10) and (12,12)) and four zigzag ((10,0), (14,0), (17,0) and (21,0)) nanotubes with different diameters are used to assess chirality and size ef-

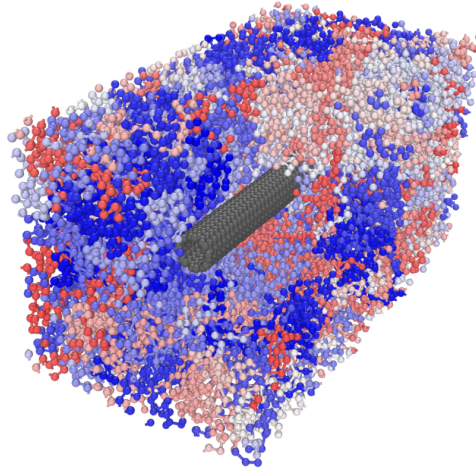


Figure 4.1: Illustration of an (8,8)-polymer composite equilibrated at 100 K (part of the polymer matrix has been removed for better visualization of the embedded nanotube). Polymer chains are displayed in different colors, the nanotube in gray.

facts. Throughout the chapter, the standard notation employing the couple of integers (n, m) to describe single-walled CNTs [20] is adopted. Moreover, the notation (n, m) -polymer denotes a polymer composite with an (n, m) single-walled CNT. The diameter of the nanotubes was calculated as

$$d = \frac{a_{cc} \sqrt{3(n^2 + m^2 + nm)}}{\pi} + t \quad (4.3)$$

where $a_{cc} = 1.421 \text{ \AA}$ is the length of the carbon-carbon bonds and $t = 3.4 \text{ \AA}$ the nanotube thickness [33].

4.3 Results and discussion

4.3.1 Glass-transition temperature

In nanocomposites, the glass-transition temperature (T_g) is one of the simplest way to characterize the interaction between polymer chains and filler. Figure 4.2 shows the density-temperature curves for the bulk material and an (8,8)-polymer composite. The bulk T_g was estimated as 200.9 K and corresponds to the dimensionless quantity $0.448 \varepsilon_p/k_B$, with k_B the Boltzmann constant. This result is in good agreement with theoretical [51] and numerical [2, 6, 13] estimates for FENE polymer melts –these values vary between 0.43 and $0.47 \varepsilon_p/k_B$. The obtained T_g , however, is lower than that for real polyethylene (between 220 and 280 K [9, 10, 22, 29, 45]). Nevertheless, a quantitative comparison between the estimated glass-transition temperatures and those for real polyethylene is beyond the scope of the this study and the model employed in our simulations. The coarse-grained model for the polymer chains is employed to provide general insight into a wide range of polymer-

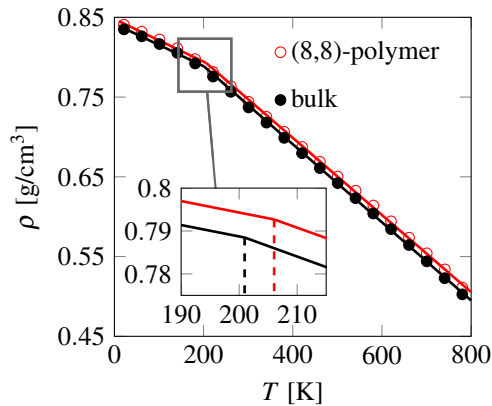


Figure 4.2: Density-temperature curves for bulk polymer and an (8,8)-polymer composite. Solid lines indicate linear fits to calculate the glass-transition temperature. Dashed lines denote the estimated value of T_g .

based materials. Indeed, as discussed next, the obtained results are in line with those from real composites. As depicted in Figure 4.2, the glass-transition temperature increases to $T_g = 206.0$ K for the case of the (8,8)-polymer composite denoting attractive interactions between the nanotube and the surrounding polymer chains [53]. More precisely, since the glass-transition temperature of the composite is higher than that of the bulk matrix, CNT-polymer interactions are stronger than those between polymer beads. Noteworthy, the variation of T_g is comparable with the variation obtained from experimental and numerical studies on real single-walled CNT-polymer composites. Liang and Tjong [41] estimated the glass-transition temperature of CNT-low density polyethylene composites about 10 K higher than that for pure polymer matrix. Grady et al. [27], from experiments on CNT-polystyrene composites with a nanotube weight fraction varying between 1 and 30%, reported T_g values 6-7 K higher than those for pure polystyrene. Sterzyński et al. [54] obtained the T_g of polyvinyl chloride matrix about 9 K lower than that of the corresponding CNT composite with a CNT concentration of 0.01-0.02 wt%. For poly(methyl methacrylate) composites an increase of about 2 K was observed with a content of CNTs of about 0.5 wt% [43]. Wei et al. [57], using molecular dynamics simulations of single-walled CNT-polyethylene composites, estimated T_g about 20 K higher than that of the bulk material.

The influence of the nanotube atomic structure on the glass-transition temperature was investigated as well. In Figure 4.3a, size and chirality effects on T_g are depicted for all simulated CNT-polymer composites.

Size effects

The composite glass-transition temperature, while remaining higher than the bulk T_g , clearly increases with the curvature of the nanotube (Figure 4.3a). This can be explained by considering that the number of non-bonded interactions between polymer beads and nanotube atoms increases with decreasing d [64] as shown in Figure 4.3b. Consequently, the mobility

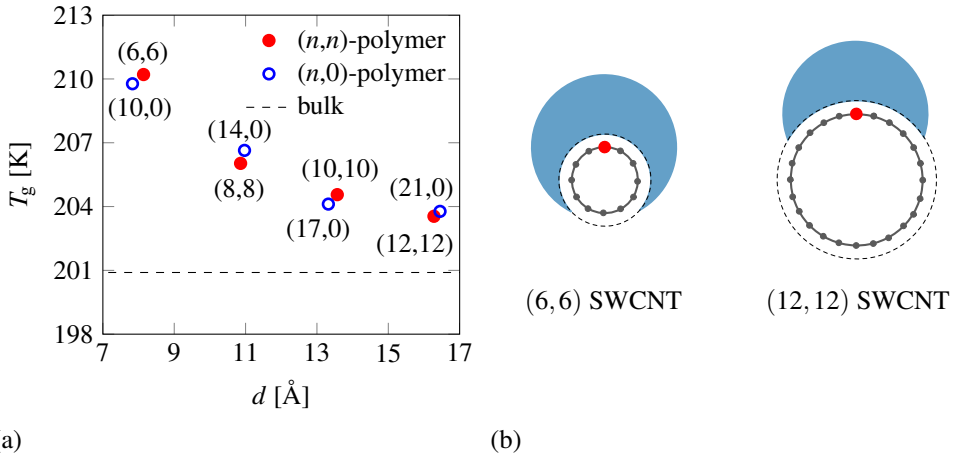


Figure 4.3: (a) Glass-transition temperature of (n,n) armchair and $(n,0)$ zigzag single-walled CNT-polymer composites as a function of the nanotube diameter d compared to the bulk glass-transition temperature. (b) Schematic of the interaction region (blue) of a single-walled CNT atom (red) with the surrounding polymer [64].

of the polymer chains surrounding the nanotubes decreases.

It is worth mentioning that also the value of the carbon nanotube weight fraction can influence T_g . Nevertheless, as indicated in Tables 4.1 and 4.2, the variation of w^{CNT} is small, especially if compared with the changes in the CNT diameter. Therefore, it is reasonable to assume that the trend of the composite glass-transition temperature T_g is mainly caused by the variation of the nanotube diameter d .

Chirality effects

As depicted in Figure 4.3a, the estimated values of T_g for armchair and zigzag composites differ by less than 1%. Since armchair and zigzag configurations represent the two extremes, minimum and maximum value, respectively, in terms of chirality, these results suggest that chirality-induced effects on T_g are negligible.

4.3.2 Density profiles

Typically, in confined geometries and polymer composites with particle inclusions, a better packing of monomer units is observed around the interface [5, 53]. As depicted in Figure 4.4, this is also the case for the single-walled CNT-polymer composites considered in this work. Concentric wall-induced layers can be identified around the nanotube. A detailed investigation of the density profile was therefore carried out to understand structural changes in the polymer matrix in the vicinity of the nanotube.

To start with, the evolution of the density profile at different temperatures has been examined. As illustrated in Figure 4.5, the number of wall-induced layers and their density increase while cooling the system. The intensity of the peaks is higher close to the nanotube

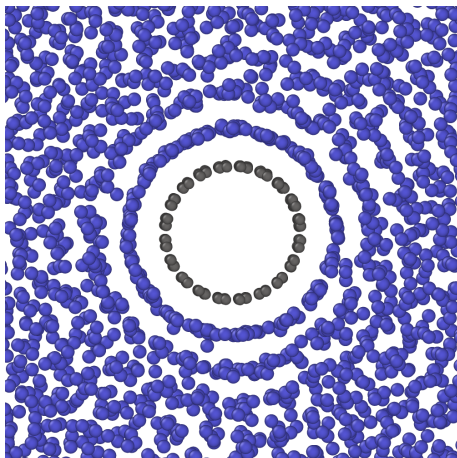


Figure 4.4: Snapshot of an (8,8)-polymer composite cross section at 100 K (monomer beads in blue, single-walled CNT carbon atoms in gray).

surface and it decays until the composite density equals that of the bulk. Noteworthy, the peak-to-peak distance remains constant and equal to about σ_p at all temperatures. This suggests that the bonds connecting two polymer beads in different layers (whose equilibrium distance is $0.97\sigma_p$) are mainly orthogonal to the nanotube surface and to its longitudinal axis. Consequently, a higher ordering of the monomers, which increases by decreasing the temperature, is observed around the nanotube (this will be discussed in more detail in the next section).

Size effects

Figure 4.6 shows a comparison of the density profiles for different armchair composites at (a) 800 and (b) 100 K. Similar profiles are observed for all the examined armchair composites. The number of layers and the peak-to-peak distance is the same. Moreover, the thickness of the perturbed region of polymer matrix (i.e. the interphase) does not change with the diameter of the nanotube—analogue results were obtained by Brown et al. [12] with MD simulations on a polymer matrix with spherical inclusions—and is about 25 Å. Therefore, as schematically shown in Figure 4.7, for CNT-polymer composites with equal v^{CNT} , the volume fraction of such interphase layer increases by decreasing the diameter of the nanotube. This size effect might have a role in the trend of T_g observed in Section 4.3.1 since the glass-transition temperature of the highly ordered polymer region is higher than that of the amorphous bulk polymer. Nonetheless, the density of the wall-induced layers increases with the nanotube diameter—weaker maxima and minima can be noticed for smaller nanotubes. This is in agreement with the results from Falkovich et al. [21] obtained with MD simulations of R-BAPB composites with graphene and a (5,5) CNT.

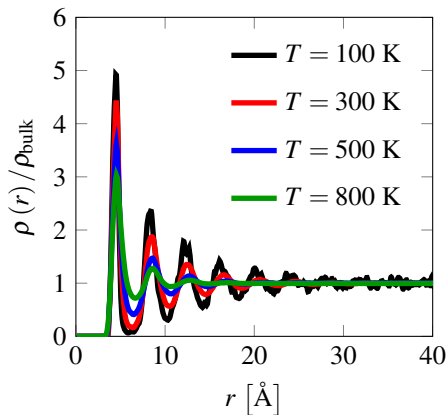


Figure 4.5: Density of an (8,8)-polymer composite at different temperatures as a function of distance r from the nanotube wall (all curves have been normalized with respect to the bulk density ρ_{bulk} at the corresponding temperature).

Chirality effects

Chirality effects on monomer packing are negligible. This can be deduced from Figure 4.8 where the density profiles of composites with single-walled CNT of comparable diameter ((12,12) armchair and (21,0) zigzag) are shown. Analogous conclusions hold for the other composites.

4.3.3 Ordering of monomers

Based on the analysis of the density profile, a higher ordering of the polymer bonds was observed in the vicinity of the nanotubes. However, the previous results do not provide a comprehensive description of the changes that nanotubes induce in the matrix monomer structure. In this section we carry out a detailed investigation into the orientation of the polymer bonds with respect to the nanotube longitudinal axis and surface.

Similar to Falkovich et al. [21], we employed histograms showing the probability P of the orientation of the polymer bonds as a function of the distance from the nanotube wall. The monomer orientation is measured according to the angles ϕ and θ between the polymer bonds and the nanotube axis and surface, respectively. The results are derived by averaging the bond orientation sampled every 5 ps within a time interval of 10 ns. The bin size of the histograms was chosen equal to 1° for both angles ϕ and θ and 1 \AA for the distance r .

The ordering of the monomers was first assessed in a polymer matrix system without carbon nanotube. In this case, we estimated the probability of the bonds to align with the x -axis of the simulation unit cell (analogous results were produced estimating P with respect to the y - and z -axis). As depicted in Figure 4.9, the histogram evaluated at 100 K does not show preferential orientations of the polymer bonds. Therefore, in absence of carbon nanotubes, the matrix is amorphous. In contrast to this, as illustrated in Figures 4.10a and 4.11a for an (8,8)-polymer composite, higher ordering is already visible at 800 K in the polymer interfa-

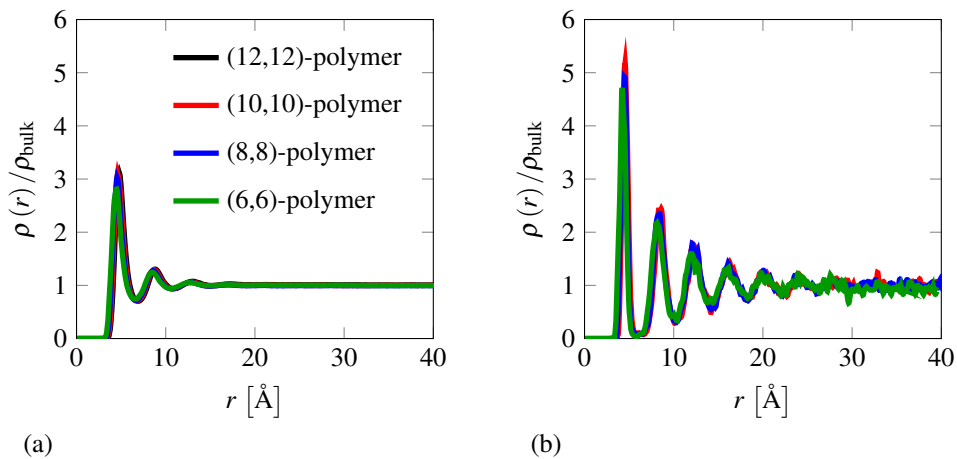


Figure 4.6: Density profile for different armchair composites at (a) 800 K and (b) 100 K as a function of distance r from the single-walled CNT wall (all curves are normalized with respect to the bulk density ρ_{bulk} at the corresponding temperature).

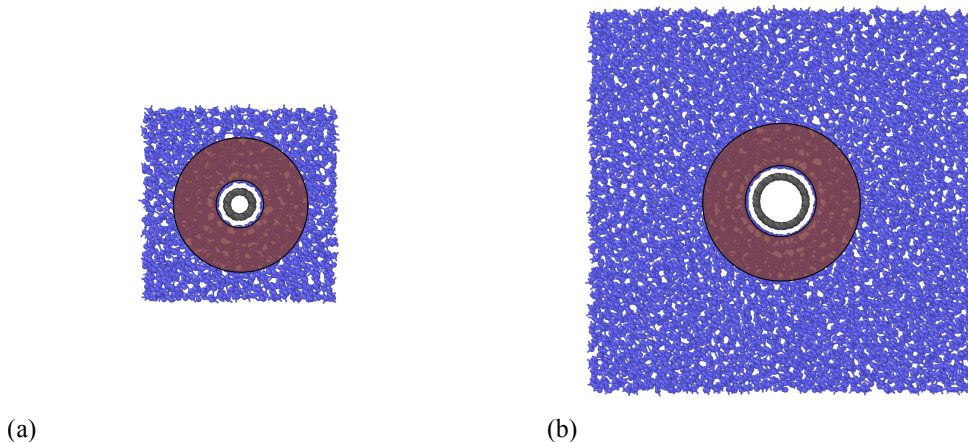


Figure 4.7: Schematic showing the region of polymer with higher ordering (highlighted in brown) in (a) (6,6) and (b) (12,12) single-walled CNT-polymer composites with $v^{\text{CNT}} = 0.6\%$. Since the thickness of the perturbed polymer phase, about 25 \AA , does not change with the nanotube diameter d , its volume fraction increases by decreasing d .

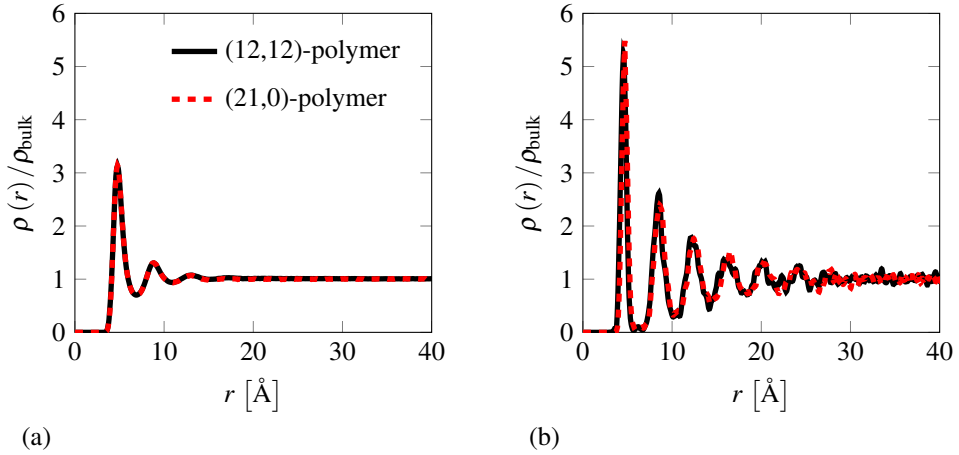


Figure 4.8: Density profile for (12,12) armchair and (21,0) zigzag single-walled CNT-polymer composites at (a) 800 K and (b) 100 K as a function of distance r from the nanotube wall (all curves are normalized with respect to the bulk density ρ_{bulk} at the corresponding temperature).

cial layer ($r \sim 4\text{-}5$ Å). In particular, while the ordering with respect to the nanotube axis is very mild, most of the polymer bonds are nearly parallel to the nanotube surface. By decreasing the temperature, the ordering increases and more ordered layers form (see Figure 4.10b-d and 4.11b-d). In the first layer, located between 4 and 5 Å from the nanotube wall, the probability of orientation along the nanotube axis presents a high peak between 0 and 5° and, especially at low temperatures, lower peaks at larger values of ϕ . Regarding θ , we observe only one peak at 0-10°. This suggests that polymer bonds at the interface, while being parallel to the nanotube surface, are preferentially aligned with the nanotube axis. Conversely, in the second layer positioned at 6-7 Å, polymer bonds are mainly orthogonal to the nanotube surface since the angle distribution peaks are at 70-90° for ϕ and θ . This pattern of alternating layers of parallel and orthogonal bonds repeats while moving far from the interface. However, the ordering decays with r since the influence of the nanotube over the polymer atoms vanishes. These results indicate the nucleation of an ordered region that has been experimentally observed in several real single-walled CNT-polymer composites [35], as widely reported for CNT-polyethylene [28, 38, 39, 61–63]. Analogous observations were made for other semi-crystalline polymers such as isotactic polypropylene [3, 26, 49], poly(vinylidene difluoride) [37, 58] and poly(vinyl alcohol) [14, 60]. Based on Raman spectroscopy on CNT-poly(ϵ -caprolactone), Chatterjee and coworkers [15] showed the formation of an ordered polymer structure oriented along the surface of the nanotubes. Regarding amorphous polymers, Dingemans and coworkers [30–32] reported the growth of a crystalline domain of polyetherimide matrix along the CNT surface.

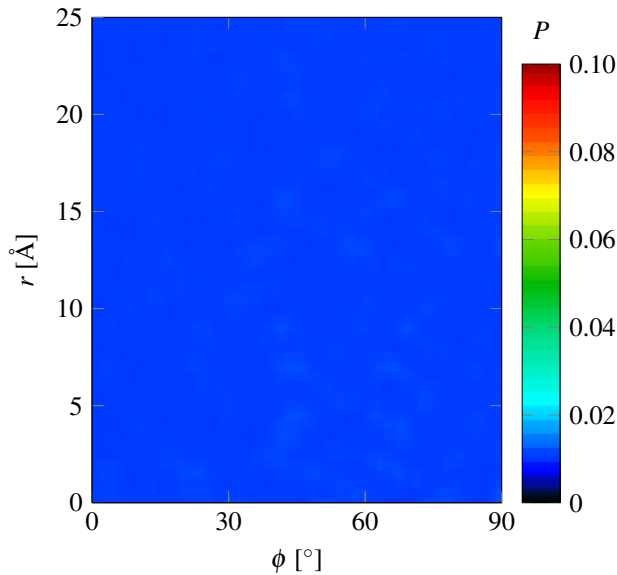


Figure 4.9: Probability P of the angle ϕ between the polymer bonds and the x -axis of the unit cell for a pure polymer matrix system at 100 K. Histograms at higher temperatures are analogous, indicating no high ordering for the pure polymer matrix.

Size effects

A quantitative assessment of size effects on the monomer ordering is shown in Figure 4.12 based on the estimation of the fraction $\psi_\alpha(r)$ of polymer bonds not exceeding a given angle α with the nanotube axis. The results have been reported only for (6,6)-polymer and (12,12)-polymer composites. At 800 and 100 K, the fraction ϕ_α of monomer bonds shows a high peak at $r = 4 - 5 \text{ \AA}$ and then decreases moving far from the nanotube surface. This denotes the higher ordering of the polymer matrix in the vicinity of the nanotube as previously discussed. At 800 K size effects are minimal. On the contrary, at 100 K, stronger ordering is noticed for the composite with the nanotube with larger diameter. Consequently, increasing the nanotube curvature hinders the ordering of the surrounding polymer chains. For temperatures between 800 and 100 K (e.g. 300 K) we observed results in between those shown in Figure 4.12. Minoia et al. [47], performing MD simulations at 300 K of single polymer chains on single-walled CNTs, related this diameter effect to the higher binding energy observed in the case of nanotube with lower curvature as more bending of the polymer chains is required to maintain their atoms in close contact with small diameter CNTs. Although a bending contribution is not explicitly implemented in the FENE potential, the repulsive term in (4.1) provides flexural stiffness to the polymer chains. Therefore, despite the increase of CNT-polymer interaction for smaller nanotubes (as illustrated in Figure 4.3b), higher ordering is observed when the curvature of the nanotube decreases.

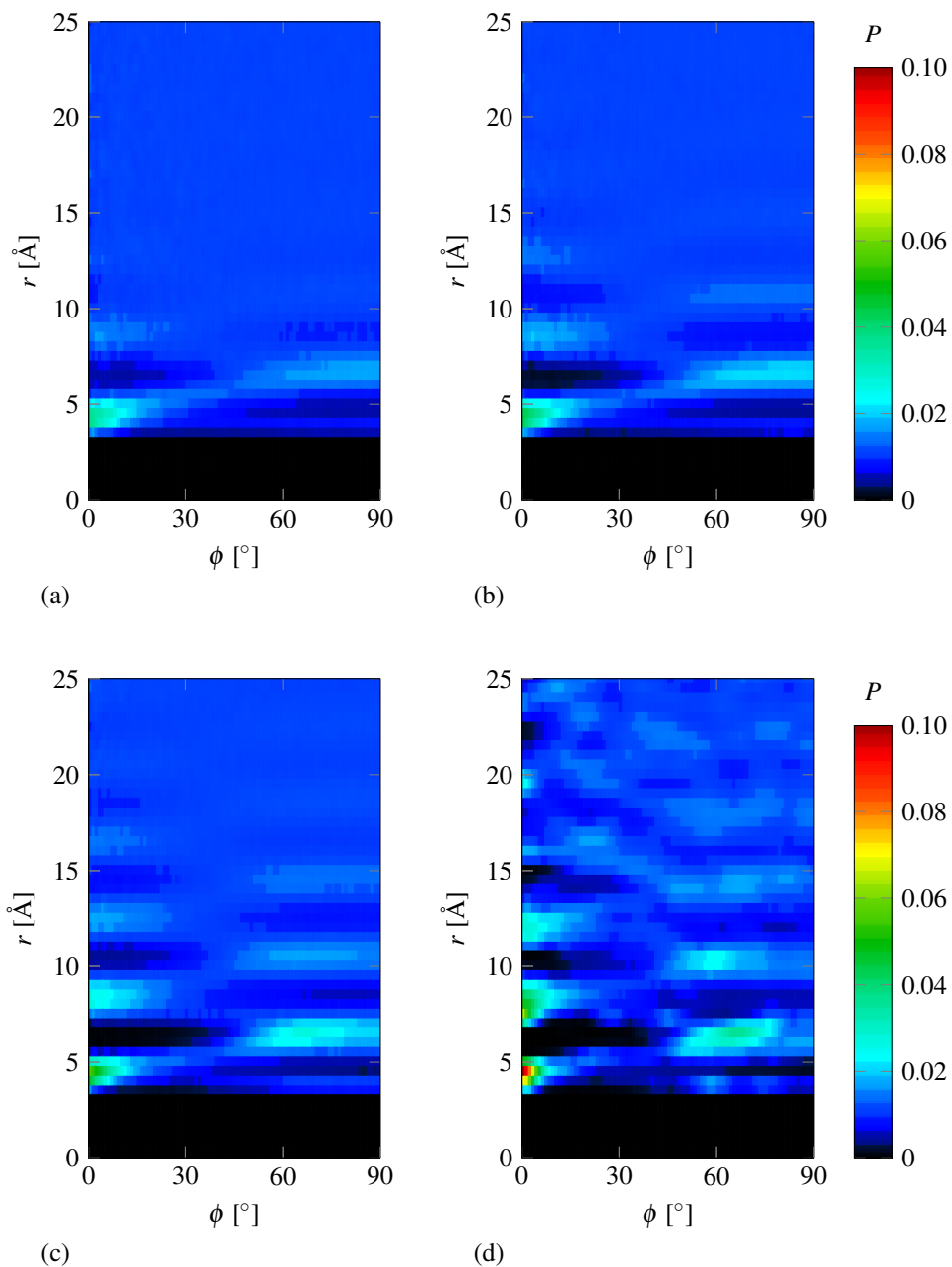


Figure 4.10: Probability P of the angle ϕ between the polymer bonds and the longitudinal axis of an (8,8) single-walled CNT at (a) 800, (b) 500, (c) 300 and (d) 100 K: the nanotube initiates high ordering at the interface. The ordering increases while cooling the system.

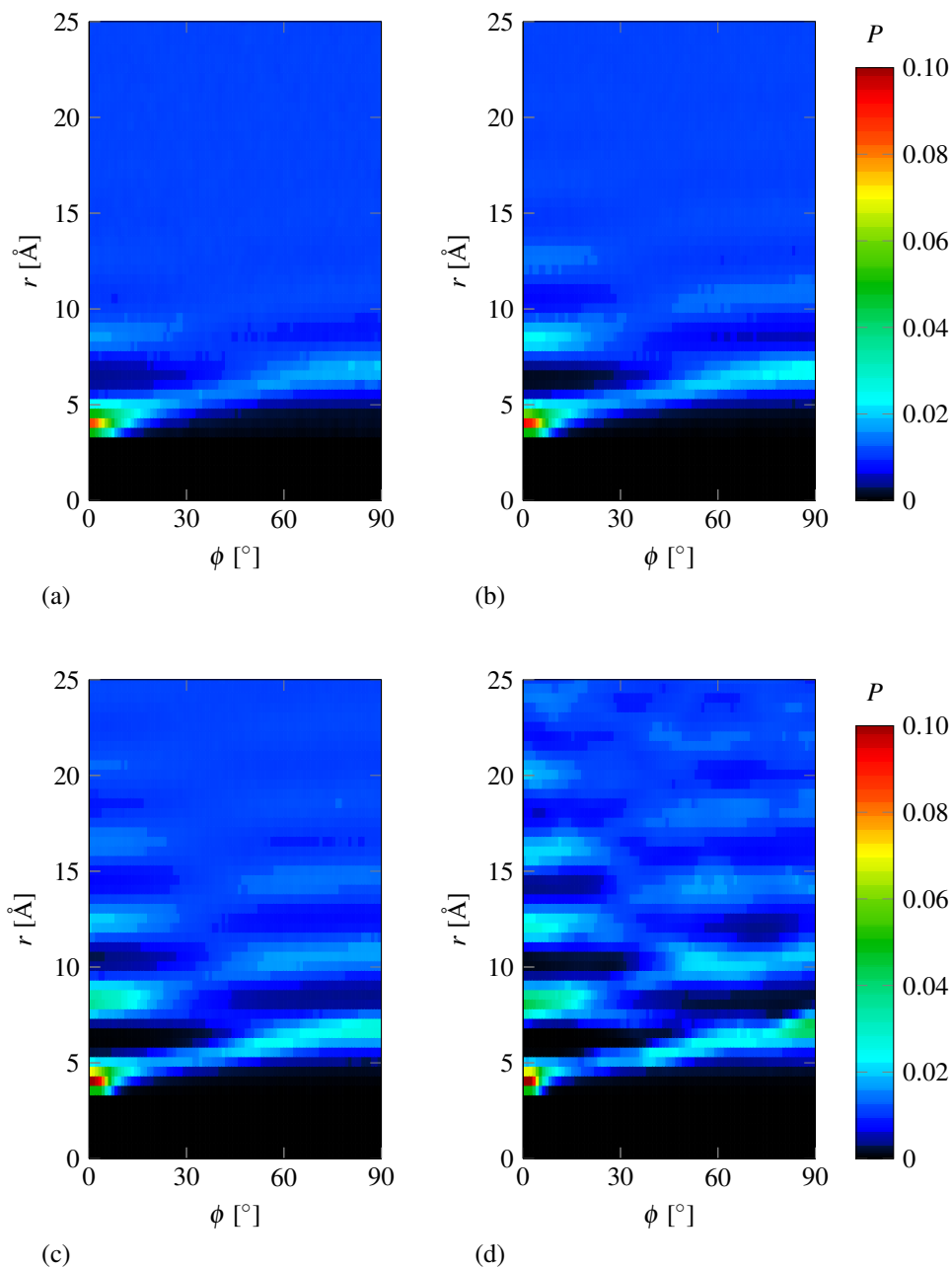


Figure 4.11: Probability P of the angle θ between the polymer bonds and the surface of an (8,8) single-walled CNT at (a) 800, (b) 500, (c) 300 and (d) 100 K: the nanotube initiates high ordering at the interface. The ordering increases while cooling the system.

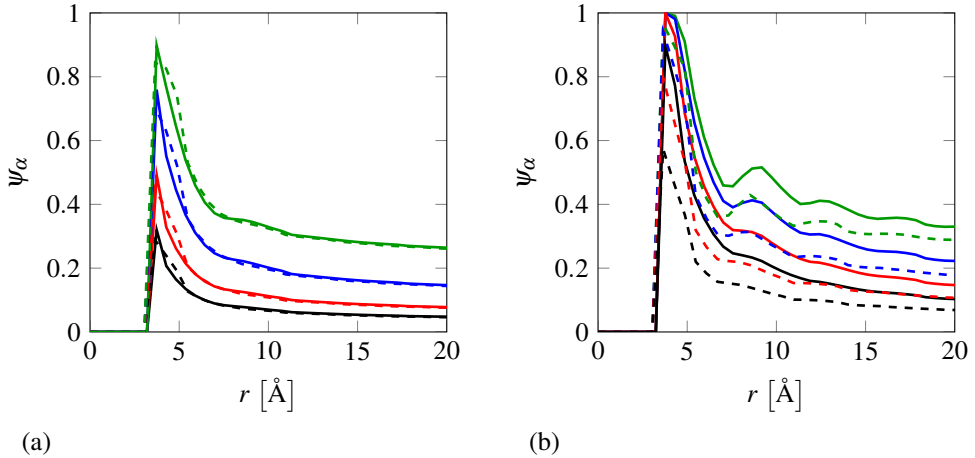


Figure 4.12: Fraction ϕ_α of monomer bonds at a distance r from the nanotube wall and at an angle $\theta < \alpha$ to the axis of armchair (12,12) (solid lines) and (6,6) (dashed lines) single-walled CNTs at (a) 800 and (b) 100 K. The angle α is equal to 2.5° (black lines), 5° (red lines), 10° (blue lines) and 20° (green lines).

Chirality effects

Figure 4.13 shows that the $\psi_\alpha(r)$ profiles for (12,12) armchair single-walled CNTs are closely akin to those obtained with (21,0) zigzag nanotubes. The small differences in $\psi_\alpha(r)$ arise from the size effects—the (21,0) zigzag single-walled CNT, having a larger diameter, leads to a slightly higher ordering. Therefore, as observed for the variation of T_g and the density profile, chirality effects in armchair and zigzag composites are negligible.

4.4 Conclusions

We assessed diameter and chirality effects on physical and structural properties of single-walled CNT-polymer composites by means of molecular-dynamics simulations. Attractive non-bonded interactions between the polymer matrix and the carbon nanotube yield a composite glass-transition temperature higher than that of the bulk matrix and a highly ordered layer of polymer chains in the vicinity of the nanotube wall. In particular, our simulations revealed that density and monomer ordering of the polymer matrix rapidly increase close to the nanotube surface. The main conclusions regarding size and chirality effects are summarized below.

Size effects The glass-transition temperature of the composite increases with the curvature of the nanotube while the thickness of the highly ordered layer surrounding the nanotubes does not change with the size of the nanotube. Nevertheless, the nanotube diameter influences its density profile and ordering. Namely, increasing the nanotube diameter increases the ordering of the polymer chains around the nanotube surface. Therefore, the results show

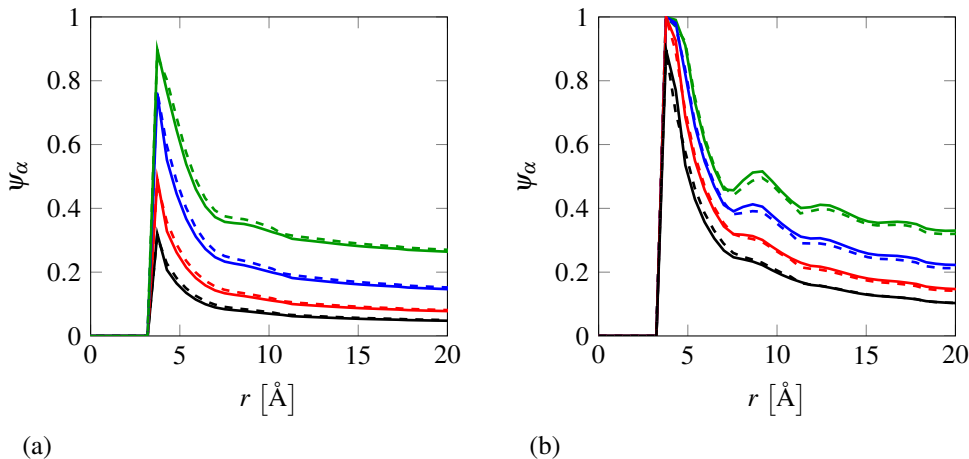


Figure 4.13: Fraction ϕ_α of monomer bonds at a distance r from the nanotube wall and at an angle $\theta < \alpha$ to the axis of (12,12) armchair (solid lines) and (21,0) zigzag (dashed lines) single-walled CNTs at (a) 800 and (b) 100 K. The angle α is equal to 2.5° (black lines), 5° (red lines), 10° (blue lines) and 20° (green lines).

that higher glass-transition temperature T_g does not lead to higher ordering in the polymer. The estimated values of T_g depend on the number of CNT-polymer interactions, while the ordering of the polymer chains depends on their possibility to maintain the monomers in close contact with the nanotube atoms.

Chirality effects The effects induced by the nanotube chirality, on the contrary, were negligible, with the results obtained for armchair and zigzag single-walled CNTs with similar diameter showing only minor differences. Hence, our findings suggest that the orientation of the periodic atomic structure of the nanotube along its longitudinal axis influences neither the density profile nor the ordering of the highly ordered polymer layer.

The relevance of our results has to be considered in the light of the characterization and design of CNT-polymer materials. Structural changes induced by nanotubes embedded in a polymer matrix might have interesting implications for physical and mechanical properties of the composite. More specifically, as the ordering of the polymer chains around the nanotube increases with its diameter, the role of size effects on the macroscopic mechanical properties of CNT-polymer composites might be significant.

Although a direct and quantitative comparison between the proposed MD model and real CNT-polymer composites was difficult and beyond the scope of this work, the obtained results were meaningful. Indeed, despite the simplicity of the atomistic representation employed for the polymer chains and the composite, the results are in good agreement with experimental and modeling literature findings that show nucleation of a crystallized or highly ordered polymer layer around the nanotube surface.

Bibliography

- [1] K. A. Anand, U. S. Agarwal, and R. Joseph. Carbon nanotubes induced crystallization of poly (ethylene terephthalate). *Polymer*, 47(11):3976–3980, 2006.
- [2] M. Asai, M. Shibayama, and Y. Koike. Common origin of dynamics heterogeneity and cooperatively rearranging region in polymer melts. *Macromolecules*, 44(16):6615–6624, 2011.
- [3] E. Assouline, A. Lustiger, A. H. Barber, C. A. Cooper, E. Klein, E. Wachtel, and H. D. Wagner. Nucleation ability of multiwall carbon nanotubes in polypropylene composites. *Journal of Polymer Science Part B: Polymer Physics*, 41(5):520–527, 2003.
- [4] A. H. Barber, S. R. Cohen, and H. D. Wagner. Measurement of carbon nanotube-polymer interfacial strength. *Applied Physics Letters*, 82(23):4140–4142, 2003.
- [5] J. Baschnagel and F. Varnik. Computer simulations of supercooled polymer melts in the bulk and in confined geometry. *Journal of Physics: Condensed Matter*, 17(32):R851, 2005.
- [6] C. Batistakis, M. A. J. Michels, and A. V. Lyulin. Confinement-induced stiffening of thin elastomer films: Linear and nonlinear mechanics vs local dynamics. *Macromolecules*, 47(14):4690–4703, 2014.
- [7] T. Belytschko, S. P. Xiao, G. C. Schatz, and R. S. Ruoff. Atomistic simulations of nanotube fracture. *Physical Review B*, 65(23):235430, 2002.
- [8] A. R. Bhattacharyya, T. V. Sreekumar, T. Liu, S. Kumar, L. M. Ericson, R. H. Hauge, and R. E. Smalley. Crystallization and orientation studies in polypropylene/single wall carbon nanotube composite. *Polymer*, 44(8):2373–2377, 2003.
- [9] R. H. Boyd, R. H. Gee, J. Han, and Y. Jin. Conformational dynamics in bulk polyethylene: A molecular dynamics simulation study. *The Journal of chemical physics*, 101(1):788–797, 1994.
- [10] J. Brandrup and E. H. Immergut. *Polymer Handbook*. John Wiley & Sons, Chichester, third edition, 1989.
- [11] D. W. Brenner. Empirical potential for hydrocarbons for use in simulating the chemical vapor deposition of diamond films. *Physical Review B*, 42(15):9458, 1990.
- [12] D. Brown, V. Marcadon, P. Mele, and N. D. Alberola. Effect of filler particle size on the properties of model nanocomposites. *Macromolecules*, 41(4):1499–1511, 2008.
- [13] J. Buchholz, W. Paul, F. Varnik, and K. Binder. Cooling rate dependence of the glass transition temperature of polymer melts: Molecular dynamics study. *The Journal of Chemical Physics*, 117(15):7364–7372, 2002.
- [14] M. Cadek, J. N. Coleman, V. Barron, K. Hedicke, and W. J. Blau. Morphological and mechanical properties of carbon-nanotube-reinforced semicrystalline and amorphous polymer composites. *Applied Physics Letters*, 81(27):5123–5125, 2002.

- [15] T. Chatterjee, C. A. Mitchell, V. G. Hadjiev, and R. Krishnamoorti. Hierarchical polymer-nanotube composites. *Advanced Materials*, 19(22):3850–3853, 2007.
- [16] T. Chatterjee, A. T. Lorenzo, and R. Krishnamoorti. Poly (ethylene oxide) crystallization in single walled carbon nanotube based nanocomposites: Kinetics and structural consequences. *Polymer*, 52(21):4938–4946, 2011.
- [17] E.-C. Chen and T.-M. Wu. Isothermal crystallization kinetics and thermal behavior of poly (ϵ -caprolactone)/multi-walled carbon nanotube composites. *Polymer Degradation and Stability*, 92(6):1009–1015, 2007.
- [18] J. N. Coleman, M. Cadek, K. P. Ryan, A. Fonseca, J. B. Nagy, W. J. Blau, and M. S. Ferreira. Reinforcement of polymers with carbon nanotubes. The role of an ordered polymer interfacial region. Experiment and modeling. *Polymer*, 47(26):8556–8561, 2006.
- [19] D. M. Dean, L. Rebenfeld, R. A. Register, and B. S. Hsiao. Matrix molecular orientation in fiber-reinforced polypropylene composites. *Journal of Materials Science*, 33(19):4797–4812, 1998.
- [20] M. S. Dresselhaus, G. Dresselhaus, P. C. Eklund, and A. M. Rao. Carbon nanotubes. In W. Andreoni, editor, *The Physics of Fullerene-Based and Fullerene-Related Materials*, pages 331–379. Springer, Dordrecht, 2000.
- [21] S. G. Falkovich, S. V. Larin, A. V. Lyulin, V. E. Yudin, J. M. Kenny, and S. V. Lyulin. Influence of the carbon nanofiller surface curvature on the initiation of crystallization in thermoplastic polymers. *RSC Advances*, 4(89):48606–48612, 2014.
- [22] R. H. Gee and R. H. Boyd. The role of the torsional potential in relaxation dynamics: A molecular dynamics study of polyethylene. *Computational and Theoretical Polymer Science*, 8(1):93–98, 1998.
- [23] H. Z. Geng, R. Rosen, B. Zheng, H. Shimoda, L. Fleming, J. Liu, and O. Zhou. Fabrication and properties of composites of poly(ethylene oxide) and functionalized carbon nanotubes. *Advanced Materials*, 14(19):1387–1390, 2002.
- [24] G. Gkikas, N.-M. Barkoula, and A. S. Paipetis. Effect of dispersion conditions on the thermo-mechanical and toughness properties of multi walled carbon nanotubes-reinforced epoxy. *Composites Part B: Engineering*, 43(6):2697–2705, 2012.
- [25] H. W. Goh, S. H. Goh, G. Q. Xu, K. P. Pramoda, and W. D. Zhang. Crystallization and dynamic mechanical behavior of double-C 60-end-capped poly (ethylene oxide)/multi-walled carbon nanotube composites. *Chemical Physics Letters*, 379(3):236–241, 2003.
- [26] B. P. Grady, F. Pompeo, R. L. Shambaugh, and D. E. Resasco. Nucleation of polypropylene crystallization by single-walled carbon nanotubes. *The Journal of Physical Chemistry B*, 106(23):5852–5858, 2002.

- [27] B. P. Grady, A. Paul, J. E. Peters, and W. T. Ford. Glass transition behavior of single-walled carbon nanotube-polystyrene composites. *Macromolecules*, 42(16):6152–6158, 2009.
- [28] R. Haggemueller, J. E. Fischer, and K. I. Winey. Single wall carbon nanotube/polyethylene nanocomposites: Nucleating and templating polyethylene crystallites. *Macromolecules*, 39(8):2964–2971, 2006.
- [29] J. Han, R. H. Gee, and R. H. Boyd. Glass transition temperatures of polymers from molecular dynamics simulations. *Macromolecules*, 27(26):7781–7784, 1994.
- [30] M. Hegde, U. Lafont, B. Norder, S. J. Picken, E. T. Samulski, M. Rubinstein, and T. Dingemans. SWCNT induced crystallization in an amorphous all-aromatic poly(ether imide). *Macromolecules*, 46(4):1492–1503, 2013.
- [31] M. Hegde, U. Lafont, B. Norder, E. T. Samulski, M. Rubinstein, and T. J. Dingemans. SWCNT induced crystallization in amorphous and semi-crystalline poly(etherimide)s: Morphology and thermo-mechanical properties. *Polymer*, 55(16):3746–3757, 2014.
- [32] M. Hegde, E. T. Samulski, M. Rubinstein, and T. J. Dingemans. The role of crystallinity in SWCNT-polyetherimide nanocomposites. *Composites Science and Technology*, 110:176–187, 2015.
- [33] Y. Huang, J. Wu, and K.-C. Hwang. Thickness of graphene and single-wall carbon nanotubes. *Physical Review B*, 74(24):245413, 2006.
- [34] K. Kremer and G. S. Grest. Dynamics of entangled linear polymer melts: A molecular-dynamics simulation. *The Journal of Chemical Physics*, 92(8):5057–5086, 1990.
- [35] E. D. Laird and C. Y. Li. Structure and morphology control in crystalline polymer-carbon nanotube nanocomposites. *Macromolecules*, 46(8):2877–2891, 2013.
- [36] S. V. Larin, S. G. Falkovich, V. M. Nazarychev, A. A. Gurtovenko, A. V. Lyulin, and S. V. Lyulin. Molecular-dynamics simulation of polyimide matrix pre-crystallization near the surface of a single-walled carbon nanotube. *RSC Advances*, 4(2):830–844, 2014.
- [37] N. Levi, R. Czerw, S. Xing, P. Iyer, and D. L. Carroll. Properties of polyvinylidene difluoride-carbon nanotube blends. *Nano Letters*, 4(7):1267–1271, 2004.
- [38] L. Li, C. Y. Li, and C. Ni. Polymer crystallization-driven, periodic patterning on carbon nanotubes. *Journal of the American Chemical Society*, 128(5):1692–1699, 2006.
- [39] L. Li, Y. Yang, G. Yang, X. Chen, B. S. Hsiao, B. Chu, J. E. Spanier, and C. Y. Li. Patterning polyethylene oligomers on carbon nanotubes using physical vapor deposition. *Nano Letters*, 6(5):1007–1012, 2006.
- [40] L. Li, B. Li, M. A. Hood, and C. Y. Li. Carbon nanotube induced polymer crystallization: The formation of nanohybrid shish-kebabs. *Polymer*, 50(4):953–965, 2009.

- [41] G. D. Liang and S. C. Tjong. Electrical properties of low-density polyethylene/multiwalled carbon nanotube nanocomposites. *Materials chemistry and physics*, 100(1):132–137, 2006.
- [42] X.-Q. Liu, W. Yang, B.-H. Xie, and M.-B. Yang. Influence of multiwall carbon nanotubes on the morphology, melting, crystallization and mechanical properties of polyamide 6/acrylonitrile-butadiene-styrene blends. *Materials & Design*, 34:355–362, 2012.
- [43] E. Logakis, C. Pandis, P. Pissis, J. Pionteck, and P. Pötschke. Highly conducting poly(methyl methacrylate)/carbon nanotubes composites: Investigation on their thermal, dynamic-mechanical, electrical and dielectric properties. *Composites Science and Technology*, 71(6):854–862, 2011.
- [44] M. Malagù, E. Benvenuti, and A. Simone. One-dimensional nonlocal elasticity for tensile single-walled carbon nanotubes: A molecular structural mechanics characterization. *European Journal of Mechanics-A/Solids*, 54:160–170, 2015.
- [45] K. F. Mansfield and D. N. Theodorou. Molecular dynamics simulation of a glassy polymer surface. *Macromolecules*, 24(23):6283–6294, 1991.
- [46] L. Martínez, R. Andrade, E. G. Birgin, and J. M. Martínez. PACKMOL: A package for building initial configurations for molecular dynamics simulations. *Journal of Computational Chemistry*, 30(13):2157–2164, 2009.
- [47] A. Minoia, L. Chen, D. Beljonne, and R. Lazzaroni. Molecular modeling study of the structure and stability of polymer/carbon nanotube interfaces. *Polymer*, 53(24):5480–5490, 2012.
- [48] M. L. Minus, H. G. Chae, and S. Kumar. Single wall carbon nanotube templated oriented crystallization of poly (vinyl alcohol). *Polymer*, 47(11):3705–3710, 2006.
- [49] N. Ning, W. Zhang, J. Yan, F. Xu, C. Tang, and Q. Fu. Effect of surface “groove” structure of carbon nanotube bundles on the formation of nanohybrid shish kebab. *Journal of Materials Research*, 27(21):2812–2818, 2012.
- [50] S. Plimpton. Fast parallel algorithms for short-range molecular dynamics. *Journal of Computational Physics*, 117(1):1–19, 1995.
- [51] J. Rottler and M. O. Robbins. Shear yielding of amorphous glassy solids: Effect of temperature and strain rate. *Physical Review E*, 68(1):011507, 2003.
- [52] J. Shen, W. Huang, L. Wu, Y. Hu, and M. Ye. The reinforcement role of different amino-functionalized multi-walled carbon nanotubes in epoxy nanocomposites. *Composites Science and Technology*, 67(15):3041–3050, 2007.
- [53] F. W. Starr, T. B. Schröder, and S. C. Glotzer. Molecular dynamics simulation of a polymer melt with a nanoscopic particle. *Macromolecules*, 35(11):4481–4492, 2002.

- [54] T. Sterzyński, J. Tomaszewska, K. Piszczek, and K. Skórczewska. The influence of carbon nanotubes on the PVC glass transition temperature. *Composites Science and Technology*, 70(6):966–969, 2010.
- [55] H. Uehara, K. Kato, M. Kakiage, T. Yamanobe, and T. Komoto. Single-walled carbon nanotube nucleated solution-crystallization of polyethylene. *The Journal of Physical Chemistry C*, 111(51):18950–18957, 2007.
- [56] C. Wei. Radius and chirality dependent conformation of polymer molecule at nanotube interface. *Nano Letters*, 6(8):1627–1631, 2006.
- [57] C. Wei, D. Srivastava, and K. Cho. Thermal expansion and diffusion coefficients of carbon nanotube-polymer composites. *Nano Letters*, 2(6):647–650, 2002.
- [58] S. Yu, W. Zheng, W. Yu, Y. Zhang, Q. Jiang, and Z. Zhao. Formation mechanism of β -phase in PVDF/CNT composite prepared by the sonication method. *Macromolecules*, 42(22):8870–8874, 2009.
- [59] V. E. Yudin, V. M. Svetlichnyi, A. N. Shumakov, D. G. Letenko, A. Y. Feldman, and G. Marom. The nucleating effect of carbon nanotubes on crystallinity in R-BAPB-type thermoplastic polyimide. *Macromolecular Rapid Communications*, 26(11):885–888, 2005.
- [60] F. Zhang, H. Zhang, Z. Zhang, Z. Chen, and Q. Xu. Modification of carbon nanotubes: Water-soluble polymers nanocrystal wrapping to periodic patterning with assistance of supercritical CO_2 . *Macromolecules*, 41(12):4519–4523, 2008.
- [61] L. Zhang, T. Tao, and C. Li. Formation of polymer/carbon nanotubes nano-hybrid shish-kebab via non-isothermal crystallization. *Polymer*, 50(15):3835–3840, 2009.
- [62] Q. Zhang, D. R. Lippits, and S. Rastogi. Dispersion and rheological aspects of SWNTs in ultrahigh molecular weight polyethylene. *Macromolecules*, 39(2):658–666, 2006.
- [63] Q. Zhang, S. Rastogi, D. Chen, D. Lippits, and P. J. Lemstra. Low percolation threshold in single-walled carbon nanotube/high density polyethylene composites prepared by melt processing technique. *Carbon*, 44(4):778–785, 2006.
- [64] Z. Q. Zhang, D. K. Ward, Y. Xue, H. W. Zhang, and M. F. Horstemeyer. Interfacial characteristics of carbon nanotube-polyethylene composites using molecular dynamics simulations. *ISRN Materials Science*, 2011:1–10, 2011.

Chapter 5

Diameter dependent elastic properties of carbon nanotube-polymer composites: Emergence of size effects from atomistic-scale simulations*

We propose a computational procedure to assess size effects in nonfunctionalized single-walled carbon nanotube (CNT)-polymer composites. The procedure upscales results obtained with atomistic simulations on a composite unit cell with one CNT to an equivalent continuum composite model with a large number of CNTs. Molecular dynamics simulations demonstrate the formation of an ordered layer of polymer matrix surrounding the nanotube. This layer, known as the interphase, plays a central role in the overall mechanical response of the composite. Due to poor load transfer from the matrix to the CNT, the reinforcement effect attributed to the CNT is negligible; hence the interphase is regarded as the only reinforcement phase in the composite. Then, the elastic properties of a one-dimensional equivalent fiber are identified through an optimization procedure based on the comparison between results from atomistic simulations and those obtained from an isogeometric analysis. Finally, the embedded reinforcement method is employed to determine the elastic properties of a representative volume element of a composite with various fiber volume fractions and distributions. We then investigate the role of the CNT diameter on the elastic response of a CNT-polymer composite; our simulations predict a size effect on the composite elastic properties, clearly related to the interphase volume fraction.

5.1 Introduction

The diameter of carbon nanotubes (CNTs) can induce size effects in the structural and mechanical properties of CNT-polymer composites [6, 7, 14, 16, 20, 49, 84]. Due to the high aspect ratio of CNTs, these size effects can only be assessed using computational multi-scale procedures. To this end, we present a computational procedure to upscale nanoscale information, obtained with atomistic simulations, to a continuum micromechanical model at the composite scale for the analysis of the size-dependent elastic properties of a nonfunctionalized single-walled CNT-polymer composite. In the following, the term “continuum”

**Reproduced from:* M. Malagù, M. Goudarzi, A. Lyulin, E. Benvenuti and A. Simone, Diameter dependent elastic properties of carbon nanotube-polymer composites: Emergence of size effects from atomistic-scale simulations, *submitted*.

indicates a volume where a continuous distribution of material replaces the atomistic structure.

Diameter-induced effects were first noticed by means of pull-out tests that showed a decrease of the interfacial shear strength between a CNT and the polymer matrix around it with increasing nanotube diameter [7, 14]. Although a limited number of experimental results is available [7, 14], the observed trend for the interfacial shear strength has been confirmed by means of atomistic simulations [20, 49, 80]. This size effect was attributed to the increasing number of non-bonded interactions between polymer and CNT atoms with decreasing nanotube diameter [84]. It is however recognized that another phase in CNT-polymer composites contributes to the overall mechanical response beside the CNT-polymer interface.

Several works (see Reference [45] for an extensive review) indicate that the formation of an ordered layer of polymer matrix around a nanotube is relevant for the enhancement of the mechanical properties of the composite. Such a layer, usually referred to as the interphase, has been identified in a wide class of CNT-polymer composites [45]. In particular, Coleman and coworkers [18, 65] suggested that the reinforcement observed in CNT-polyvinyl alcohol composites was mainly provided by the interphase while the load transfer from the matrix to the CNT was poor. Similar results, emphasizing the reinforcement effect of the interphase and the weakness of the interface in nonfunctionalized CNT-polymer composites have been experimentally observed with various polymer matrices [3, 27, 35, 67, 76, 77].

The characterization of the interphase is usually performed with computer simulations since they enable a detailed analysis of the polymer chain structure. Using molecular dynamics (MD) simulations, Falkovich et al. [26] showed that the ordering of the interphase in CNT-polyimide composites increases with the nanotube diameter. Similar results were also achieved with a generic amorphous polymer model [52]. The mechanical properties of the interphase are typically assessed through a continuum model that is mechanically equivalent to an atomistic reference model [15, 56, 82, 83]. In an alternative approach, proposed by Choi et al. [16], the stiffness of the interphase in CNT-epoxy composites is studied through a reverse engineering procedure by comparing the elastic response of the MD system with that of an intermediate continuum micromechanical model. Results showed that the interphase stiffness increases by decreasing the CNT diameter. However, their atomistic model considered periodic infinitely long nanotubes. Consequently, once the simulation cell is loaded in tension along the CNT axis direction, matrix and nanotube are equally stretched while in reality the CNT should deform according to the stresses transferred to it from the matrix through the interface.

The multiscale procedure employed in this contribution for the characterization of size effects in the elastic properties of the CNT-polymer composites is summarized in Figure 5.1. As proposed in previous works [15, 16, 56, 82], we employed a) atomistic simulations to investigate structural and mechanical features of CNT-polymer composites at the nanoscale, b) an intermediate continuum micromechanical model to estimate the mechanical properties of the reinforcement phase, and c) a continuum micromechanical model to assess the macroscopic elastic moduli of the composite.

As shown in Figure 5.1a, the atomistic models consider a short uncapped nonfunctionalized single-walled CNT of finite length fully embedded into the simulation box. This setup enables load transfer from a coarse-grained amorphous monodisperse polyethylene-

like polymer matrix [52] to the nanotube. Rather than characterizing size effects for a specific composite, we aim to explore the influence of the CNT diameter for a wider range of polymer matrices using a simple yet representative model for the polymer chains. CNT-polymer composites with nanotubes of different diameter are generated in the molecular dynamics setting described in Section 5.2.1. The equilibrated configurations are examined in Section 5.2.2 to characterize the geometry of CNT, interface, interphase and bulk polymer matrix. The roles of these four phases in the elastic response of the composite are explored through uniaxial tensile tests performed with molecular mechanics (MM) in Section 5.2.3. At the same time, MM uniaxial tensile tests are also performed on a pure polymer matrix to calculate the elastic properties of the polymer. As discussed in Section 5.2.4, and observed in the literature [3, 18, 27, 35, 65, 67, 76, 77] for real CNT-polymer composites, the interphase is the true reinforcement phase in the composite while the effect of the embedded CNT on the elastic response of the composite is negligible due to the weak interface interaction (Sections 5.2.3 and 5.2.4). To take into account the effect of the interphase in a computationally feasible manner at the composite level with a realistic number of CNTs, we have defined an equivalent fiber. The approach consists in the definition of an intermediate continuum micromechanical model that, as shown in Figure 5.1b, contains the bulk polymer and a three-dimensional domain, referred to as equivalent fiber, whose geometry coincides with that of the interphase derived in Section 5.2.2 in the atomistic model. The elastic properties of the equivalent fiber are determined through a parameter estimation procedure by comparing the mechanical response of the one-fiber composite obtained with the atomistic and the isogeometric analysis in Section 5.3.

With the interphase and bulk polymer mechanical properties at hand, a micromechanical analysis of the CNT-polymer composite shown in Figure 5.1c is conducted. Elastic properties of several representative volume elements (RVEs) with unidirectional and randomly oriented CNTs are derived by means of FEM simulations (see Section 5.4) to assess diameter effects at different nanotube volume ratios. Akin to the intermediate continuum model in Figure 5.1b, only the bulk polymer and equivalent continuum fibers (the interphases) are considered. Due to the high aspect ratio of real nanotubes and to their large number in an RVE, each equivalent continuum three-dimensional fiber is modeled as a one-dimensional fiber by means of the embedded reinforcement method [59] described in Section 5.4.1. The results of the FEM analyses are finally compared with those obtained with classical micromechanical models in Section 5.5.

The proposed computational procedure is not only intended for the assessment of size effects. It also provides a strategy to understand the role played by the different phases in the composite, a relevant question about CNT-polymer composites and other nanocomposite materials [62, 78]. Despite the approximations of the polymer model at the atomistic level, the results of our simulations are qualitatively comparable with literature findings using real polymers as discussed in Section 5.6.

The standard notation (n, m) to describe single-walled CNTs [23] is adopted throughout the paper. Moreover, the notation (n, m) -polymer is used to denote a polymer matrix reinforced with (n, m) single-walled CNTs.

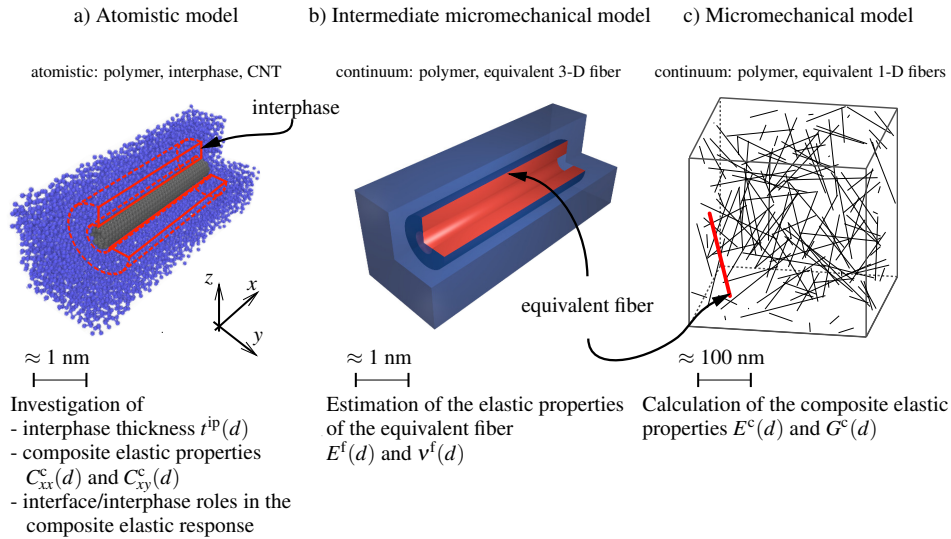


Figure 5.1: Objectives of the multiscale procedure for the characterization of size effects induced by the nanotube diameter d on the CNT-polymer composite elastic properties. In the intermediate micromechanical model and the micromechanical model, only the bulk polymer matrix and the interphase have been considered since the contributions of the nanotube and the interface on the elastic response of the composite are negligible.

5.2 Atomistic modeling of CNT-polymer composites

Atomistic simulations of representative CNT-polymer composites are performed to characterize the nanoscale features required to establish the intermediate continuum model in Section 5.3. To this end, four composites embedding uncapped nanotubes of different diameter are generated through MD simulations as detailed in Section 5.2.1. Here, we considered CNT-polymer composites with the same nanotube volume fraction to explore the effects induced by the CNT diameter. In particular, the effect on the interphase volume fraction and the elastic properties of the CNT-polymer composites are investigated (see Sections 5.2.2 and 5.2.3, respectively). Furthermore, based on the results obtained from MM uniaxial tensile tests, the roles of the CNT and the interphase in the mechanical response of the composite are discussed in Section 5.2.4.

5.2.1 Method

The atomistic model for the CNT-polymer composite is identical to that used in Reference [52]. Fully-atomistic uncapped nonfunctionalized single-walled CNTs are modeled with the modified Morse potential [8, 51, 74] while the amorphous monodisperse polyethylene-like polymer is modeled with the coarse-grained Finite Extensible Nonlinear Elastic (FENE) potential [43]. This allows for the analysis of CNT diameter-induced effects as well. Polymer chemistry-specific effects are therefore avoided to explore the influence of the nanotube

in a wide range of single-walled CNT-polymer composite.

The polymer matrix is modeled as a coarse-grained amorphous monodisperse polyethylene-like system. Each polymer chain is defined by 300 identical monomeric units (referred to as beads) covalently bonded through the FENE interatomic potential

$$U(r) = -0.5KR_0^2 \ln \left[1 - \left(\frac{r}{R_0} \right)^2 \right] + 4\epsilon_p \left[\left(\frac{\sigma_p}{r} \right)^{12} - \left(\frac{\sigma_p}{r} \right)^6 + \frac{1}{4} \right], \quad (5.1)$$

where r is the distance between two beads. The constants K and R_0 are the stiffness and the maximum elongation of the polymer bonds, while ϵ_p and σ_p are the beads characteristic length and energy constants. According to Kremer and Grest [43], for a monodisperse polyethylene-like polymer model system, $\epsilon_p = 5.1 \text{ \AA}$, $\sigma_p = 0.8903 \text{ kcal/mol}$, $K = 30\sigma_p/\epsilon_p^2$ and $R = 1.5\sigma_p$. The model employed for the nanotubes is detailed in Reference [8]. Between polymer beads and CNT atoms only non-bonded Lennard-Jones interactions defined by the potential

$$U(r) = 4\epsilon_{pc} \left[\left(\frac{\sigma_{pc}}{r} \right)^{12} - \left(\frac{\sigma_{pc}}{r} \right)^6 + \frac{1}{4} \right] \quad (5.2)$$

are allowed. The constants ϵ_{pc} and σ_{pc} are calculated with the Lorentz-Berthelot rules

$$\sigma_{pc} = \frac{1}{2} (\sigma_p + \sigma_c) \quad \text{and} \quad \epsilon_{pc} = \sqrt{\epsilon_p \epsilon_c}, \quad (5.3)$$

where σ_c and ϵ_c are the Lennard-Jones constants for single-walled CNT carbon atoms [11].

To explore diameter effects in CNT-polymer composites with the same nanotube volume fraction v^{CNT} , four different nanocomposites with $v^{\text{CNT}} \approx 0.6\%$ but with nanotubes of different diameter were generated. Since the variation of carbon nanotube weight fraction in the generated CNT-polymer composites is small [52], we can assume that the trend for the mechanical properties observed in the next sections is mainly caused by the changes in the nanotube diameter. Effects induced by the nanotube chirality are not investigated because assumed to be negligible: as observed by Malagù et al. [52], chirality does not influence the atomic structure at the CNT-polymer interphase that determines the mechanical properties of the composite (later explained in Section 5.3.2). Here, only armchair ((6,6), (8,8), (10,10) and (12,12)) single-walled CNTs are considered. As shown Figure 5.2a, the nanotubes, centered at $x = 0 \text{ \AA}$, are aligned along the x -axis. The length of the simulation box in the x -direction ($L_x \approx 180 \text{ \AA}$) is larger than that of the nanotubes ($l \approx 100 \text{ \AA}$). This allows for the assessment of the interface properties and the load transfer mechanism between polymer matrix and CNT. The dimension of the unit cell in the y - and z direction (L_y and L_z , respectively) is such that the interphase region is completely embedded in the simulation box, hence to avoid any contact or intersection of the interphase with its periodic image. To fully assess the nanotube reinforcement effects, a pure polymer matrix was also generated.

Seeking for the elastic properties under quasi-static deformation through molecular mechanics (MM), CNT-polymer composite and pure polymer matrix systems are investigated in glassy state where the vibrational part of the free energy is negligible [36, 70]. Therefore, all simulations have been performed on atomistic configurations below the glass transition temperature ($T_g \approx 200 \text{ K}$ [52]), specifically at 100 K. For each system, three different initial configurations were generated and the corresponding results were averaged. The Large-scale Atomic/Molecular Massively Parallel Simulator (LAMMPS) software package was

used [61]. Newton's equations of motion were integrated with the velocity Verlet algorithm using a time step of 1 fs. The Nosé-Hoover thermostat and barostat were used. Energy minimization was performed with the conjugate gradient method. In all simulations, periodic boundary conditions in the three directions were applied. LAMMPS input scripts to generate the results discussed in the next sections are available for download at the authors' web-page.*

5.2.2 Single-walled CNT and interphase volume fractions

In this section, the geometry of the phases in the CNT-polymer composite, required for the development of the intermediate continuum micromechanical model in Section 5.3, is determined. The corresponding volume fractions are also provided since they play a significant role in the macroscopic elastic properties discussed in Section 5.4.

Figure 5.2b shows the cross section of an (8,8)-polymer composite and highlights the different phases characterizing single-walled CNT-polymer composites. Visual examination reveals four distinct regions. The first (in gray), with a cylindrical shape, represents the effective nanotube volume, also indicated as the *effective reinforcement* according to the model proposed by Pipes et al. [60, Figure 2] and adopted by many others [28, 32, 85]. Here, the nanotube and the empty region inside it are replaced by an effective solid cylinder. A nanotube is therefore considered as a solid beam of length l and circular cross section of diameter d with volume

$$V^{\text{CNT}} = \pi \frac{d^2}{4} l. \quad (5.4)$$

The diameter of the effective reinforcement related to an (n, m) single walled CNT is given in Reference [60]:

$$d = \frac{a_{\text{cc}} \sqrt{3(n^2 + m^2 + nm)}}{\pi} + t, \quad (5.5)$$

where $a_{\text{cc}} = 1.421 \text{ \AA}$ is the carbon-carbon bond length and $t = 3.42 \text{ \AA}$ is the separation distance of graphene sheets [38].

The second region (in green) is the interface. Its thickness t^{if} is defined as the average equilibrium distance between the CNT surface and the first layer of polymer atoms [60]. The thickness t^{if} can be determined from the analysis of the radial density profile $\rho(r)$, where r is the distance from the nanotube surface (i.e., at $t/2$ from the CNT atoms), obtained from atomistic simulations. Here, t^{if} has been assumed as the distance between the CNT surface ($r = 0 \text{ \AA}$) and the first peak in $\rho(r)$. As illustrated in Figure 5.3a, the interface thickness, insensitive to the nanotube diameter, is approximately equal to 4.5 \AA . This estimate is in line with literature results obtained from MD models of CNTs embedded in real polymers [17, 20, 31, 79]. Analogously, examination of the density profile along the axis of the CNT (i.e. in the x direction) provides the length of the interface. As shown in Figure 5.3b, the peaks in $\rho(r)$ quickly decay after the end of the nanotube (i.e. at $|x| \geq l/2$), and the interface length is assumed equal to that of the nanotube. Thus, the interface volume is calculated as

$$V^{\text{if}} = \pi \frac{(d + 2t^{\text{if}})^2 - d^2}{4} l. \quad (5.6)$$

*Note to Reviewer: These scripts will be available in due time.

The third region (in red) consists of the ordered layer of polymer matrix surrounding the nanotube, the interphase. Its thickness and length are derived by comparing the density profile in the CNT-polymer composite with that of the pure polymer matrix as previously done for real CNT-polymer composites in [47, 83]. Due to statistical noise in $\rho(r)$, it is difficult to provide a precise estimate of the interphase thickness t^{ip} . Nevertheless, as depicted in Figure 5.3a, for $r \geq 30.0 \text{ \AA}$ the oscillations in the density profiles for all CNT-polymer composites resemble those in the pure polymer matrix. Therefore, t^{ip} has been assumed 25.5 \AA irrespective of the nanotube diameter. The independence of the interphase thickness from the size of the inclusion was observed in atomistic models of CNTs embedded in real polymers [26, 36] and other nanocomposite systems [12, 30]. It is however worth mentioning that t^{ip} shows a temperature dependence as shown in [52, Figure 6]; in this work t^{ip} has been estimated at $T = 100 \text{ K}$. Figure 5.3b shows that the interphase length can be set equal to l , thus yielding the interphase volume

$$V^{\text{ip}} = \pi \frac{(d + 2t^{\text{if}} + 2t^{\text{ip}})^2 - (d + 2t^{\text{if}})^2}{4} l. \quad (5.7)$$

Figure 5.3a shows that nanotubes with bigger diameter lead to highest peaks in the interphase density profile. As thoroughly discussed in [26, 52], this indicates that the ordering of the interphase atomic structure increases with the diameter of the embedded CNT.

Finally, the fourth region (in blue) corresponds to the amorphous bulk polymer whose structure is not affected by the CNT. Knowing the volume of the MD unit cell V^{cell} (the dimensions of the CNT-polymer composite unit cell at this temperature are in Table 5.1), the volume of amorphous polymer is

$$V^{\text{bulk}} = V^{\text{cell}} - (V^{\text{CNT}} + V^{\text{if}} + V^{\text{ip}}). \quad (5.8)$$

composite	d	L_x	L_y	L_z
(6,6)-polymer	8.14	66.9	66.9	181.2
(8,8)-polymer	10.86	91.9	91.9	175.9
(10,10)-polymer	13.57	114.7	114.7	177.9
(12,12)-polymer	16.28	136.3	136.3	181.7

Table 5.1: Dimensions of the (n,n) -polymer composites at 100 K.

From the volume of the aforementioned regions, the corresponding volume fractions are easily calculated dividing (5.4)-(5.8) by V^{cell} . For the particular case of the nanotube and the interphase volume fractions we have

$$v^{\text{CNT}} = \frac{V^{\text{CNT}}}{V^{\text{cell}}} = \pi \frac{d^2 l}{4V^{\text{cell}}} \quad (5.9)$$

and

$$v^{\text{ip}} = \frac{V^{\text{ip}}}{V^{\text{cell}}} = v^{\text{CNT}} \frac{V^{\text{ip}}}{V^{\text{CNT}}} = v^{\text{CNT}} \frac{(4t^{\text{ip}})^2 + 4dt^{\text{ip}} + 8t^{\text{ip}}t^{\text{if}}}{d^2}, \quad (5.10)$$

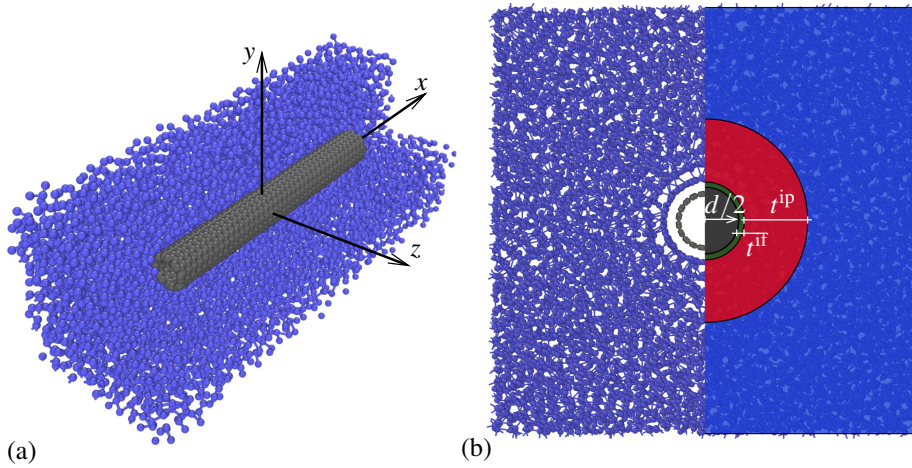


Figure 5.2: (a) Snapshot of the atomistic model of an (8,8)-polymer composite (monomer beads in blue, single-walled CNT carbon atoms in gray). Part of the polymer matrix has been removed to reveal the embedded nanotubes. (b) Cross sectional view of the (8,8)-polymer composite. On the right half of the image, colored regions denote the composite phases: CNT (gray), interface (green), interphase (red) and bulk matrix (blue). These figures have been adapted from Reference [52].

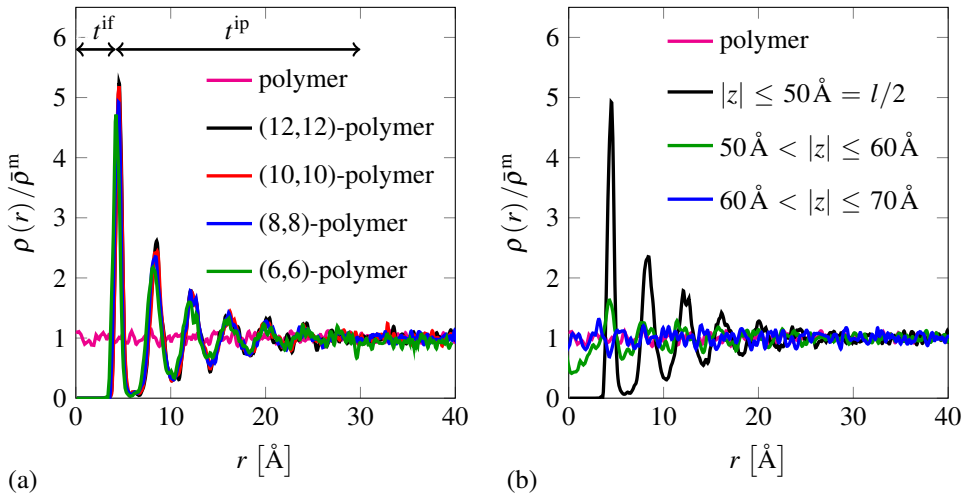


Figure 5.3: (a) Density profile in the polymer matrix and in (n,n) -polymer composites at 100 K as a function of the distance r from the nanotube surface. All curves have been normalized with respect to the average density of the polymer matrix $\bar{\rho}^m = 0.818 \text{ g/cm}^3$ (this figure is adapted from Reference [52]). (b) Density profile in the polymer matrix and in an (8,8)-polymer composite evaluated at different position along the longitudinal axis of the nanotube (i.e. x -axis).

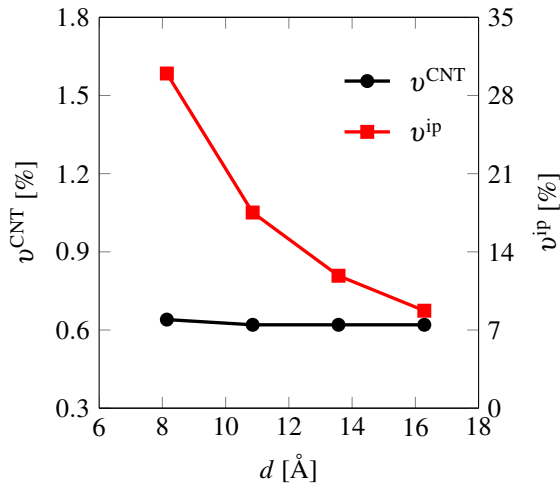


Figure 5.4: CNT volume fraction v^{CNT} and interphase volume fraction v^{ip} calculated with (5.9) and (5.7), respectively, for four different (n,n) -polymer composites.

respectively. As a direct consequence, Figure 5.4 shows that when composites with the same CNT volume fraction v^{CNT} but different CNT diameter are considered, the volume fraction of the interphase v^{ip} decreases with d . This result has a considerable impact on the composite mechanical properties discussed in Section 5.4. Moreover, as indicated in eq. (5.10), v^{ip} increases linearly with the CNT volume fraction as observed experimentally [18].

5.2.3 Uniaxial tensile test simulations

Mechanical properties of CNT-polymer composites under uniaxial quasi-static loading are determined with MM simulations. After each strain increment, consisting in a small uniaxial deformation applied in the direction of the nanotube axis (i.e., the x axis), the total potential energy of the system is minimized. More specifically, making use of the Voigt notation, the strain increment defined by the macrostrain tensor

$$\bar{\boldsymbol{\varepsilon}} = [\bar{\varepsilon}_{xx} \ 0 \ 0 \ 0 \ 0 \ 0]^T = [0.01\% \ 0 \ 0 \ 0 \ 0 \ 0]^T, \quad (5.11)$$

with the superscript T denoting transpose, is applied to the periodic unit cell (in (5.11) and throughout this work a bar above a symbol indicates a macroscopic quantity). Afterwards, the total potential energy of the system is minimized keeping the size of the box fixed [4, 46, 54]. This procedure is repeated until the total axial strain is equal to 5% since MM simulations on glassy polymers can be performed only under small deformation since the adopted interatomic potentials are not suitable to model the nonlinear response of the material.

The first significant insight concerning the deformation mechanism in CNT-polymer composite is provided by the analysis of the strain energy contributions during deformation. Here, the total strain energy Π^{total} is decomposed into the contribution of the CNT

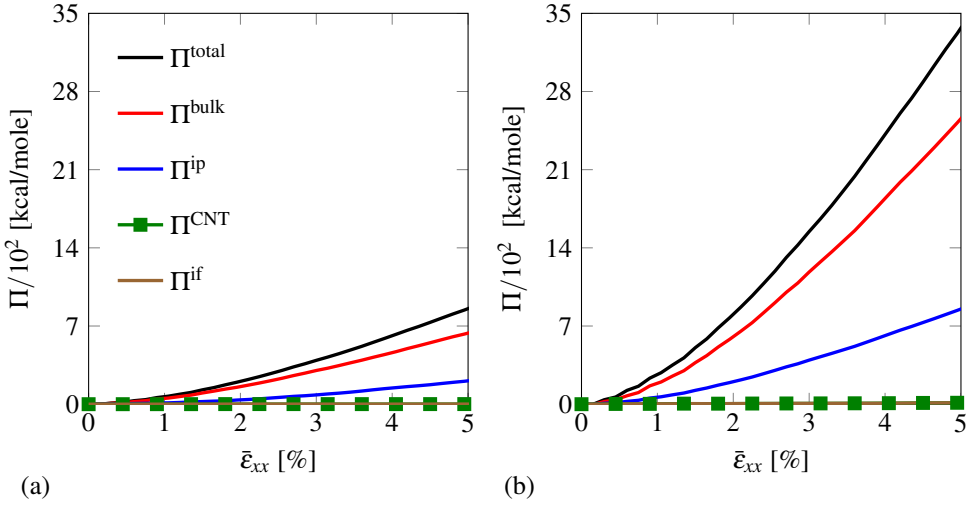


Figure 5.5: Analysis of the total strain energy Π^{total} and its separate contributions from CNT (Π^{CNT}), interface (Π^{if}), interphase (Π^{ip}) and bulk (Π^{bulk}) during uniaxial tension of two CNT-polymer composites with an (8,8) nanotube of length (a) 10 and (b) 40 nm.

	$\Pi^{\text{CNT}}/\Pi^{\text{total}}$ [%]	$\Pi^{\text{if}}/\Pi^{\text{total}}$ [%]	$\Pi^{\text{ip}}/\Pi^{\text{total}}$ [%]	$\Pi^{\text{bulk}}/\Pi^{\text{total}}$ [%]
$l = 10$ nm	1.55	1.40	24.15	72.60
$l = 40$ nm	1.15	1.14	24.90	72.81

Table 5.2: Normalized value of the strain energy contributions at $\bar{\epsilon}_{xx} = 5\%$.

(Π^{CNT}), the interface (Π^{if}), the interphase (Π^{ip}), and the bulk (Π^{bulk}). As shown in Figure 5.5a for an (8,8)-polymer composite, Π^{ip} and Π^{bulk} are the major contributions to Π^{total} while Π^{if} and Π^{CNT} are negligible. However, since in classical short fiber composites the reinforcement efficiency and, consequently, the axial strain in the fiber increases with its length, we repeated these measurements for a composite embedding an (8,8) CNT four times longer ($l = 40$ nm). Nevertheless, as shown in Figure 5.5b, the corresponding results are analogous to those obtained with the shorter nanotube (see Table 5.2 for a comparison of the strain energy contributions at $\bar{\epsilon}_{xx} = 5\%$). This indicates that, due to poor adhesion with the polymer matrix, negligible deformation occurs in the CNT. Thus, the mechanical response of the composite can be determined to a good approximation by just considering interphase and bulk polymer. An analogous conclusion has been reached by Coleman and coworkers [18, 65] in their experiments on real CNT-polymer composites.

The results obtained from the MM uniaxial tensile tests have been used to estimate the effect of the reinforcement induced by the inclusion of a nanotube into a polymer matrix. Since the nanotubes are aligned along the x -direction, the generated CNT-polymer compos-

ites are transversely isotropic and the elastic constitutive relations are expressed by

$$\begin{bmatrix} \bar{\sigma}_{xx} \\ \bar{\sigma}_{yy} \\ \bar{\sigma}_{zz} \\ \bar{\sigma}_{xy} \\ \bar{\sigma}_{xz} \\ \bar{\sigma}_{yz} \end{bmatrix} = \begin{bmatrix} C_{xx}^c & C_{xy}^c & C_{xy}^c & 0 & 0 & 0 \\ C_{xy}^c & C_{yy}^c & C_{yz}^c & 0 & 0 & 0 \\ C_{xy}^c & C_{yz}^c & C_{yy}^c & 0 & 0 & 0 \\ 0 & 0 & 0 & 2G_{xy}^c & 0 & 0 \\ 0 & 0 & 0 & 0 & 2G_{xy}^c & 0 \\ 0 & 0 & 0 & 0 & 0 & \frac{C_{yy}^c - C_{yz}^c}{2} \end{bmatrix} \begin{bmatrix} \bar{\epsilon}_{xx} \\ \bar{\epsilon}_{yy} \\ \bar{\epsilon}_{zz} \\ \bar{\epsilon}_{xy} \\ \bar{\epsilon}_{xz} \\ \bar{\epsilon}_{yz} \end{bmatrix}, \quad (5.12)$$

where C_{ij}^c and $\bar{\sigma}_{ij}$ are the components of the elasticity tensor and the macroscopic stress tensor in matrix form, respectively. The elasticity matrix \mathbf{C}^c in (5.12) is defined by five independent elastic constants. In this work, however, we will determine only C_{xx}^c and C_{xy}^c since, as shown in Section 5.3, the other components are not relevant for the mechanical characterization of the interphase. Substituting (5.11) into (5.12), we obtain

$$C_{xx}^c = \frac{\bar{\sigma}_{xx}}{\bar{\epsilon}_{xx}} \quad \text{and} \quad C_{xy}^c = \frac{\bar{\sigma}_{yy}}{\bar{\epsilon}_{xx}} = \frac{\bar{\sigma}_{zz}}{\bar{\epsilon}_{xx}}, \quad (5.13)$$

where $\bar{\sigma}_{xx}$, $\bar{\sigma}_{yy}$ and $\bar{\sigma}_{zz}$ were derived from the MM simulations.

Similarly, the elastic properties were determined for the pure polymer matrix. As expected, tensile tests in all three directions yielded an isotropic response. Its stress-strain relations is expressed as

$$\begin{bmatrix} \bar{\sigma}_{xx} \\ \bar{\sigma}_{yy} \\ \bar{\sigma}_{zz} \\ \bar{\sigma}_{xy} \\ \bar{\sigma}_{xz} \\ \bar{\sigma}_{yz} \end{bmatrix} = \begin{bmatrix} C_{xx}^m & C_{xy}^m & C_{xy}^m & 0 & 0 & 0 \\ C_{xy}^m & C_{xx}^m & C_{xy}^m & 0 & 0 & 0 \\ C_{xy}^m & C_{xy}^m & C_{xx}^m & 0 & 0 & 0 \\ 0 & 0 & 0 & \frac{C_{xx}^m - C_{xy}^m}{2} & 0 & 0 \\ 0 & 0 & 0 & 0 & \frac{C_{xx}^m - C_{xy}^m}{2} & 0 \\ 0 & 0 & 0 & 0 & 0 & \frac{C_{xx}^m - C_{xy}^m}{2} \end{bmatrix} \begin{bmatrix} \bar{\epsilon}_{xx} \\ \bar{\epsilon}_{yy} \\ \bar{\epsilon}_{zz} \\ \bar{\epsilon}_{xy} \\ \bar{\epsilon}_{xz} \\ \bar{\epsilon}_{yz} \end{bmatrix}, \quad (5.14)$$

where the superscript m identifies the elastic components of the polymer matrix. In particular, $C_{xx}^m = 5.14$ GPa and $C_{xy}^m = 2.90$ GPa. As shown in Figure 5.6, C_{xx}^c is always higher than C_{xx}^m while the opposite is observed comparing C_{xy}^c and C_{xy}^m . Therefore, as shown in previous works on real CNT-polymer composites [16, 36, 82], the presence of a CNT yields higher elastic constants in the axial direction compared to those of the pure polymer matrix.

5.2.4 Interface versus interphase

Results from MM suggested that the reinforcement in the nonfunctionalized CNT-polymer composites is merely determined by the interphase. The role of the nanotube, due to the weak interface interactions, is limited to the nucleation of the interphase layer.

Although there is no consensus [62] about the reinforcement offered by the CNT through the interactions at the interface and the interphase, some experimental results on nonfunctionalized CNT-polymer composites support our findings. For instance, Coleman and coworkers [18, 65] associated the reinforcement in CNT-polyvinyl alcohol composites to the formation of an ordered polymer layer around the nanotubes. Fitting their experimental results

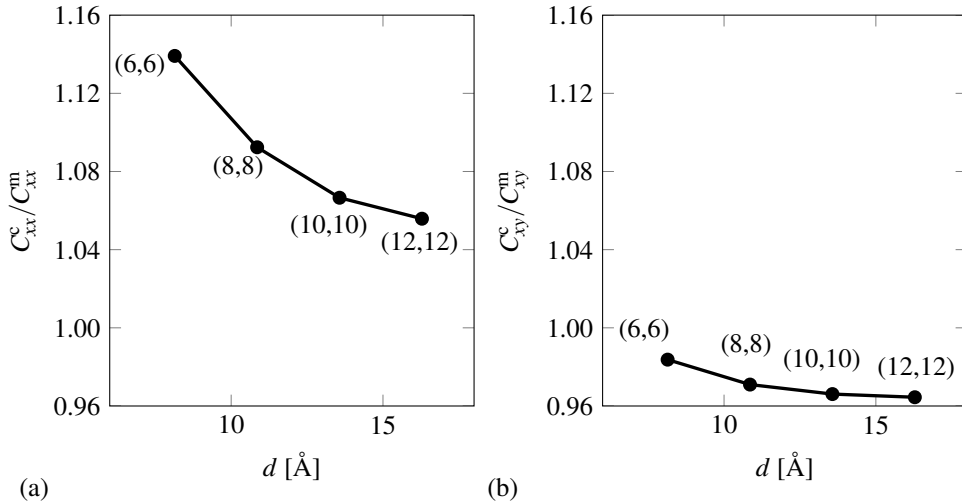


Figure 5.6: Normalized elastic components (a) C_{xx}^c and (b) C_{xy}^c of four (n,n) -polymer composites. The results have been normalized with respect to the elastic components of the polymer matrix $C_{xx}^m = 5.14$ GPa and $C_{xy}^m = 2.90$ GPa.

with micromechanical models, the authors deduced that the stress transfer between nanotubes and polymer matrix was poor. Hegde et al. [35], comparing results from different amorphous polymer matrix reinforced with CNTs, found that the elastic properties of the composite increase only when nanotubes nucleate crystallization. Watts and Hsu [77] investigated the strength of the interface through examination of the surface fracture in an MPC-DEA polymer matrix reinforced with CNTs. TEM images at the crack surface showed that the surface of the pulled-out nanotubes was clean (i.e. no polymer particles were attached to them) denoting poor adhesion between CNTs and matrix. Similar results were also reported for CNTs embedded in polystyrene [27] and epoxy [3, 67] matrices. Using Raman spectroscopy, Wang et al. [76] suggested that the variation in the Young's modulus of CNT-epoxy composites induced by different degrees and types of functionalization groups on the nanotubes surface was caused by changes of the interfacial molecular structure.

However, it is worth mentioning that other authors reported strong bond between polymer matrix and nonfunctionalized nanotubes. Qian and coworkers [63, 64] observed fractured nanotubes at the crack surface in CNT-polystyrene composites suggesting a good load transfer between CNTs and polymer matrix. By using pull-out tests, good adhesion was also reported in CNT-epoxy composites [19] and CNT-polyethylene butane composites [7]. However, in these cases the pull-out force was not always parallel to the nanotube axis. Thus, the possible sliding of the embedded part of the nanotube along the interface surface during pull-out might have induced an overestimation of the interfacial properties [77]. Moreover, the elastic mechanical properties of the interface were not compared to those of the interphase.

Therefore, we limit the present study to nonfunctionalized CNT-polymer composites where the CNT-matrix adhesion is poor and CNTs nucleate a highly ordered region of polymer matrix. At the same time, this study allows for the assessment of the effect of the

interphase on the composite elastic properties.

5.2.5 Size effect

As shown in Figure 5.6, the component C_{xx} of the elasticity tensor, characterizing the stiffness of the composite in the axial direction, decreases by increasing the nanotube diameter. A similar trend was observed with atomistic simulations of CNTs embedded in polypropylene [82], polyvinyl chloride [36] and EPON 862[®] epoxy resin [16]. Here, the size effect is solely determined by the interphase as the only component of the CNT-polymer composites having a reinforcement effect. In particular, the variation of C_{xx}^c and C_{xy}^c with respect to the CNT diameter d can be motivated by the trend of the interphase volume fraction v^{ip} with respect to d (this will be discussed in further details in Section 5.3). As shown in Figures 5.3-5.4, by increasing the diameter d , despite the increased ordering of the interphase atomic structure, the volume fraction of the interphase (i.e. the reinforcement phase) decreases and, consequently, also the stiffness of the composite in the x -direction: the lower the interphase volume fraction, the weaker the reinforcement.

5.3 Interphase as an equivalent continuum 3-D fiber

In this section we define a continuum model that is mechanically equivalent to the discrete atomistic model shown earlier. This allows the estimation of the elastic properties of the interphase, here modeled through an equivalent 3-D fiber, that are required for the micromechanical modeling of the nonfunctionalized CNT-polymer composites in Section 5.4. Moreover, CNT diameter-induced size effects on the elastic properties of the interphase are discussed in Section 5.3.2.

The previous MM simulations showed that only the interphase provides reinforcement. Due to weak non-bonded interactions, the contribution of the CNT is negligible. Therefore, as shown in Figure 5.1b, the proposed intermediate continuum micromechanical model consists only of the bulk polymer, assumed as homogeneous, and an equivalent continuum 3-D fiber (representing the interphase region) with homogeneous properties while interface and CNT are not taken into account.

The Young's modulus E^m and the Poisson's ratio ν^m of the bulk polymer matrix are derived from the estimated C_{xx}^m and C_{xy}^m . Since the matrix is isotropic, following Milton [53],

$$E^m = \frac{C_{xx}^m C_{xx}^m + C_{xx}^m C_{xy}^m - 2C_{xy}^m C_{xy}^m}{C_{xx}^m + C_{xy}^m} \quad \text{and} \quad \nu^m = \frac{C_{xy}^m}{C_{xx}^m + C_{xy}^m}. \quad (5.15)$$

Accordingly, E^m and ν^m resulted equal to 3.04 GPa and 0.36, respectively, values in the typical range for glassy polymers [10].

As illustrated in Figure 5.1b, the interphase is modeled by an equivalent continuum solid fiber shaped as a hollow cylinder. Its dimensions coincide with those of the interphase region: the length is equal to that of the embedded nanotube (l) while inner radius $r^i = d/2 + t^{if}$ and outer radius $r^f = d/2 + t^{if} + t^{ip}$. Since in Section 5.4 we model the reinforcement provided by the interphase through one-dimensional elements, the equivalent continuum fibers are assumed isotropic and the mechanical properties are averaged through the thickness.

Young's modulus E^f and Poisson's ratio ν^f of the equivalent continuum solid fiber are determined through an identification procedure where the axial stiffness of the atomistic model and that of the intermediate continuum micromechanical model are compared. This problem is formulated as

$$\text{find } \min_p f(p), \quad (5.16)$$

with $p = [E^f, \nu^f]$ the vector of unknown parameters and $f(p)$ the cost function

$$f(p) = \frac{1}{2} \sum_{i=x,y} \left(\frac{C_{xi}^c - \tilde{C}_{xi}^c(E^f, \nu^f)}{C_{xi}^c} \right)^2, \quad (5.17)$$

where C_{xi}^c are the elastic components of the CNT-polymer composites derived from the MM simulations (Section 5.2.3) and \tilde{C}_{xi}^c those from the corresponding continuum models in Figure 5.1b. The least-square problem (5.16) was solved using the Gauss-Newton algorithm [55]. This iterative procedure was terminated when both $f(p)$ and the infinity norm of the gradient $\nabla_p f(p)$ were lower than 10^{-10} .

5.3.1 Numerical solution

The elastic components \tilde{C}_{xx}^c and \tilde{C}_{xy}^c of the continuum model in Figure 5.1b have been derived with isogeometric analysis. Due to the hollow cylindrical shape of the equivalent continuum three-dimensional fiber, isogeometric finite elements [39] were employed. Cubic Non-Uniform B-spline (NURBS) basis functions were used to exactly represent the equivalent continuum fiber and bulk matrix geometries, and at the same time to approximate the corresponding displacement fields. As for the MM tensile tests, periodic boundary conditions in all directions together with the macrostrain tensor (5.11) have been enforced. Due to symmetry with respect to planes xy , xz and yz , only an eight of the full model (see Figure 5.7a) is considered and the corresponding boundary conditions are depicted in Figure 5.7b (see Appendix 5.A for details).

A NURBS multi-patch code [25, 39] was employed to generate the isogeometric model. As illustrated in Figure 5.7c, the model is defined by five patches: one for the equivalent continuum fiber and four for the bulk polymer matrix. According to Hughes et al. [39], the geometry of each patch is defined by

$$S(\xi, \eta, \zeta) = \sum_{i=1}^{n_\xi} \sum_{j=1}^{n_\eta} \sum_{k=1}^{n_\zeta} N_{i,p}(\xi) M_{j,q}(\eta) L_{k,r}(\zeta) B_{i,j,k}, \quad (5.18)$$

where ξ , η and ζ are coordinates in the so-called parameter space, $N_{i,p}(\xi)$, $M_{j,q}(\eta)$ and $L_{k,r}(\zeta)$ NURBS basis functions of degree p , q and r , respectively, and $B_{i,j,k}$ the control points (the reader is referred to Hughes et al. [39] for more details on NURBS geometries and isogeometric analysis). NURBS basis functions $N_{i,p}(\xi)$, $M_{j,q}(\eta)$ and $L_{k,r}(\zeta)$ are defined by the knot vectors $\Xi = [\xi_1, \xi_2, \dots, \xi_{n_\xi+p+1}]$, $\mathcal{H} = [\eta_1, \eta_2, \dots, \eta_{n_\eta+q+1}]$ and $\mathcal{Z} = [\zeta_1, \zeta_2, \dots, \zeta_{n_\zeta+r+1}]$, respectively. Parameters n_ξ , n_η and n_ζ indicate the number of

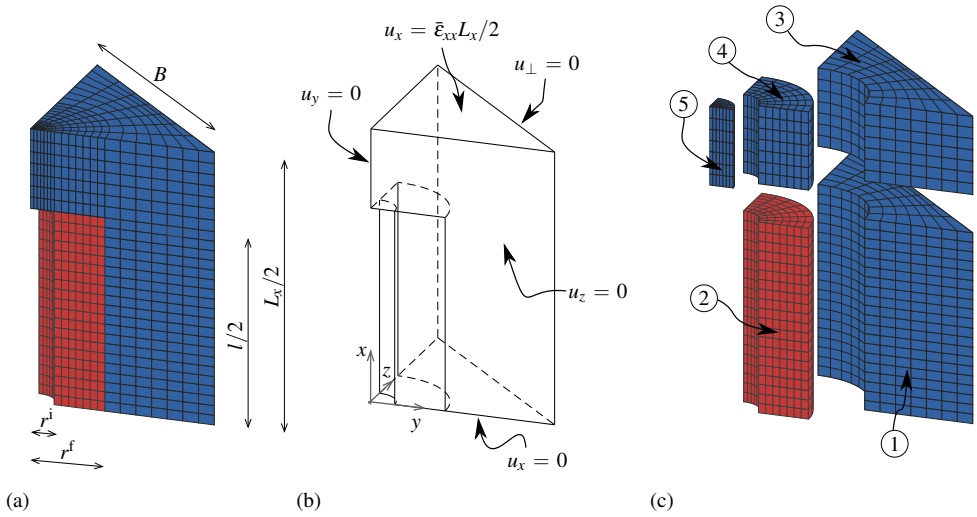


Figure 5.7: (a) NURBS isogeometric model of the equivalent continuum (only an eight of the composite is considered due to symmetry). The bulk matrix is in blue, the equivalent continuum fiber in red. Quantities r^i and r^f refer to the inner and outer radius of the equivalent continuum fiber, respectively, l its length and L_x and B denote the RVE size. (b) Schematic of the applied boundary conditions (u_{\perp} denotes displacements orthogonal to the considered face of the model). (c) Exploded view of the isogeometric model showing the five NURBS patches and numbering of the different NURBS patches.

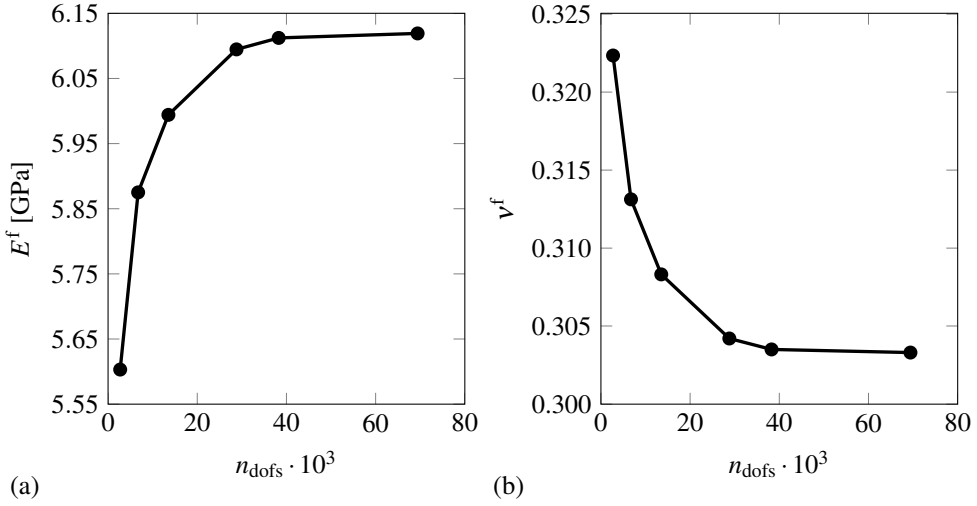


Figure 5.8: Convergence of the estimated (a) E^f and (b) ν^f with respect to the number of degrees of freedom n_{dofs} for an (8,8)-polymer composite.

Patch	m_ξ	m_η	m_ζ
1	21	8	8
2	21	8	8
3	8	8	8
4	8	8	8
5	8	8	8

Table 5.3: Number of knots along ξ , η and ζ (denoted by m_ξ , m_η and m_ζ , respectively) for the five NURBS patches used in the estimation of the Young's modulus E^f and Poisson's ratio ν^f of the equivalent continuum fiber.

basis functions $N_{i,p}(\xi)$, $M_{j,q}(\eta)$ and $L_{k,r}(\zeta)$. Moreover, each control point $B_{i,j,k}$ is associated to a weight $w_{i,j,k}$. Therefore, each NURBS patch is defined by a set of knot vectors, control points and weight. The full data structure is provided in Appendix 5.B.

The k -refinement approach [39] has been employed to increase the degree of the NURBS basis functions to cubic and insert new knots along the ξ , η and ζ directions until convergence in the values of E^f and ν^f (see Figure 5.8). In particular, knots were inserted such that the knot vectors were uniform (i.e. evenly spaced knots) and the dimensions of the elements in the three directions close to each others. The final number of knots along ξ , η and ζ is reported in Table 5.3 (the same discretization has been used for all the CNT-polymer composites).

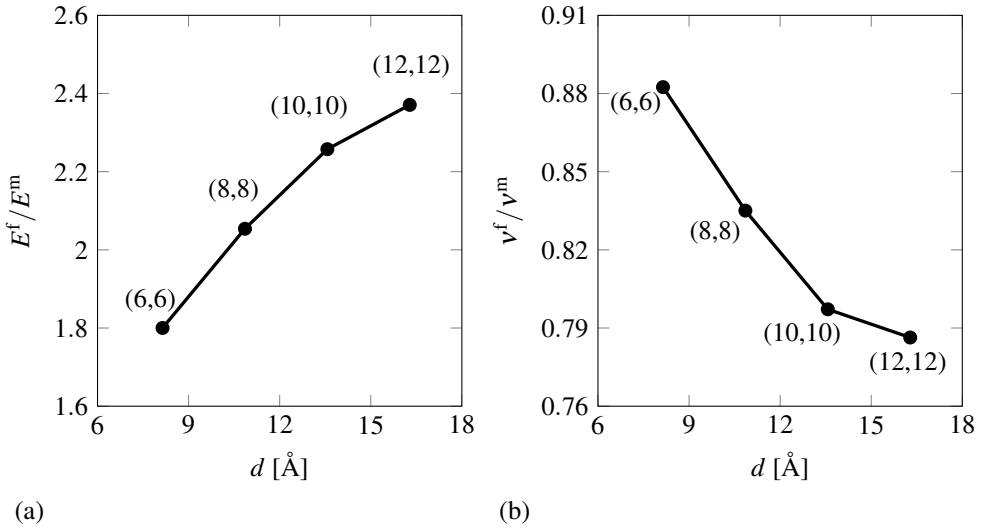


Figure 5.9: (a) Young's modulus E^f and (b) Poisson's ratio v^f of the equivalent continuum fiber in (n,n) -polymer composites as a function of the nanotube d . Results have been normalized with respect to the polymer Young's modulus $E^m = 3.04$ GPa and Poisson's ratio $v^m = 0.36$. Since the ordering of the interphase atomic structure increases with the CNT diameter [52], E^f increases with d while the opposite trend is observed for v^f .

5.3.2 Size effects

Figure 5.9 shows the Young's modulus E^f and the Poisson's ratio v^f of the equivalent continuum fiber obtained from the parameter estimation procedure described in the previous section. The CNT diameter influences both E^f and v^f . The Young's modulus increases with the diameter d of the embedded nanotube while the Poisson's ratio decreases. Therefore, the overall stiffness of the interphase increases with d . This was expected as higher ordering in the interphase was observed when increasing the nanotube diameter [26, 52].

Although the stiffness of the equivalent continuum fiber increases with the CNT diameter, the opposite trend was observed in Section 5.2.3 for the components of the elasticity tensor of the composite: the bigger the d , the weaker the CNT-polymer composite. Nevertheless, this is a consequence of the decreasing volume fraction of interphase v^{ip} in the composites reinforced with nanotubes of bigger diameters (see Figure 5.4). Therefore, the results in Figures 5.4 and 5.9 indicate that v^{ip} plays a central role in the value of the mechanical properties of the CNT-polymer composites.

5.4 Micromechanical models for CNT-polymer composites

Having defined the elastic properties of bulk polymer and equivalent continuum fiber, we can investigate the macroscopic mechanical response of CNT-polymer composites. Due to the negligible effect of the CNT on the mechanical response of the composite, the microme-

chanical model for the CNT-polymer composite considers only the polymer matrix and the interphase as in the continuum model studied in the previous section. Moreover, with reference to real composites, the equivalent continuum fiber can be modeled as a one-dimensional fiber due to the high aspect ratio of the real nanotubes –throughout the rest of the paper the term “fiber” is used to refer to the one-dimensional equivalent continuum fiber. To model CNT-polymer composites with realistic nanotube volume fractions, thus with a high number of fibers as shown in Figure 5.1c, the Embedded Reinforcement Method (ERM) is adopted. This numerical procedure is employed in the analysis of periodic RVEs with different CNT volume fractions and to investigate CNT diameter-induced effects. The numerical results are then compared to estimate from various analytical micromechanical models in Section 5.5.

5.4.1 The embedded reinforcement method

The embedded reinforcement method [22, 59] allows to efficiently incorporate fibers into a discretized continuum without actually meshing them as shown in Figure 5.10a where a discrete fiber is embedded into a 3-D element. Although this model can be modified to incorporate fiber slip [5, 24], here fibers are perfectly bonded to the matrix since there is no relative displacement between interphase and surrounding polymer.

For completeness, the derivation of the discrete set of equations governing the mechanical response of an element with one embedded fiber is reported next. We consider an elastic body with total volume Ω subdivided into matrix (Ω^m) and fiber (Ω^f) parts. In the absence of the external load, the principle of virtual work can be written as

$$\int_{\Omega^m} \nabla^s \delta \mathbf{u}^m : \mathbf{C}^m : \nabla^s \mathbf{u}^m d\Omega^m + \int_{\Omega^f} (\delta u_{,s}^f (E^f - E^m) u_{,s}^f) d\Omega^f = 0, \quad (5.19)$$

where \mathbf{C}^m is the elasticity tensor of the bulk polymer (see (5.14)), E^f and E^m are the equivalent continuum fiber and bulk polymer elastic moduli derived in Section 5.3, ∇^s is the symmetric-gradient operator, δ denotes variation, and we used subscript notation for differentiation (a derivative with respect to the fiber local axis is indicated by the subscript “,s”). We exclude bulk material in the fiber domain by using the effective elastic moduli ($E^f - E^m$) in the second term of (5.19). The displacement components \mathbf{u}^m of a bulk element with n nodes (for trilinear hexahedral elements, n is equal to 8) can be discretized at any arbitrary point \mathbf{x} through

$$\mathbf{u}^m(\mathbf{x}) = \sum_{i=1}^n N_i^m(\mathbf{x}) \mathbf{u}_i(\mathbf{x}) \quad (5.20)$$

with N_i^m the shape functions of the bulk element and \mathbf{u}_i the corresponding degrees of freedom. Thus, the discretized displacements and strains can be written in matrix form as

$$\mathbf{u}^m(\mathbf{x}) = \mathbf{N}^m \mathbf{u} \quad \text{and} \quad (5.21a)$$

$$\boldsymbol{\varepsilon}^m(\mathbf{x}) = \mathbf{B}^m \mathbf{u}, \quad (5.21b)$$

respectively, where \mathbf{N}^m and \mathbf{B}^m are matrices containing shape functions and corresponding derivatives, and \mathbf{u} is the element displacement vector. The scalar fiber displacement u^f

along the fiber local axis s is approximated using one-dimensional linear Lagrangian shape functions as

$$u^f(s) = N_{s_1}^f(s)a_{s_1} + N_{s_2}^f(s)a_{s_2}, \quad (5.22)$$

where $N_{s_1}^f$ and $N_{s_2}^f$ are the shape functions attributed to the fiber end points s_1 and s_2 , respectively, while a_{s_1} and a_{s_2} are the corresponding local displacements (see Figure 5.10b). The fiber displacement is transferred from the local fiber coordinate system (s) to the global coordinate system (x, y, z) by means of

$$u^f(s) = \begin{bmatrix} N_{s_1}^f \cos(\theta_x^s) & N_{s_1}^f \cos(\theta_y^s) & N_{s_1}^f \cos(\theta_z^s) & N_{s_2}^f \cos(\theta_x^s) \\ N_{s_2}^f \cos(\theta_y^s) & N_{s_2}^f \cos(\theta_z^s) \end{bmatrix} \begin{bmatrix} u_{s_1}^f \\ u_{s_2}^f \end{bmatrix}$$

with $\mathbf{u}_{s_i}^f = [a_{x_i}^f, a_{y_i}^f, a_{z_i}^f]^T$ the global displacement vector at fiber endpoints and θ_i^s (with $i = x, y, z$) the fiber orientation angles. The derivatives of (5.23) with respect to the fiber axis are expressed as

$$u_{,s}^f(\mathbf{x}) = \mathbf{B}^f \mathbf{H} \mathbf{u}, \quad (5.23)$$

with

$$\mathbf{B}^f = \begin{bmatrix} N_{s_1,s}^f \cos(\theta_x^s) & N_{s_1,s}^f \cos(\theta_y^s) & N_{s_1,s}^f \cos(\theta_z^s) & N_{s_2,s}^f \cos(\theta_x^s) & N_{s_2,s}^f \cos(\theta_y^s) \\ N_{s_2,s}^f \cos(\theta_z^s) \end{bmatrix}$$

and

$$\mathbf{H} = \begin{bmatrix} N_1^m(\mathbf{s}_1) & 0 & 0 & \cdots & N_n^m(\mathbf{s}_1) & 0 & 0 \\ 0 & N_1^m(\mathbf{s}_1) & 0 & \cdots & 0 & N_n^m(\mathbf{s}_1) & 0 \\ 0 & 0 & N_1^m(\mathbf{s}_1) & \cdots & 0 & 0 & N_n^m(\mathbf{s}_1) \\ N_1^m(\mathbf{s}_2) & 0 & 0 & \cdots & N_n^m(\mathbf{s}_2) & 0 & 0 \\ 0 & N_1^m(\mathbf{s}_2) & 0 & \cdots & 0 & N_n^m(\mathbf{s}_2) & 0 \\ 0 & 0 & N_1^m(\mathbf{s}_2) & \cdots & 0 & 0 & N_n^m(\mathbf{s}_2) \end{bmatrix}, \quad (5.24)$$

where \mathbf{H} is the transformation matrix mapping fiber displacements $\mathbf{u}_{s_i}^f$ into bulk element displacements \mathbf{u} , while \mathbf{s}_1 and \mathbf{s}_2 are the coordinates of the fiber endpoints in the bulk element coordinate system. Finally, introducing the discretized interpolations of matrix (5.21b) and fiber (5.23) derivatives into the weak momentum equation (5.19) yields the total stiffness matrix of an element with an embedded fiber

$$\mathbf{K} = \int_{\Omega^m} \mathbf{B}^{mT} \mathbf{C}^m \mathbf{B}^m d\Omega + A^f \int_{l^f} \mathbf{H}^T \mathbf{B}^{fT} (E^f - E^m) \mathbf{B}^f \mathbf{H} ds, \quad (5.25)$$

where, since a uniform cross sectional area A_f is assumed for the fiber, the fiber volume integral in (5.19) is replaced by an equivalent line integral over the portion of fiber l^f embedded in the solid element. In the case of multiple fibers embedded in a single element, the total stiffness matrix

$$\mathbf{K} = \int_{\Omega^m} \mathbf{B}^{mT} \mathbf{C}^m \mathbf{B}^m d\Omega + \sum_{i=1}^{n_f} A_i^f \int_{l_i^f} \mathbf{H}_i^T \mathbf{B}_i^{fT} (E_i^f - E^m) \mathbf{B}_i^f \mathbf{H}_i ds_i, \quad (5.26)$$

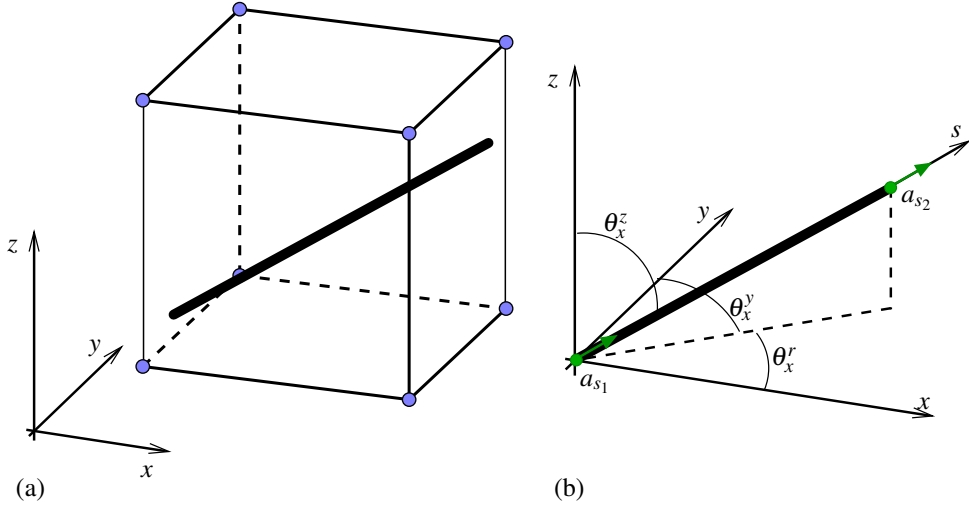


Figure 5.10: (a) A hexahedral finite element with one embedded fiber: degrees of freedom (blue circles) are located only at the nodes of the embedding element. (b) Global coordinate system (x, y, z) and fiber local axis s (local displacements a_{s_1} and a_{s_2} at the fiber endpoints in green).

in which n_f is the number of fibers in the solid element. As shown in (5.25) and (5.26), the total stiffness matrix of a solid element for the composite material is given by the sum of the stiffness matrix of the bulk polymer matrix and the stiffness contribution(s) of the embedded one-dimensional fiber(s).

Effective mechanical properties and periodic boundary conditions

The macroscopic elastic properties of the CNT-polymer composite are derived through computational homogenization. For a generic RVE, Hooke's law is expressed as

$$\begin{bmatrix} \bar{\sigma}_{xx} \\ \bar{\sigma}_{yy} \\ \bar{\sigma}_{zz} \\ \bar{\sigma}_{xy} \\ \bar{\sigma}_{xz} \\ \bar{\sigma}_{yz} \end{bmatrix} = \begin{bmatrix} C_{11}^c & C_{12}^c & C_{13}^c & C_{14}^c & C_{15}^c & C_{16}^c \\ C_{21}^c & C_{22}^c & C_{23}^c & C_{24}^c & C_{25}^c & C_{26}^c \\ C_{31}^c & C_{32}^c & C_{33}^c & C_{34}^c & C_{35}^c & C_{36}^c \\ C_{41}^c & C_{42}^c & C_{43}^c & C_{44}^c & C_{45}^c & C_{46}^c \\ C_{51}^c & C_{52}^c & C_{53}^c & C_{54}^c & C_{55}^c & C_{56}^c \\ C_{61}^c & C_{62}^c & C_{63}^c & C_{64}^c & C_{65}^c & C_{66}^c \end{bmatrix} \begin{bmatrix} \bar{\epsilon}_{xx} \\ \bar{\epsilon}_{yy} \\ \bar{\epsilon}_{zz} \\ \bar{\epsilon}_{xy} \\ \bar{\epsilon}_{xz} \\ \bar{\epsilon}_{yz} \end{bmatrix}, \quad (5.27)$$

where the parameters C_{ij}^c are the components of the homogenized effective elasticity tensor for the composite material. These are determined imposing the six sets of boundary conditions in Table 5.4 (the full set of constraint equations to be imposed on RVE faces, edges and vertices are listed in Appendix 5.A). Then, for each boundary condition, the corresponding local stress field $\boldsymbol{\sigma}$ in the composite is determined using the ERM described in Section 5.4.1.

Boundary condition	Macrostrain tensor $\bar{\boldsymbol{\epsilon}}$	Derived components of \mathbf{C}^c
Uniaxial tension	$[0.1, 0, 0, 0, 0, 0]^T$	C_{i1}^c
	$[0, 0.1, 0, 0, 0, 0]^T$	C_{i2}^c
	$[0, 0, 0.1, 0, 0, 0]^T$	C_{i3}^c
Transverse shear	$[0, 0, 0, 0.1, 0, 0]^T$	C_{i4}^c
	$[0, 0, 0, 0, 0.1, 0]^T$	C_{i5}^c
	$[0, 0, 0, 0, 0, 0.1]^T$	C_{i6}^c

Table 5.4: Macrostrain tensor and derived components of \mathbf{C}^c for uniaxial tension and transverse shear boundary condition.

Consequently, the macrostress tensor $\bar{\boldsymbol{\sigma}}$ is calculated as

$$\bar{\boldsymbol{\sigma}} = \frac{1}{V} \int_V \boldsymbol{\sigma} dV, \quad (5.28)$$

where V is the volume of the RVE. Hence, knowing the macrostrain and macrostress tensors $\bar{\boldsymbol{\epsilon}}$ and $\bar{\boldsymbol{\sigma}}$, respectively, the effective elasticity tensor components C_{ij}^c are derived from (5.27).

Once the effective mechanical properties in (5.27) are known, we can provide an estimate of the engineering constants (Young's modulus, shear modulus and Poisson's ratio). For composites with perfectly aligned CNTs along the x axis, the RVE is transversely isotropic and the elastic constitutive matrix is

$$\mathbf{C}^c = \begin{bmatrix} C_{xx}^c & C_{xy}^c & C_{xy}^c & 0 & 0 & 0 \\ C_{xy}^c & C_{yy}^c & C_{yz}^c & 0 & 0 & 0 \\ C_{xy}^c & C_{yz}^c & C_{yy}^c & 0 & 0 & 0 \\ 0 & 0 & 0 & 2G_{xy}^c & 0 & 0 \\ 0 & 0 & 0 & 0 & 2G_{yz}^c & 0 \\ 0 & 0 & 0 & 0 & 0 & 2G_{yz}^c \end{bmatrix}. \quad (5.29)$$

Two of the five independent constants, the shear moduli G_{xy}^c and G_{yz}^c , are known from (5.29) and, following Afddl and Kardos [2], the remaining three are expressed according to

$$E_{xx}^c = C_{xx}^c - \frac{2C_{xy}^c C_{xy}^c}{C_{yy}^c + C_{yz}^c}, \quad (5.30a)$$

$$E_{yy}^c = \frac{(C_{yy}^c - C_{yz}^c)(C_{yy}^c C_{xx}^c + C_{yz}^c C_{xx}^c - 2C_{xy}^c C_{xy}^c)}{C_{yy}^c C_{xx}^c - C_{xy}^c C_{xy}^c}, \quad \text{and} \quad (5.30b)$$

$$\nu_{xy}^c = \frac{C_{xy}^c}{C_{yy}^c + C_{yz}^c}. \quad (5.30c)$$

For randomly oriented fibers, the RVE is isotropic and the elastic constitutive matrix is ex-

pressed as

$$\mathbf{C}^c = \begin{bmatrix} \lambda^c + 2\mu^c & \lambda^c & \lambda^c & 0 & 0 & 0 \\ \lambda^c & \lambda^c + 2\mu^c & \lambda^c & 0 & 0 & 0 \\ \lambda^c & \lambda^c & \lambda^c + 2\mu^c & 0 & 0 & 0 \\ 0 & 0 & 0 & \mu^c & 0 & 0 \\ 0 & 0 & 0 & 0 & \mu^c & 0 \\ 0 & 0 & 0 & 0 & 0 & \mu^c \end{bmatrix}, \quad (5.31)$$

where λ^c and μ^c are the Lamé parameters. The corresponding Young's modulus and shear modulus are

$$E^c = \frac{\mu^c (3\lambda^c + 2\mu^c)}{\lambda^c + \mu^c} \quad \text{and} \quad G^c = \mu^c, \quad (5.32)$$

respectively.

RVE generation

The ERM has been used for the analysis of cubic periodic RVEs with equally long and randomly distributed fibers, here representing the interphases, either perfectly aligned along the x direction or randomly oriented. The method used for the generation of the RVEs, implemented in Matlab[®], followed the Random Sequential Adsorption algorithm [9, 42, 81]. Accordingly, fibers are added consecutively to the RVEs until a specific volume fraction is reached. In unidirectional fiber composites, all fibers are aligned along the x -axis while in randomly oriented fiber composites the orientation of each fiber is determined using the Matlab[®] function `rand`. For both unidirectional and randomly oriented fiber composites, the `rand` function is used to define the coordinates of one of the end points of a fiber. As the fiber length is a known parameter, the coordinates of the second end of a fiber can be easily derived. If this point lies outside the RVE, the exceeding part of the fiber is cut and shifted to the opposite boundary to enforce periodicity. To avoid fiber overlap, when a new fiber is added to the RVE we check that the distance between its axis and that of the exiting fibers is larger than twice the radius of the fibers (i.e., the outer radius of the interphase). If this condition is not satisfied, the fiber is removed and a new one is created. This process is repeated until the requirement for the minimum distance between fibers is fulfilled.

Assessment of fibers orientation distribution Fiber orientation has a strong influence on the mechanical properties of the composite. Therefore, after the RVEs were created, the overall orientation of the fibers, also known as the orientation distribution, has been characterized. The orientation distribution was measured through the second order tensor of fiber orientation [1, 48]. With reference to Figure 5.11a, the orientation of a single fiber is defined by the unit vector \mathbf{p} with components

$$p_1 = \sin \theta \cdot \cos \phi, \quad (5.33a)$$

$$p_2 = \sin \theta \cdot \sin \phi \quad \text{and} \quad (5.33b)$$

$$p_3 = \cos \theta, \quad (5.33c)$$

where θ is the angle between the fiber axis and the z -axis, and ϕ is the angle between the projection of the fiber on the xy -plane and the x -axis. Accordingly, the second order tensor

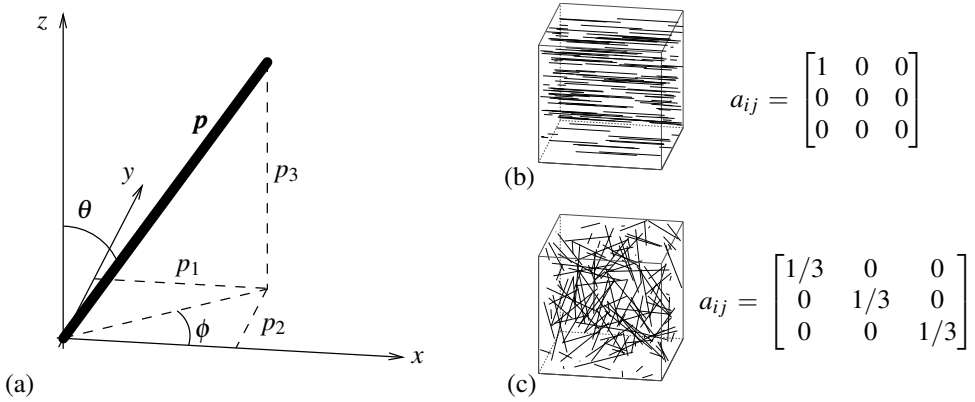


Figure 5.11: (a) Definition of angles θ and ϕ used to calculate the orientation of a CNT (thick solid line) through the unit vector \mathbf{p} with components p_1 , p_2 and p_3 . Composites with CNTs perfectly aligned along the x -axis (b) and randomly oriented CNTs (c).

\mathbf{a} of fiber order orientation is calculated as

$$\mathbf{a} = a_{ij} = \frac{1}{n^{\text{CNT}}} \sum_{k=1}^{n^{\text{CNT}}} p_i^k p_j^k = \begin{bmatrix} a_{11} & a_{12} & a_{13} \\ a_{12} & a_{22} & a_{23} \\ a_{13} & a_{23} & a_{33} \end{bmatrix} \quad (5.34)$$

with n^{CNT} the number of fibers in the RVE. Only six of the nine components of a_{ij} are independent due to its symmetry. Figures 5.11b and c show the second order tensor \mathbf{a} for composites with fibers perfectly aligned along the x axis and randomly oriented, respectively. For an (8,8)-polymer composite with 6915 randomly oriented fibers, later used in our simulations,

$$a_{ij} = \begin{bmatrix} 0.330 & -0.003 & -0.003 \\ -0.003 & 0.339 & -0.003 \\ -0.003 & -0.003 & 0.331 \end{bmatrix}. \quad (5.35)$$

The second order tensor in (5.35) is very close to that in Figure 5.11c, indicating that fibers can be considered as evenly oriented in the three directions. Analogous results were derived for all the RVEs used in our simulations. The second order tensor of fiber orientation was calculated also for RVEs with unidirectional fibers and it coincided with that in Figure 5.11b.

RVE dimensions

The size of the RVE should be sufficiently large to be statistically representative of the macroresponse of the composite and such that its mechanical properties do not depend on the dimensions of the inclusions [33, 37, 57]. In this case it seems reasonable to require that the RVE size should at least be larger than the nanotube length, typically in the range of some micrometers [3, 19, 35, 63]. However, this would imply large RVEs with a very high number of CNTs due to their high aspect ratio and, consequently, a prohibitive computational effort.

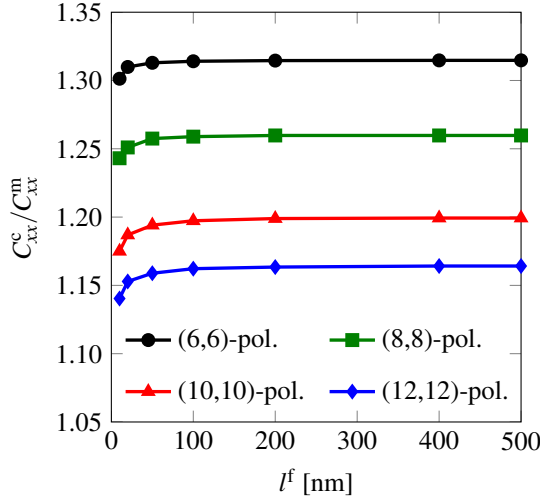


Figure 5.12: Variation of C_{xx}^c with the length l^f of the embedded fibers. These results, normalized with respect to $C_{xx}^m = 5.14$ GPa, were derived with the ERM for different (n,n) -polymer composites with fibers aligned along the x direction and $v^{\text{CNT}} = 1.5\%$. Similar results were observed for C_{xy}^c .

To avoid this issue, before defining the size of the RVE, we determined the minimum length of the embedded fibers above which the elastic properties of the RVEs do not change. This allows for the generation of smaller RVEs with a lower number of fibers and, at the same time, avoids length effects in the mechanical properties of the composites (in this work we focus only on diameter-induced effects). Figure 5.12 shows that C_{xx}^c can be assumed constant for $l^f \geq 200$ nm as previously observed through multiscale simulations on CNT-polyimide composites [56].

Then, using $l^f = 200$ nm we investigated the effects induced by the RVEs size. This was performed through the analysis of C_{xx}^c changing the size L of the cubic RVE. For each value of L , four different RVEs were created and the standard deviation from the mean value of C_{xx}^c was calculated. This procedure was performed for CNT-polymer composites with v^{CNT} equal to 0.6 and 1.5%. As shown in Figure 5.13a and b, the dispersion is always lower than 2% and decreases when increasing L similarly to the results in Reference [41]. For $L/l^f = 2$, standard deviation further decreases and the averaged values of C_{xx}^c are more in line with those obtained for larger RVEs. Therefore, in our simulations the size of the RVE was assumed twice the length of the embedded fibers (i.e., 400 nm) as also suggested in other works on short fiber reinforced composites [42, 71].

Meshing the RVEs

As mentioned in Section 5.4.1 the RVEs are discretized using hexahedral finite elements. Since the fibers are uniformly distributed in the matrix and because of the modest stress concentration at the fiber ends, we employed uniform meshes for all the RVEs.

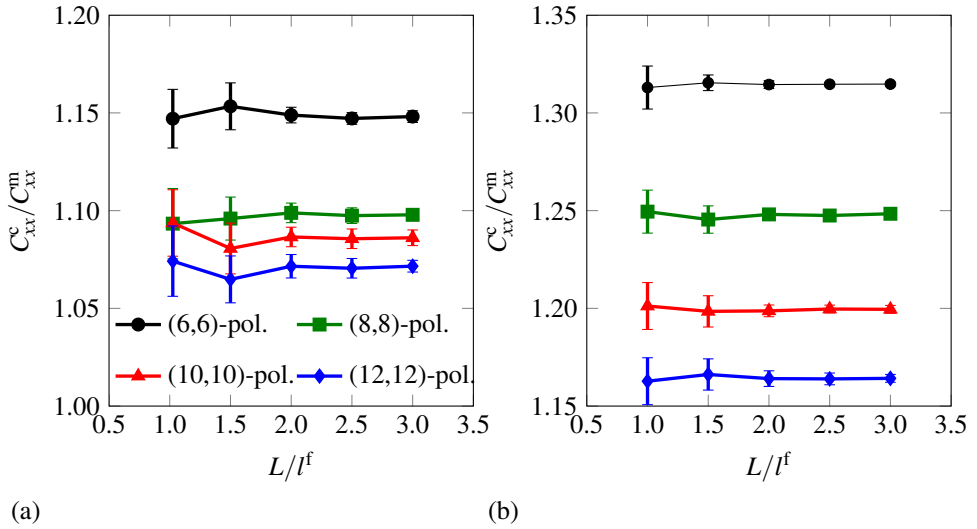


Figure 5.13: Variation of C^c_{xx} with the side L of cubic RVEs for (n,n) -polymer composites with v^{CNT} equal to (a) 0.6% and (b) 1.5%. The values of C^c_{xx} and L have been normalized with respect to $C^m_{xx} = 5.14$ GPa and the fiber length $l^f = 200$ nm, respectively. For each case, four different samples were considered. Error bars indicate standard deviations from the mean values of C^c_{xx} denoted by the symbols.

The size of the cubic hexahedral elements $L_e = L/n_{\text{sub}}$, where n_{sub} is the number of subdivisions per RVE side, was determined from the variation of the RVE elastic properties while refining the mesh. This analysis was performed on the RVE with the highest number of embedded fibers, a (6,6)-polymer composite with v^{CNT} equal to 2% (12293 CNTs). The length of the fibers and that of the RVE side were set equal to 200 and 400 nm according to the results in the previous section.

Figure 5.14 shows that the difference between the estimated E^c and G^c with respect to the values obtained with the finer mesh (i.e., $n_{\text{sub}} = 30$) is negligible when $n_{\text{sub}} \geq 20$. Therefore, for all the simulations we adopted a uniform mesh with cubic hexahedral elements of size L_e equal to $L/20$.

5.5 Elastic properties of the nanocomposite

In this section, we assess the influence of the reinforcement provided by the interphase on the macroscopic properties of the CNT-polymer composites. As shown in Table 5.5, we employed values of v^{CNT} between 0.2 and 2.0% [27, 35, 64] to avoid intersections between different fibers (i.e., the interphase regions). Accordingly, the number of embedded fibers in the generated RVEs ranges from 307 to 12293 for both unidirectional and randomly oriented CNTs (see Figure 5.15a and b, respectively). Three different RVEs were created for each configuration and results were averaged.

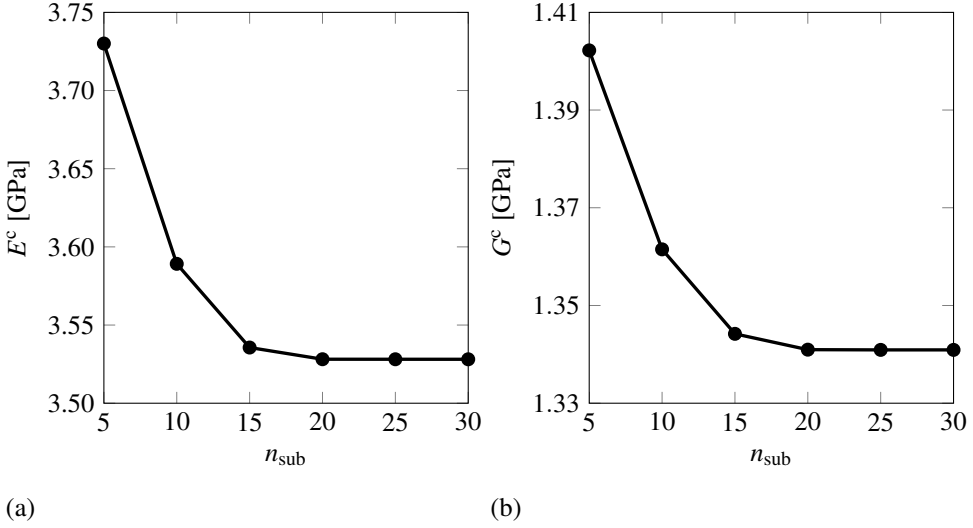


Figure 5.14: Numerical convergence of E^c and G^c for a (6,6)-polymer composite with $v^{\text{CNT}} = 2\%$ (corresponding to 12293 CNTs).

v^{CNT}	0.2%	0.6%	1.0%	1.5%	2.0%
(6,6)-polymer	1229	3688	6146	9220	12293
(8,8)-polymer	691	2074	3457	5186	6915
(10,10)-polymer	443	1328	2213	3319	4425
(12,12)-polymer	307	922	1537	2305	3073

Table 5.5: Number of embedded fibers in the RVEs.

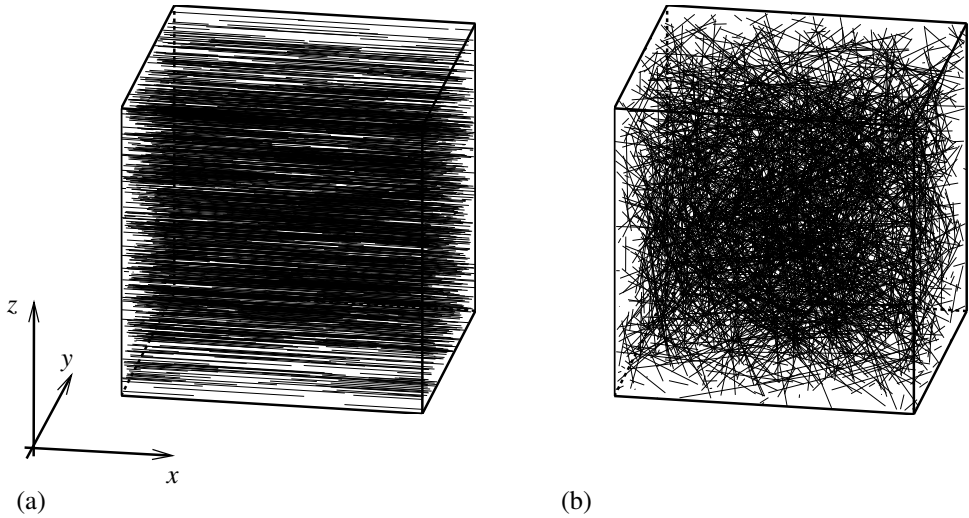


Figure 5.15: Periodic RVEs of (8,8)-polymer composites with (a) unidirectional and (b) randomly oriented nanotubes with $v^{\text{CNT}} = 1\%$ (i.e., 3457 CNTs).

The elastic properties of the composites are derived through the modeling approach in Section 5.4 and some analytical micromechanical models discussed in the next section.

5.5.1 Analytical micromechanical models

Analytical micromechanical models are commonly used to estimate the mechanical properties of fiber reinforced materials. Some of the most frequently used micromechanical models are briefly summarized below. In the next sections, their predictions are compared with numerical results obtained with the embedded reinforcement method presented in Section 5.4.1.

Shear lag models [40] are typically employed to provide an analytical solution for the stress distribution in short fiber composites and an estimate of their mechanical properties. The classical formulation proposed by Cox [21] examines the axial stress along a single short fiber encased in a continuous solid matrix. The matrix, assumed void free, is considered elastic and isotropic. The load is transferred from the matrix to the fiber through shear stresses at their interface where matrix and fibers are perfectly bonded. Based on the results from [21], for a composite reinforced with unidirectional perfectly aligned and equally spaced short fibers, with equal length and stiffness, the Young's modulus in the fibers direction (the x -axis in this work) is estimated through the modified rule of mixture

$$E_{xx}^c = \eta_l v^f E^f + (1 - v^f) E^m. \quad (5.36)$$

The variable v^f is the fiber volume fraction (here coinciding with v^{ip}) and the coefficient η_l ,

which takes into account the aspect ratio of the fibers [21], is calculated as

$$\eta_l = 1 - \frac{\tanh(\beta l/2)}{\beta l/2} \quad \text{with} \quad \beta = \sqrt{\frac{2G^m}{E^f (r^f)^2 \ln(R/r^f)}}, \quad (5.37)$$

where G^m is the matrix shear modulus, R is half the distance between the axis of the fibers [40], and r^f is their radius. For randomly oriented fibers of equal length, Krenchel [44] proposed a modified version of (5.36):

$$E^c = \frac{1}{5} \eta_l v^f E^f + (1 - v^f) E^m. \quad (5.38)$$

The Halpin-Tsai model [2] is based on the same assumptions of the shear lag model and provides the following equation for the Young's modulus in the direction of the fibers:

$$E_{xx}^c = E^m \frac{1 + \xi_P \eta v^f}{1 - \eta v^f} \quad (5.39)$$

with

$$\eta = \frac{E^f/E^m - 1}{E^f/E^m + \xi} \quad \text{and} \quad \xi = 2l/d^f. \quad (5.40)$$

A modified version of (5.39), referred to as the Tsai-Pagano equation [69, 73], has been proposed for the calculation of the Young's modulus of composites with randomly oriented fibers in 3-D:

$$E^c = E^m \left[\frac{3}{8} \frac{1 + \xi \eta (1 - v^f)}{1 - \eta v^f} + \frac{5}{8} \frac{1 + \xi \eta (1 - v^f)}{1 - \eta v^f} \right]. \quad (5.41)$$

Further, we have considered the micromechanical model proposed by Pan [58] for composite materials with randomly oriented fibers. Here, the Young's modulus is defined as

$$E^c = E^f \frac{v^f}{2\pi} + E^m \left(1 - \frac{v^f}{2\pi} \right). \quad (5.42)$$

Finally, the numerical results have been compared to the Hashin-Shtrikman bounds [34] derived through variational principles for statistically isotropic and nonhomogeneous composite materials. For the present composites, the lower and upper bounds (denoted with the superscripts (-) and (+)) for the bulk and shear moduli are

$$K^{c(-)} = K^m + \frac{v^f}{1/(K^f - K^m) + 3(1 - v^f)/(3K^m + 4G^m)}, \quad (5.43a)$$

$$K^{c(+)} = K^f + \frac{1 - v^f}{1/(K^m - K^f) + 3v^f/(3K^f + 4G^f)}, \quad (5.43b)$$

$$G^{c(-)} = G^m + \frac{v^f}{1/(G^f - G^m) + 6(1 - v^f)(K^m + 2G^m)/(5G^m(3K^m + 4G^m))}, \quad (5.43c)$$

$$G^{c(+)} = G^f + \frac{1 - v^f}{1/(G^m - G^f) + 6v^f(K^f + 2G^f)/(5G^f(3K^f + 4G^f))}, \quad (5.43d)$$

respectively. Consequently, the lower and upper bounds for the composite Young's modulus are

$$E^{c(-)} = \frac{9K^{(-)}G^{(-)}}{3K^{(-)} + G^{(-)}} \quad \text{and} \quad E^{c(+)} = \frac{9K^{(+)}G^{(+)}}{3K^{(+)} + G^{(+)}}. \quad (5.44)$$

5.5.2 Unidirectional reinforcement

Figures 5.16a-e show the variation of the Young's moduli E_{xx}^c , E_{yy}^c , the Poisson's ratio ν_{xy}^c and the shear moduli G_{xy}^c and G_{yz}^c , respectively, for composites with CNTs perfectly aligned along the x direction. Results indicate an overall improvement of the stiffness with increasing CNT volume fraction. More specifically, E_{xx}^c , E_{yy}^c , G_{xy}^c and G_{yz}^c linearly increase with ν^{CNT} while the opposite trend is observed for ν_{xy}^c . Due to the unidirectional orientation of the embedded reinforcements, the major improvements are noticed in E_{xx}^c while the variation of the other engineering constants is modest.

In the macroscopic model, unidirectional fibers are randomly located (i.e., not evenly spaced) in the RVE, in contrast with the hypothesis of evenly spaced fibers adopted by the micromechanical models presented in Section 5.5.1. Nevertheless, as depicted in Figure 5.16a, the values of E_{xx} obtained with the numerical simulations are in good agreement with those provided by the analytical micromechanical models, and especially with the Halpin-Tsai model [29]. For the sake of completeness, we generated also RVEs with equally spaced unidirectional fibers and the corresponding results (not shown here) were identical to those reported in Figures 5.16a-e.

5.5.3 Random reinforcement

For the case of randomly oriented CNTs, the out of diagonal terms in the second order tensor of fibers distribution a_{ij} were not identically equal to zero (see (5.35)) implying that the corresponding RVEs are not perfectly isotropic. By way of example, the elastic constitutive matrix for an (8,8)-polymer composite is

$$\mathbf{C} = \begin{bmatrix} 5.3700 & 2.9938 & 2.9939 & 0.0015 & 0.0027 & 0.0046 \\ 2.9938 & 5.3751 & 2.9943 & 0.0012 & 0.0011 & 0.0032 \\ 2.9939 & 2.9943 & 5.3747 & 0.0013 & 0.0003 & 0.0011 \\ 0.0015 & 0.0012 & 0.0013 & 2.4121 & 0.0032 & 0.0003 \\ 0.0027 & 0.0011 & 0.0003 & 0.0032 & 2.4111 & 0.0014 \\ 0.0046 & 0.0032 & 0.0011 & 0.0003 & 0.0014 & 2.4114 \end{bmatrix}. \quad (5.45)$$

Nevertheless, the off-diagonal terms in the 4th, 5th and 6th rows and columns are about three orders of magnitude lower than the other entries. Moreover, since the matrix is symmetric and the diagonal entries in top-left and right-bottom blocks are close to each others, it is reasonable to assume that the RVE is isotropic. The two Lamé constants are therefore calculated as

$$\lambda^c = \frac{C_{12}^c + C_{13}^c + C_{23}^c}{3} \quad \text{and} \quad \mu^c = \frac{C_{44}^c + C_{55}^c + C_{66}^c}{3}, \quad (5.46)$$

and the Young's modulus E^c and shear modulus G^c are derived from (5.32).

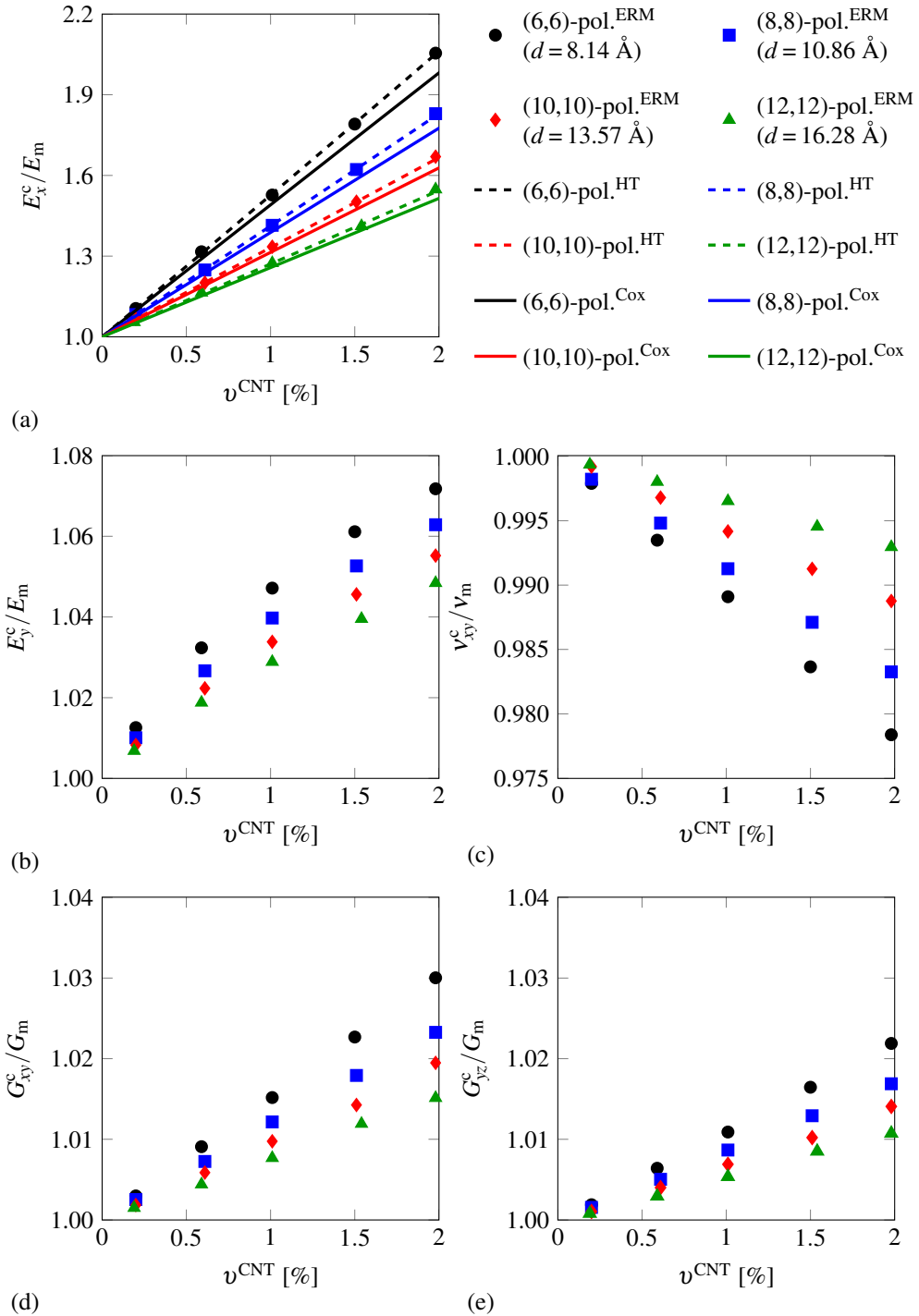


Figure 5.16: Normalized elastic properties (a) E_x^c , (b) E_y^c , (c) v_{xy}^c , (d) G_{xy}^c and (e) G_{yz}^c for (n,n) -polymer composites with unidirectional CNTs. For the case of E_x^c , results are in good agreement with those obtained with the Halpin-Tsai (HT) and Cox micromechanical models.

As shown in Figures 5.17a-b, also for RVEs with randomly oriented CNTs, E^c and G^c linearly increase with v^{CNT} . Compared with the case where CNTs are perfectly aligned along the x direction, the improvement in the elastic properties is lower while the opposite is observed for the shear modulus (similar results were derived numerically in [72]). Here, the estimated values of E^c and G^c provided by the Krenchel and Tsai-Pagano models are far from those obtained with FEM simulations. Surprisingly, the trend of E^c obtained with the Krenchel model is the opposite of the expected one: this is a consequence of the low Young's modulus of the interphase region (for higher values the usual trend would be observed). On the contrary, the Pan model provides a good estimate. Moreover, the numerical results are within the Hashin-Shtrikman bounds.

5.5.4 Size effects

Figure 5.16 shows that in unidirectional CNT-polymer composites an overall reinforcement effect is noticed decreasing the diameter of the embedded nanotubes: E_{xx}^c , E_{yy}^c , G_{xy}^c and G_{yz}^c decrease with d . The opposite trend is observed for ν_{xy}^c . Similarly, in CNT-polymer composites with randomly oriented fibers (see Figure 5.17), E^c and G^c increase by decreasing the diameter of the nanotubes. In both cases, the reinforcement effect provided by (6, 6) CNTs on the mechanical properties of the pure polymer matrix is typically twice of that offered by (12, 12) CNTs.

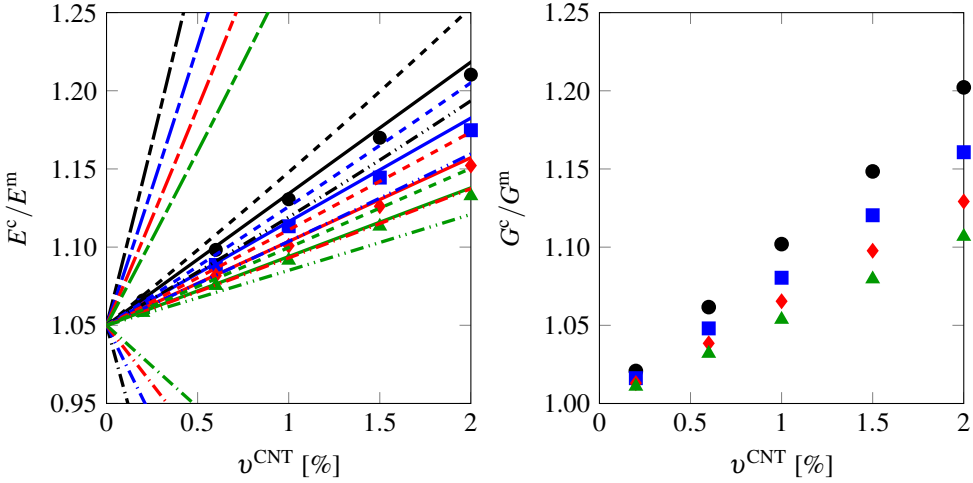
Therefore, as discussed in Section 5.3, the role played by the interphase volume fraction on the composite mechanical properties is crucial. Although the stiffness of the interphase increase with d (Figure 5.9), those of the corresponding composites increase by decreasing d (Figures 5.16 and 5.17).

5.6 Summary and concluding remarks

The computational procedure proposed in this work hinges on the characterization of the roles played by the various phases of a CNT-polymer composite on its mechanical response.

The atomistic simulations of a generic polymer matrix embedding an uncapped non-functionalized single-walled CNT in Section 5.2 have been fundamental for the geometrical characterization of the different phases (i.e., single-walled CNT, interface, interphase and bulk polymer) and for the definition of their roles in the mechanical response of the composite. This task addressed a crucial issue concerning nanocomposites: the separate reinforcement effect of the CNT and the interphase [62]. The results of our simulations reveals that the reinforcement in the nonfunctionalized CNT-polymer composites is solely exerted by the interphase. Despite the simplicity and generality of the atomistic polymer model, our results are supported by literature findings on some real nonfunctionalized CNT-polymer composites obtained through experiments [18, 27, 35, 67, 76, 77] and numerical simulations [16, 26, 36, 82].

This characterization justified the FEM model proposed in Section 5.3 that, at variance with previous contributions [16, 50, 56, 68, 75], does not take into account the embedded CNT and the interface. The elastic properties of the interphase were determined through a parameter identification procedure by comparing the mechanical response of the atomistic model and a mechanically equivalent intermediate continuum micromechanical model. Not



(a)

(b)

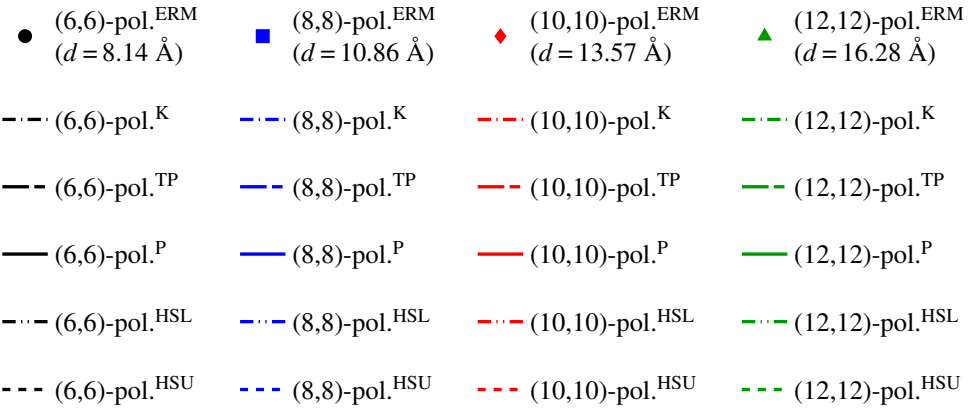


Figure 5.17: Normalized elastic properties (a) E^c and (b) G^c for (n,n) -polymer-polymer composites with randomly oriented CNTs. Results for the Young's modulus E^c of the composite are compared to those obtained with the Krenchel (K), Tsai-Pagano (TP), Pan (P) micromechanical models and the Hashin-Shtrikman upper (HSU) and lower (HSL) bounds.

surprisingly, the stiffness of the interphase increases with the CNT diameter d since the ordering of the surrounding polymer layer improves with increasing values of d [26, 52].

Finally, the mechanical properties of the composite in Section 5.5 were calculated through the computational homogenization procedure described in Section 5.4. Different RVEs embedding one-dimensional discrete fibers, representing equivalent continuum CNT-induced interphases, have been generated. The ERM was employed to efficiently take into account the high number of fibers in the FEM simulations. The results show that the elastic properties can significantly increase when the nanotubes diameter decreases, clearly indicating size-dependent effective elastic properties.

Due to the generality of the model for the polymer chains, it is difficult, and beyond the scope of the paper, to quantitatively compare the estimated macroscopic elastic properties with literature findings on real CNT-polymer composites. Nevertheless, similarities with experimental results on composites showing CNT-nucleated crystallization can be found. For instance, Coleman and coworkers [18, 65] observed that Young's modulus and crystallinity in CNT-polyvinyl alcohol linearly increase with ν_{CNT} as observed in the present study. Hegde et al. [35] also noticed a linear increase in the Young's modulus with the CNT diameter d . Moreover, some experiments on CNT-polymer composites [13, 35, 65] showed that the stiffness does not increase after a certain value of ν_{CNT} . This might suggest full crystallization of the polymer matrix and supports, as discussed in Section 5.2.4, the relevant role of the interphase beside the negligible one of the interface for composites with nonfunctionalized CNTs.

5.A Periodic boundary conditions for three-dimensional RVE

For the RVE in Figure 5.18 with dimensions L_x , L_y and L_z , the periodic boundary conditions [66] can be stated as

$$u_i^k - u_i^l = \bar{\epsilon}_{ij}L_j \quad (5.47)$$

where u_i^k and u_i^l are the displacements in i -direction on the two opposite boundaries denoted by indexes k and l while $\bar{\epsilon}_{ij}$ is the imposed macrostrain tensor. Therefore, with reference to Figures 5.18b-d, the periodic boundary conditions for a generic macrostrain can be explicitly written for all faces:

$$u_x^1 = u_x^3 + \bar{\epsilon}_{xx}L_x, \quad (5.48a) \quad u_x^2 = u_x^4 + \bar{\epsilon}_{xy}L_y, \quad (5.49a) \quad u_x^6 = u_x^5 + \bar{\epsilon}_{xz}L_z, \quad (5.50a)$$

$$u_y^1 = u_y^3 + \bar{\epsilon}_{yx}L_x, \quad (5.48b) \quad u_y^2 = u_y^4 + \bar{\epsilon}_{yy}L_y, \quad (5.49b) \quad u_y^6 = u_y^5 + \bar{\epsilon}_{yz}L_z, \quad (5.50b)$$

$$u_z^1 = u_z^3 + \bar{\epsilon}_{zx}L_x, \quad (5.48c) \quad u_z^2 = u_z^4 + \bar{\epsilon}_{zy}L_y, \quad (5.49c) \quad u_z^6 = u_z^5 + \bar{\epsilon}_{zz}L_z, \quad (5.50c)$$

edges:

$$u_x^2 = u_x^3 + \bar{\epsilon}_{xx}L_x, \quad (5.51a) \quad u_x^3 = u_x^4 + \bar{\epsilon}_{xy}L_y, \quad (5.52a) \quad u_x^1 = u_x^4 + \bar{\epsilon}_{xx}L_x, \quad (5.53a)$$

$$u_y^2 = u_y^3 + \bar{\epsilon}_{yx}L_x, \quad (5.51b) \quad u_y^3 = u_y^4 + \bar{\epsilon}_{yy}L_y, \quad (5.52b) \quad u_y^1 = u_y^4 + \bar{\epsilon}_{yx}L_x, \quad (5.53b)$$

$$u_z^2 = u_z^3 + \bar{\epsilon}_{zx}L_x, \quad (5.51c) \quad u_z^3 = u_z^4 + \bar{\epsilon}_{zy}L_y, \quad (5.52c) \quad u_z^1 = u_z^4 + \bar{\epsilon}_{zx}L_x, \quad (5.53c)$$

$$u_x^6 = u_x^7 + \bar{\epsilon}_{xx}L_x, \quad (5.54a) \quad u_x^7 = u_x^8 + \bar{\epsilon}_{xy}L_z, \quad (5.55a) \quad u_x^5 = u_x^8 + \bar{\epsilon}_{xx}L_x, \quad (5.56a)$$

$$u_y^6 = u_y^7 + \bar{\epsilon}_{yx}L_x, \quad (5.54b) \quad u_y^7 = u_y^8 + \bar{\epsilon}_{yy}L_z, \quad (5.55b) \quad u_y^5 = u_y^8 + \bar{\epsilon}_{yx}L_x, \quad (5.56b)$$

$$u_z^6 = u_z^7 + \bar{\epsilon}_{zx}L_x, \quad (5.54c) \quad u_z^7 = u_z^8 + \bar{\epsilon}_{zy}L_z, \quad (5.55c) \quad u_z^5 = u_z^8 + \bar{\epsilon}_{zx}L_x, \quad (5.56c)$$

$$u_x^{11} = u_x^{10} + \bar{\epsilon}_{xz}L_z, \quad (5.57a) \quad u_x^{11} = u_x^{12} + \bar{\epsilon}_{xy}L_y, \quad (5.58a) \quad u_x^{12} = u_x^9 + \bar{\epsilon}_{xz}L_z, \quad (5.59a)$$

$$u_y^{11} = u_y^{10} + \bar{\epsilon}_{yz}L_z, \quad (5.57b) \quad u_y^{11} = u_y^{12} + \bar{\epsilon}_{yy}L_y, \quad (5.58b) \quad u_y^{12} = u_y^9 + \bar{\epsilon}_{yz}L_z, \quad (5.59b)$$

$$u_z^{11} = u_z^{10} + \bar{\epsilon}_{zz}L_z, \quad (5.57c) \quad u_z^{11} = u_z^{12} + \bar{\epsilon}_{zy}L_y, \quad (5.58c) \quad u_z^{12} = u_z^9 + \bar{\epsilon}_{zz}L_z, \quad (5.59c)$$

and vertices:

$$u_x^2 = u_x^1 + \bar{\epsilon}_{xy}L_y, \quad (5.60a) \quad u_x^3 = u_x^2 + \bar{\epsilon}_{xz}L_z, \quad (5.61a) \quad u_x^3 = u_x^4 + \bar{\epsilon}_{xy}L_y, \quad (5.62a)$$

$$u_y^2 = u_y^1 + \bar{\epsilon}_{yy}L_y, \quad (5.60b) \quad u_y^3 = u_y^2 + \bar{\epsilon}_{yz}L_z, \quad (5.61b) \quad u_y^3 = u_y^4 + \bar{\epsilon}_{yy}L_y, \quad (5.62b)$$

$$u_z^2 = u_z^1 + \bar{\epsilon}_{zy}L_y, \quad (5.60c) \quad u_z^3 = u_z^2 + \bar{\epsilon}_{zz}L_z, \quad (5.61c) \quad u_z^3 = u_z^4 + \bar{\epsilon}_{zy}L_y, \quad (5.62c)$$

$$u_x^7 = u_x^8 + \bar{\epsilon}_{xy}L_y, \quad (5.63a) \quad u_x^7 = u_x^6 + \bar{\epsilon}_{xz}L_z, \quad (5.64a) \quad u_x^6 = u_x^5 + \bar{\epsilon}_{xy}L_y, \quad (5.65a)$$

$$u_y^7 = u_y^8 + \bar{\epsilon}_{yy}L_y, \quad (5.63b) \quad u_y^7 = u_y^6 + \bar{\epsilon}_{yz}L_z, \quad (5.64b) \quad u_y^6 = u_y^5 + \bar{\epsilon}_{yy}L_y, \quad (5.65b)$$

$$u_z^7 = u_z^8 + \bar{\epsilon}_{zy}L_y, \quad (5.63c) \quad u_z^7 = u_z^6 + \bar{\epsilon}_{zz}L_z, \quad (5.64c) \quad u_z^6 = u_z^5 + \bar{\epsilon}_{zy}L_y, \quad (5.65c)$$

$$u_x^4 = u_x^8 + \bar{\epsilon}_{xx}L_x, \quad (5.66a)$$

$$u_y^4 = u_y^8 + \bar{\epsilon}_{yx}L_x, \quad (5.66b)$$

$$u_z^4 = u_z^8 + \bar{\epsilon}_{zx}L_x. \quad (5.66c)$$

If the RVE is symmetric with respect to the xy , xz and yz planes, displacements on opposite faces are such that

$$u_x^1 = -u_x^3, \quad (5.67a)$$

$$u_y^2 = -u_y^4, \quad \text{and} \quad (5.67b)$$

$$u_z^5 = -u_z^6. \quad (5.67c)$$

Substituting (5.67a)-(5.67c) in (5.48a), (5.49b) and (5.50c), respectively, for $\bar{\epsilon} = [\bar{\epsilon}_{xx} \ 0 \ 0 \ 0 \ 0 \ 0]^T$ yields

$$u_x^1 = -u_x^3 = \bar{\epsilon}_{xx} \frac{L_x}{2}, \quad (5.68a)$$

$$u_y^2 = u_y^4 = 0, \quad \text{and} \quad (5.68b)$$

$$u_z^5 = u_z^6 = 0. \quad (5.68c)$$

This implies that the displacements orthogonal to faces 4, 6, 2 and 5 are null. Therefore, with reference to the equivalent continuum model in discussed in Section 5.3, derivation of the boundary conditions in Figure 5.7b is straightforward.

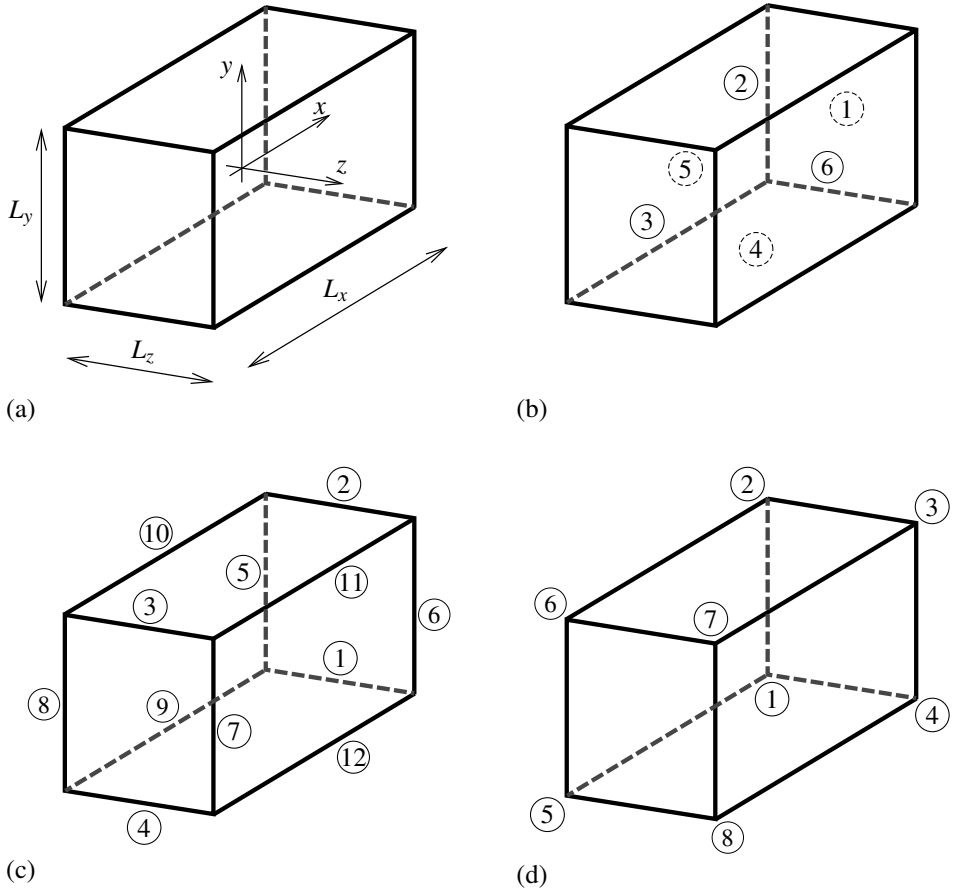


Figure 5.18: (a) Schematic representation of a three-dimensional RVE and numbering of (b) faces, (c) edges and (d) vertices.

Direction	Degree	Knot vector
ξ	$p = 1$	$\Xi = [0, 0, 1, 1]$
η	$q = 2$	$\mathcal{H} = [0, 0, 0, 1, 1, 1]$
ζ	$r = 1$	$\mathcal{L} = [0, 0, 1, 1]$

Table 5.6: NURBS degree and knot vectors used for the five NURBS patches in Figure 5.7.

j	k	$B_{1,j,k}$	$w_{1,j,k}$	$B_{2,j,k}$	$w_{2,j,k}$
1	1	$(0, B, 0)$	1	$(\frac{l}{2}, B, 0)$	1
2	1	$(0, \frac{B}{2}, \frac{B}{2})$	1	$(\frac{l}{2}, \frac{B}{2}, \frac{B}{2})$	1
3	1	$(0, 0, B)$	1	$(\frac{l}{2}, 0, B)$	1
1	2	$(0, r^f, 0)$	1	$(\frac{l}{2}, r^f, 0)$	1
2	2	$(0, r^f \cos \frac{\pi}{4}, r^f \sin \frac{\pi}{4})$	$\frac{1}{\sqrt{2}}$	$(\frac{l}{2\sqrt{2}}, r^f \cos \frac{\pi}{4}, r^f \sin \frac{\pi}{4})$	$\frac{1}{\sqrt{2}}$
3	2	$(0, 0, r^f)$	1	$(\frac{l}{2}, 0, r^f)$	1

Table 5.7: Control points and weights of the NURBS patch 1 (see Figure 5.7c).

5.B Control data for the NURBS continuum equivalent model

The knot vectors and control points required for the multi-patch NURBS solid shown in Figure 5.7 are reported in Table 5.6 and Tables 5.7-5.11, respectively.

Bibliography

- [1] S.G. Advani and C.L. Tucker III. The use of tensors to describe and predict fiber orientation in short fiber composites. *Journal of Rheology*, 31(8):751–784, 1987.

j	k	$B_{1,j,k}$	$w_{1,j,k}$	$B_{2,j,k}$	$w_{2,j,k}$
1	1	$(0, r^f, 0)$	1	$(\frac{l}{2}, r^f, 0)$	1
2	1	$(0, r^f \cos \frac{\pi}{4}, r^f \sin \frac{\pi}{4})$	$\frac{1}{\sqrt{2}}$	$(\frac{l}{2}\sqrt{2}, r^f \cos \frac{\pi}{4}, r^f \sin \frac{\pi}{4})$	$\frac{1}{\sqrt{2}}$
3	1	$(0, 0, r^f)$	1	$(\frac{l}{2}, 0, r^f)$	1
1	2	$(0, r^i, 0)$	1	$(\frac{l}{2}, r^i, 0)$	1
2	2	$(0, r^i \cos \frac{\pi}{4}, r^i \sin \frac{\pi}{4})$	$\frac{1}{\sqrt{2}}$	$(\frac{l}{2}\sqrt{2}, r^i \cos \frac{\pi}{4}, r^i \sin \frac{\pi}{4})$	$\frac{1}{\sqrt{2}}$
3	2	$(0, 0, r^i)$	1	$(\frac{l}{2}, 0, r^i)$	1

Table 5.8: Control points and weights of the NURBS patch 2 (see Figure 5.7c).

j	k	$B_{1,j,k}$	$w_{1,j,k}$	$B_{2,j,k}$	$w_{2,j,k}$
1	1	$(\frac{l}{2}, B, 0)$	1	$(\frac{L_x}{2}, B, 0)$	1
2	1	$(\frac{l}{2}, \frac{B}{2}, \frac{B}{2})$	1	$(\frac{L_x}{2}, \frac{B}{2}, \frac{B}{2})$	1
3	1	$(\frac{l}{2}, 0, B)$	1	$(\frac{L_x}{2}, 0, B)$	1
1	2	$(\frac{l}{2}, r^f, 0)$	1	$(\frac{L_x}{2}, r^f, 0)$	1
2	2	$(\frac{l}{2}\sqrt{2}, r^f \cos \frac{\pi}{4}, r^f \sin \frac{\pi}{4})$	$\frac{1}{\sqrt{2}}$	$(\frac{L_x}{2}\sqrt{2}, r^f \cos \frac{\pi}{4}, r^f \sin \frac{\pi}{4})$	$\frac{1}{\sqrt{2}}$
3	2	$(\frac{l}{2}, 0, r^f)$	1	$(\frac{L_x}{2}, 0, r^f)$	1

Table 5.9: Control points and weights of the NURBS patch 3 (see Figure 5.7c).

j	k	$B_{1,j,k}$	$w_{1,j,k}$	$B_{2,j,k}$	$w_{2,j,k}$
1	1	$(\frac{l}{2}, r^i, 0)$	1	$(\frac{L_x}{2}, r^i, 0)$	1
2	1	$(\frac{l}{2}\sqrt{2}, r^i \cos \frac{\pi}{4}, r^i \sin \frac{\pi}{4})$	$\frac{1}{\sqrt{2}}$	$(\frac{L_x}{2}\sqrt{2}, r^i \cos \frac{\pi}{4}, r^i \sin \frac{\pi}{4})$	$\frac{1}{\sqrt{2}}$
3	1	$(\frac{l}{2}, 0, r^i)$	1	$(\frac{L_x}{2}, 0, r^i)$	1
1	2	$(\frac{l}{2}, r^f, 0)$	1	$(\frac{L_x}{2}, r^f, 0)$	1
2	2	$(\frac{l}{2}\sqrt{2}, r^f \cos \frac{\pi}{4}, r^f \sin \frac{\pi}{4})$	$\frac{1}{\sqrt{2}}$	$(\frac{L_x}{2}\sqrt{2}, r^f \cos \frac{\pi}{4}, r^f \sin \frac{\pi}{4})$	$\frac{1}{\sqrt{2}}$
3	2	$(\frac{l}{2}, 0, r^f)$	1	$(\frac{L_x}{2}, 0, r^f)$	1

Table 5.10: Control points and weights of the NURBS patch 4 (see Figure 5.7c).

j	k	$B_{1,j,k}$	$w_{1,j,k}$	$B_{2,j,k}$	$w_{2,j,k}$
1	1	$(\frac{l}{2}, 0, 0)$	1	$(\frac{L_x}{2}, 0, 0)$	1
2	1	$(\frac{l}{2}\sqrt{2}, 0, 0)$	$\frac{1}{\sqrt{2}}$	$(\frac{L_x}{2}\sqrt{2}, 0, 0)$	$\frac{1}{\sqrt{2}}$
3	1	$(\frac{l}{2}, 0, 0)$	1	$(\frac{L_x}{2}, 0, 0)$	1
1	2	$(\frac{l}{2}, r^i, 0)$	1	$(\frac{L_x}{2}, r^i, 0)$	1
2	2	$(\frac{l}{2}, r^i \cos \frac{\pi}{4}, r^i \sin \frac{\pi}{4})$	$\frac{1}{\sqrt{2}}$	$(\frac{L_x}{2}\sqrt{2}, r^i \cos \frac{\pi}{4}, r^i \sin \frac{\pi}{4})$	$\frac{1}{\sqrt{2}}$
3	2	$(\frac{l}{2}, 0, 0)$	1	$(\frac{L_x}{2}, 0, 0)$	1

Table 5.11: Control points and weights of the NURBS patch 5 (see Figure 5.7c).

- [2] J.C. Halpin Affdl and J.L. Kardos. The Halpin-Tsai equations: A review. *Polymer Engineering & Science*, 16(5):344–352, 1976.
- [3] P.M. Ajayan, L.S. Schadler, C. Giannaris, and A. Rubio. Single-walled carbon nanotube–polymer composites: Strength and weakness. *Advanced Materials*, 12(10):750–753, 2000.
- [4] B. Arash, Q. Wang, and V.K. Varadan. Mechanical properties of carbon nanotube/polymer composites. *Scientific Reports*, 4, 2014.
- [5] S. Balakrishnan and D. W. Murray. Finite element prediction of reinforced concrete behavior. Technical Report No. 138 (Structural Engineering), Department of Civil Engineering, The University of Alberta, July 1986.
- [6] A.H. Barber, S.R. Cohen, and H.D. Wagner. Measurement of carbon nanotube–polymer interfacial strength. *Applied Physics Letters*, 82(23):4140–4142, 2003.
- [7] A.H. Barber, S.R. Cohen, S. Kenig, and H.D. Wagner. Interfacial fracture energy measurements for multi-walled carbon nanotubes pulled from a polymer matrix. *Composites Science and Technology*, 64(15):2283–2289, 2004.
- [8] T. Belytschko, S.P. Xiao, G.C. Schatz, and R.S. Ruoff. Atomistic simulations of nanotube fracture. *Physical Review B*, 65(23):235430, 2002.
- [9] H. J. Böhm, A. Eckschlager, and W. Han. Multi-inclusion unit cell models for metal matrix composites with randomly oriented discontinuous reinforcements. *Computational Materials Science*, 25(1):42–53, 2002.
- [10] D.I. Bower. *An Introduction to Polymer Physics*. Cambridge University Press, 2002.
- [11] D.W. Brenner. Empirical potential for hydrocarbons for use in simulating the chemical vapor deposition of diamond films. *Physical Review B*, 42(15):9458, 1990.
- [12] D. Brown, V. Marcadon, P. Mele, and N.D. Alberola. Effect of filler particle size on the properties of model nanocomposites. *Macromolecules*, 41(4):1499–1511, 2008.
- [13] T.E. Chang, L.R. Jensen, A. Kisliuk, R.B. Pipes, R. Pyrz, and A.P. Sokolov. Microscopic mechanism of reinforcement in single-wall carbon nanotube/polypropylene nanocomposite. *Polymer*, 46(2):439–444, 2005.
- [14] X. Chen, L. Zhang, M. Zheng, C. Park, X. Wang, and C. Ke. Quantitative nanomechanical characterization of the van der waals interfaces between carbon nanotubes and epoxy. *Carbon*, 82:214–228, 2015.
- [15] J. Choi, H. Shin, S. Yang, and M. Cho. The influence of nanoparticle size on the mechanical properties of polymer nanocomposites and the associated interphase region: A multiscale approach. *Composite Structures*, 119:365–376, 2015.
- [16] J. Choi, H. Shin, and M. Cho. A multiscale mechanical model for the effective interphase of SWNT/epoxy nanocomposite. *Polymer*, 89:159–171, 2016.

- [17] T.C. Clancy and T.S. Gates. Modeling of interfacial modification effects on thermal conductivity of carbon nanotube composites. *Polymer*, 47(16):5990–5996, 2006.
- [18] J.N. Coleman, M. Cadek, K.P. Ryan, A. Fonseca, J.B. Nagy, W.J. Blau, and M.S. Ferreira. Reinforcement of polymers with carbon nanotubes. The role of an ordered polymer interfacial region. Experiment and modeling. *Polymer*, 47(26):8556–8561, 2006.
- [19] C.A. Cooper, S. Cohen, A.H. Barber, and H.D. Wagner. Detachment of nanotubes from a polymer matrix. *Applied Physics Letters*, 81(20):3873–3875, 2002.
- [20] B. Coto, I. Antia, J. Barriga, M. Blanco, and J.-S. Sarasua. Influence of the geometrical properties of the carbon nanotubes on the interfacial behavior of epoxy/CNT composites: A molecular modelling approach. *Computational Materials Science*, 79:99–104, 2013.
- [21] H.L. Cox. The elasticity and strength of paper and other fibrous materials. *British Journal of Applied Physics*, 3(3):72–79, 1952.
- [22] V. M. C. F. Cunha, J. A. O. Barros, and J. M. Sena-Cruz. A finite element model with discrete embedded elements for fibre reinforced composites. *Computers & structures*, 94:22–33, 2012.
- [23] M.S. Dresselhaus, G. Dresselhaus, P.C. Eklund, and A.M. Rao. *Carbon Nanotubes*. Springer, 2000.
- [24] A.E. Elwi and T.M. Hruday. Finite element model for curved embedded reinforcement. *Journal of Engineering Mechanics*, 115(4):740–754, 1989.
- [25] C. De Falco, A. Reali, and R. Vázquez. GeoPDEs: A research tool for Isogeometric Analysis of PDEs. *Advances in Engineering Software*, 42(12):1020–1034, 2011.
- [26] S.G. Falkovich, S.V. Larin, A.V. Lyulin, V.E. Yudin, J.M. Kenny, and S.V. Lyulin. Influence of the carbon nanofiller surface curvature on the initiation of crystallization in thermoplastic polymers. *RSC Advances*, 4(89):48606–48612, 2014.
- [27] B. Fragneaud, K. Masenelli-Varlot, A. Gonzalez-Montiel, M. Terrones, and J.-Y. Cavaillé. Mechanical behavior of polystyrene grafted carbon nanotubes/polystyrene nanocomposites. *Composites Science and Technology*, 68(15):3265–3271, 2008.
- [28] S. J. V. Frankland, V. M. Harik, G. M. Odegard, D. W. Brenner, and T. S. Gates. The stress-strain behavior of polymer-nanotube composites from molecular dynamics simulation. *Composites Science and Technology*, 63(11):1655–1661, 2003.
- [29] A.A. Gusev, P.J. Hine, and I.M. Ward. Fiber packing and elastic properties of a transversely random unidirectional glass/epoxy composite. *Composites Science and Technology*, 60(4):535–541, 2000.
- [30] C.M. Hadden, B.D. Jensen, A. Bandyopadhyay, G.M. Odegard, A. Koo, and R. Liang. Molecular modeling of EPON-862/graphite composites: Interfacial characteristics for multiple crosslink densities. *Composites Science and Technology*, 76:92–99, 2013.

- [31] S. Haghghatpanah and K. Bolton. Molecular-level computational studies of single wall carbon nanotube–polyethylene composites. *Computational Materials Science*, 69: 443–454, 2013.
- [32] Y. Han and J. Elliott. Molecular dynamics simulations of the elastic properties of polymer/carbon nanotube composites. *Computational Materials Science*, 39(2):315–323, 2007.
- [33] Z. Hashin. Analysis of composite materials—a survey. *Journal of Applied Mechanics*, 50(3):481–505, 1983.
- [34] Z. Hashin and S. Shtrikman. On some variational principles in anisotropic and nonhomogeneous elasticity. *Journal of the Mechanics and Physics of Solids*, 10(4):335–342, 1962.
- [35] M. Hegde, U. Lafont, B. Norder, S.J. Picken, E.T. Samulski, M. Rubinstein, and T. Dingemans. SWCNT induced crystallization in an amorphous all-aromatic poly(ether imide). *Macromolecules*, 46(4):1492–1503, 2013.
- [36] S. Herasati, L.C. Zhang, and H.H. Ruan. A new method for characterizing the interphase regions of carbon nanotube composites. *International Journal of Solids and Structures*, 51(9):1781–1791, 2014.
- [37] R. Hill. Elastic properties of reinforced solids: Some theoretical principles. *Journal of the Mechanics and Physics of Solids*, 11(5):357–372, 1963.
- [38] Y. Huang, J. Wu, and K.-C. Hwang. Thickness of graphene and single-wall carbon nanotubes. *Physical Review B*, 74(24):245413, 2006.
- [39] T.J.R. Hughes, J.A. Cottrell, and Y. Bazilevs. Isogeometric analysis: CAD, finite elements, NURBS, exact geometry and mesh refinement. *Computer Methods in Applied Mechanics and Engineering*, 194(39):4135–4195, 2005.
- [40] C. L. Tucker III and E. Liang. Stiffness predictions for unidirectional short-fiber composites: Review and evaluation. *Composites Science and Technology*, 59(5):655–671, 1999.
- [41] T. Kanit, S. Forest, I. Galliet, V. Mounoury, and D. Jeulin. Determination of the size of the representative volume element for random composites: Statistical and numerical approach. *International Journal of Solids and Structures*, 40(13):3647–3679, 2003.
- [42] S. Kari, H. Berger, and U. Gabbert. Numerical evaluation of effective material properties of randomly distributed short cylindrical fibre composites. *Computational Materials Science*, 39(1):198–204, 2007.
- [43] K. Kremer and G.S. Grest. Dynamics of entangled linear polymer melts: A molecular-dynamics simulation. *The Journal of Chemical Physics*, 92(8):5057–5086, 1990.
- [44] H. Krenchel. *Fibre reinforcement: Theoretical and practical investigations of the elasticity and strength of fibre-reinforced materials*. Akademisk forlag, 1964.

- [45] E.D. Laird and C.Y. Li. Structure and morphology control in crystalline polymer-carbon nanotube nanocomposites. *Macromolecules*, 46(8):2877–2891, 2013.
- [46] M. Lan and H. Waisman. Mechanics of SWCNT aggregates studied by incremental constrained minimization. *Journal of Nanomechanics and Micromechanics*, 2(2):15–22, 2011.
- [47] S.V. Larin, S.G. Falkovich, V.M. Nazarychev, A.A. Gurtovenko, A.V. Lyulin, and S.V. Lyulin. Molecular-dynamics simulation of polyimide matrix pre-crystallization near the surface of a single-walled carbon nanotube. *RSC Advances*, 4(2):830–844, 2014.
- [48] Y. Lee, S. Lee, J. Youn, K. Chung, and T. Kang. Characterization of fiber orientation in short fiber reinforced composites with an image processing technique. *Materials Research Innovations*, 6(2):65–72, 2002.
- [49] Y. Li, Y. Liu, X. Peng, C. Yan, S. Liu, and N. Hu. Pull-out simulations on interfacial properties of carbon nanotube-reinforced polymer nanocomposites. *Computational Materials Science*, 50(6):1854–1860, 2011.
- [50] Y. J. Liu, N. Nishimura, D. Qian, N. Adachi, Y. Otani, and V. Mokashi. A boundary element method for the analysis of CNT/polymer composites with a cohesive interface model based on molecular dynamics. *Engineering Analysis with Boundary Elements*, 32(4):299–308, 2008.
- [51] M. Malagù, E. Benvenuti, and A. Simone. One-dimensional nonlocal elasticity for tensile single-walled carbon nanotubes: A molecular structural mechanics characterization. *European Journal of Mechanics-A/Solids*, 54:160–170, 2015.
- [52] M. Malagù, A. Lyulin, E. Benvenuti, and A. Simone. A molecular-dynamics study of size and chirality effects on glass-transition temperature and ordering in carbon nanotube-polymer composites. *Macromolecular Theory and Simulations*, 25(6):571–581, 2016. doi: <http://dx.doi.org/10.1002/mats.201600041>.
- [53] G.W. Milton. The theory of composites. *The Theory of Composites*, 2002.
- [54] V.V. Mokashi, D. Qian, and Y. Liu. A study on the tensile response and fracture in carbon nanotube-based composites using molecular mechanics. *Composites Science and Technology*, 67(3):530–540, 2007.
- [55] J. Nocedal and S. J. Wright. *Numerical Optimization*. Springer, 2006.
- [56] G.M. Odegard, T.S. Gates, K.E. Wise, C. Park, and E.J. Siochi. Constitutive modeling of nanotube-reinforced polymer composites. *Composites Science and Technology*, 63(11):1671–1687, 2003.
- [57] M. Ostoja-Starzewski. Microstructural randomness versus representative volume element in thermomechanics. *Journal of Applied Mechanics*, 69(1):25–35, 2002.
- [58] N. Pan. The elastic constants of randomly oriented fiber composites: A new approach to prediction. *Science and Engineering of Composite Materials*, 5(2):63–72, 1996.

- [59] D. V. Phillips and O. C. Zienkiewicz. Finite element non-linear analysis of concrete structures. *Proceedings of the Institution of Civil Engineers. Part 2*, 61:59–88, 1976.
- [60] R. B. Pipes, S. J. V. Frankland, P. Hubert, and E. Saether. Self-consistent properties of carbon nanotubes and hexagonal arrays as composite reinforcements. *Composites Science and Technology*, 63(10):1349–1358, 2003.
- [61] S. Plimpton. Fast parallel algorithms for short-range molecular dynamics. *Journal of Computational Physics*, 117(1):1–19, 1995.
- [62] B. Pukánszky. Interfaces and interphases in multicomponent materials: Past, present, future. *European Polymer Journal*, 41(4):645–662, 2005.
- [63] D. Qian and E.C. Dickey. In-situ transmission electron microscopy studies of polymer-carbon nanotube composite deformation. *Journal of Microscopy*, 204(1):39–45, 2001.
- [64] D. Qian, E.C. Dickey, R. Andrews, and T. Rantell. Load transfer and deformation mechanisms in carbon nanotube-polystyrene composites. *Applied Physics Letters*, 76(20):2868–2870, 2000.
- [65] K. P. Ryan, M. Cadek, V. Nicolosi, D. Blond, M. Ruether, G. Armstrong, H. Swan, A. Fonseca, J. B. Nagy, W. K. Maser, W. J. Blau, and J. N. Coleman. Carbon nanotubes for reinforcement of plastics? A case study with poly (vinyl alcohol). *Composites Science and Technology*, 67(7):1640–1649, 2007.
- [66] E. Sanchez-Palencia and A. Zaou. *Homogenization Techniques for Composite Media*. Springer-Verlag, 1987.
- [67] L.S. Schadler, S.C. Giannaris, and P.M. Ajayan. Load transfer in carbon nanotube epoxy composites. *Applied Physics Letters*, 73(26):3842–3844, 1998.
- [68] M. M. Shokrieh and R. Rafiee. Investigation of nanotube length effect on the reinforcement efficiency in carbon nanotube based composites. *Composite Structures*, 92(10):2415–2420, 2010.
- [69] S. Singh and A. K. Mohanty. Wood fiber reinforced bacterial bioplastic composites: Fabrication and performance evaluation. *Composites Science and Technology*, 67(9):1753–1763, 2007.
- [70] D.N. Theodorou and U.W. Suter. Detailed molecular structure of a vinyl polymer glass. *Macromolecules*, 18(7):1467–1478, 1985.
- [71] W. Tian, L. Qi, J. Zhou, J. Liang, and Y. Ma. Representative volume element for composites reinforced by spatially randomly distributed discontinuous fibers and its applications. *Composite Structures*, 131:366–373, 2015.
- [72] W. Tian, L. Qi, C. Su, J. Zhou, and Z. Jing. Numerical simulation on elastic properties of short-fiber-reinforced metal matrix composites: Effect of fiber orientation. *Composite Structures*, 152:408–417, 2016.

- [73] S. W. Tsai and N. J. Pagano. Invariant properties of composite materials. Technical report, DTIC Document, 1968.
- [74] K. I. Tserpes, P. Papanikos, G. Labeas, and S. G. Pantelakis. Multi-scale modeling of tensile behavior of carbon nanotube-reinforced composites. *Theoretical and Applied Fracture Mechanics*, 49(1):51–60, 2008.
- [75] H. Wan, F. Delale, and L. Shen. Effect of CNT length and CNT-matrix interphase in carbon nanotube (CNT) reinforced composites. *Mechanics Research Communications*, 32(5):481–489, 2005.
- [76] S. Wang, R. Liang, B. Wang, and C. Zhang. Load-transfer in functionalized carbon nanotubes/polymer composites. *Chemical Physics Letters*, 457(4):371–375, 2008.
- [77] P.C.P. Watts and W.K. Hsu. Behaviours of embedded carbon nanotubes during film cracking. *Nanotechnology*, 14(5):L7, 2003.
- [78] D. Weidt and Ł. Figiel. Effect of CNT waviness and van der Waals interaction on the nonlinear compressive behaviour of epoxy/CNT nanocomposites. *Composites Science and Technology*, 115:52–59, 2015.
- [79] T. Werder, J.H. Walther, R.L. Jaffe, T. Halicioglu, and P. Koumoutsakos. On the water-carbon interaction for use in molecular dynamics simulations of graphite and carbon nanotubes. *The Journal of Physical Chemistry B*, 107(6):1345–1352, 2003.
- [80] J. M. Wernik, B. J. Cornwell-Mott, and S. A. Meguid. Determination of the interfacial properties of carbon nanotube reinforced polymer composites using atomistic-based continuum model. *International Journal of Solids and Structures*, 49(13):1852–1863, 2012.
- [81] B. Widom. Random sequential addition of hard spheres to a volume. *The Journal of Chemical Physics*, 44(10):3888–3894, 1966.
- [82] S. Yang, S. Yu, W. Kyoung, and D.-S. Han and M. Cho. Multiscale modeling of size-dependent elastic properties of carbon nanotube/polymer nanocomposites with interfacial imperfections. *Polymer*, 53(2):623–633, 2012.
- [83] S. Yang, S. Yu, J. Ryu, J.-M. Cho, W. Kyoung, D.-S. Han, and M. Cho. Nonlinear multiscale modeling approach to characterize elastoplastic behavior of cnt/polymer nanocomposites considering the interphase and interfacial imperfection. *International Journal of Plasticity*, 41:124–146, 2013.
- [84] Z.Q. Zhang, D.K. Ward, Y. Xue, H.W. Zhang, and M.F. Horstemeyer. Interfacial characteristics of carbon nanotube-polyethylene composites using molecular dynamics simulations. *ISRN Materials Science*, 2011, 2011.
- [85] R. Zhu, E. Pan, and A. K. Roy. Molecular dynamics study of the stress-strain behavior of carbon-nanotube reinforced Epon 862 composites. *Materials Science and Engineering: A*, 447(1):51–57, 2007.

Chapter 6

Conclusions and future perspective

The mechanical properties of carbon nanotubes are intimately linked to their structural features (diameter and chirality). When used as reinforcement in polymer-based composites, a change in their diameter leads to variations in the ordering and mechanical properties of the surrounding layer of polymer chains—the interphase—and consequently on the mechanical response of the composite. Therefore, the successful design of CNT-polymer composites requires a thorough understanding of nanotube-induced size effects both at the nanoscale and at the macroscale. In this context, this thesis proposes a computational framework that, by exploiting advanced numerical tools, allowed for the characterization of size effects in CNTs and CNT-polymer composites. Atomistic simulations are used for an accurate investigation of CNTs and CNT-polymer composites at the nanoscale while continuum models are employed to efficiently assess size effects at the macroscale. Despite the initial hypothesis of modeling the nanotubes in the CNT-polymer composites as one-dimensional nonlocal fibers (see Section 1.3), only the interphase has been considered. Due to weak non-bonded interaction between CNT and polymer chains, the reinforcement in the CNT-polymer composites is solely determined by the interphase.

The main conclusions of this study can be summarized as follows:

- An efficient numerical solution for nonlocal elastic problems, useful for the investigation of nanostructures such as carbon nanotubes, can be obtained using higher-order B-spline approximation schemes (Chapter 2).
- The effectiveness of nonlocal formulations in modeling CNTs depends on the employed nonlocal kernel and nonlocal parameters. The choice of the former and the estimation of the latter have been determined comparing the axial strain profile derived with a continuum one-dimensional nonlocal model and a discrete atomistic one. In particular, size effects in the estimated nonlocal parameters have been observed varying the diameter and chirality of the nanotubes (Chapter 2).
- One-dimensional nonlocal formulations are not suitable for modeling chiral nanotubes due to their anisotropic response (Chapter 3).
- Increasing the CNTs diameter improves the ordering and the stiffness of the interphase (Chapters 4 and 5).
- The interphase layer has a crucial role in the stiffening effects observed in CNT-polymer composites while the effect of the interface is negligible due to the weak interaction between nanotubes and surrounding polymer chains (Chapters 5).

- Although the stiffness of the interphase increases with the diameter of the embedded CNTs, the composite stiffness increases by decreasing the CNT diameter as a result of the higher interphase volume fraction (Chapters 5).
- State of the art analytical micromechanical models are poorly suited for the prediction of the elastic properties of composites reinforced with randomly distributed CNTs (see Chapters 5).

The computational procedure in this thesis is to be considered as a basic framework for the characterization of CNT-polymer composites. Although it provides a methodology for the assessment of size effects in the mechanical response of CNT-polymer composites at the nano- and macroscale, further developments are still needed for a better understanding of these materials.

Possible topics for future research are:

- The use of GFEM with *ad-hoc* enrichment functions for the nonlocal one-dimensional problems in Chapters 2 and 3. The choice of an enrichment function that captures the essence of the deformation profile along the nanotube can drastically decrease the computational effort. However, this implies that the solution of the problem, dependent on the imposed set of boundary conditions, must be known in advance.
- Accounting for the specific chemistry of a real polymer matrix for the atomistic simulations of realistic CNT-polymer composites. Although this choice increases the computational effort (i.e., higher number of atoms and complexity of the interatomic potential field), it could facilitate the comparison between numerical results and new experimental findings.
- Modeling chemical bonds between nanotubes and polymer matrix to improve the adhesion at the interface. If such a functionalization leads to comparable deformations in the CNTs and in the surrounding polymer matrix, nonlocal formulations might be required to model the nanotubes at the microscale. In this case, a new set of nonlocal parameters is needed since the boundary conditions on the nanotubes are different from those considered in Chapter 3.
- Large deformation analysis of CNT-polymer composites. Since molecular mechanics is limited to small deformations (Chapter 5), molecular dynamics simulations must be performed.
- Investigation of the dynamic response of CNT-polymer composites. This represents a challenging task since molecular dynamics simulations are limited to few nanoseconds (i.e. extremely high strain rates). Therefore, comparison with experimental results would be impossible. Nevertheless, coarse-grained models, accelerated molecular dynamics methods (e.g., hyperdynamics) or high-performance computational tools (e.g., parallelization on graphics processing units) might provide a possible solution to this problem.

Acknowledgements

The research presented in this thesis was carried out at the Department of Engineering at University of Ferrara and at the Faculty of Civil Engineering and Geosciences at Delft University of Technology. Funding for this work was provided by the Italian Ministry of Education, Universities and Research (Fondo Giovani 2011) and the European Research Council under the European Union's Seventh Framework Programme (FP7/2007-2013)/ERC Grant agreement n° 617972.

There are many people to whom I owe gratitude for the results presented in these pages and for much more that this booklet does not show.

I wish to express my appreciation to my promotors A. M. Tralli and L. J. Sluys for giving me the possibility to pursue a PhD position jointly at the University of Ferrara and the Delft University of Technology. Special thanks go to my copromotors E. Benvenuti and A. Simone for their valuable time, guidance and endless patience. I am indebted to them for the trust and support provided during all these years. I owe gratitude to Dr. A. Lyulin from the Eindhoven University of Technology for his supervision on the atomistic simulations in Chapters 4 and 5. I also would like to thank Professor A. C. Duarte from the University of Illinois at Urbana-Champaign for the invaluable help with the work in Chapter 2.

I would like to express my gratitude to all past and present colleagues and collaborators at the *LabStruture* in Ferrara and at the department of Structural Mechanics in Delft. In particular, I would like to thank P. Srinivasan, O. Verners, B. Arash and M. Goudarzi for the fruitful discussions on some of the topics in this work. A special thank you goes also to my office mates M. Simoni, N. Ponara, M. Pizzolato, A. Chiozzi and M. Musivand Arzanfudi for the pleasant time in the office.

I would like to thank my friends in the Netherlands for making me feel like home and the ones in Italy for reminding me where I'm coming from. I am grateful to each and one of them for being by my side during my PhD studies and transforming these five years into a memorable journey.

Last, but most important of all, I would like to thank those few people who *had* to share their life with mine. I gratefully thank my girlfriend Olia for the love, trust and patience I received throughout these years—that meant a lot in the moments of frustration. For their total support I owe my deepest gratitude to my wonderful family: my father Mauro, a great source of encouragement and inspiration throughout my entire life, my *nonna* Edda—the rock of our family—, my sister Fulvia for always being there and my stepmother Agata for treating me like a son. Finally, I also would like to thank my beloved mother Donatella. Although she passed away before the beginning of my PhD studies, she has always been and still is my greatest source of strength.

Marcello Malagù,
December 2016

Curriculum Vitæ

July 29 th , 1986	Born in Ferrara, Italy, as Marcello Malagù
Sep 2000 – Jun 2005	Maturità scientifica Liceo Scientifico A. Roiti
Sep 2005 – Dec 2008	Bachelor's Degree in Civil and Environmental Engineering Università degli Studi di Ferrara
Jan 2009 – Oct 2011	Master's Degree in Civil Engineering Università degli Studi di Ferrara
Oct 2011 – Dec 2011	Assistant Researcher Università degli Studi di Cagliari
Jan 2012 – May 2016	PhD Candidate Università degli Studi di Ferrara and Technische Universiteit Delft
June 2016 – present	Software developer DIANA FEA BV

List of Publications

Journal articles

1. **M. Malagù**, E. Benvenuti, C.A. Duarte and A. Simone, One-dimensional nonlocal and gradient elasticity: Assessment of high order approximation schemes, *Computer Methods in Applied Mechanics and Engineering*, 275:138–158, 2014.
2. **M. Malagù**, E. Benvenuti and A. Simone, One-dimensional nonlocal elasticity for tensile single-walled carbon nanotubes: A molecular structural mechanics characterization, *European Journal of Mechanics-A/Solids*, 54:160–170, 2015.
3. **M. Malagù**, A. Lyulin, E. Benvenuti and A. Simone, A molecular-dynamics study of size and chirality effects on glass-transition temperature and ordering in carbon nanotube-polymer composites, *Macromolecular Theory and Simulations*, 25:571–581, 2016.
4. **M. Malagù**, M. Goudarzi, A. Lyulin, E. Benvenuti and A. Simone, Diameter dependent elastic properties of carbon nanotube-polymer composites: Emergence of size effects from atomistic-scale simulations, *submitted*.

Conference proceedings

1. **M. Malagù**, A. Lyulin, E. Benvenuti and A. Simone, An atomistic-to-continuum approach to modeling size effects in polymer-carbon nanotube composites *Engineering Mechanics Institute Conference 2016*, Nashville, U.S.A., May 22–10, 2015
2. **M. Malagù**, E. Benvenuti and A. Simone, Nonlocal parameter estimation for tensile single-walled carbon nanotubes by molecular structural mechanics, *ESMC 2015: 9th European Solid Mechanics Conference*, Madrid, Spain, July 6–10, 2015
3. **M. Malagù**, E. Benvenuti and A. Simone, Benchmarking high order finite element approximations for one-dimensional boundary layer problems, *AIMETA 2013: XXI Conference Associazione Italiana di Meccanica Teorica e Applicata*, Torino, Italy, September 17–20, 2013.
4. **M. Malagù**, E. Benvenuti and A. Simone, Finite element and B-spline methods for one-dimensional non-local elasticity, *ECCOMAS 2012: 6th European Congress on Computational Methods in Applied Sciences and Engineering*, Vienna, Austria, September 10–14, 2012.
5. **M. Malagù**, E. Benvenuti, A. Simone and A.M. Tralli, A strain gradient approach to the analysis of nanoarches: Formulation and numerical solution with NURBS interpolation, *GIMC 2012: XIX Convegno Italiano di Meccanica Computazionale*, Rossano, Italy, June 25–27, 2012.

Journal articles from other projects

1. A. Cazzani, **M. Malagù** and E. Turco, Isogeometric analysis of plane-curved beams, *Mathematics and Mechanics of Solids*, 21(5):562-577, 2016.
2. A. Cazzani, **M. Malagù** and E. Turco, Isogeometric analysis: a powerful numerical tool for the elastic analysis of historical masonry arches, *Continuum Mechanics and Thermodynamics*, 28(1):139-156, 2016.
3. A. Cazzani, **M. Malagù**, E. Turco and F. Stochino, Constitutive models for strongly curved beams in the frame of isogeometric analysis, *Mathematics and Mechanics of Solids*, 21(2):182-209, 2016.
4. A. Chiozzi, **M. Malagù**, A. Tralli and A. Cazzani, ArchNURBS: NURBS-Based Tool for the Structural Safety Assessment of Masonry Arches in MATLAB, *Journal of Computing in Civil Engineering*, 30(2):04015010, 2015.